Observations and modeling of nearshore - offshore exchange processes in Lake Superior

A Dissertation
SUBMITTED TO THE FACULTY OF
UNIVERSITY OF MINNESOTA
BY

Paul McKinney

IN PARTIAL FULFILLMENT OF THE REQUIREMENTS
FOR THE DEGREE OF
DOCTOR OF PHILOSOPHY

Katsumi Matsumoto, Advisor

December 2015

Acknowledgements

This dissertation and the coursework that preceded it would not have been possible without the support of many people. In particular, I thank my advisor Katsumi Matsumoto and committee members Calvin Alexander, Jim Cotner and David Fox for their encouragement. Kathy Tokos was a cheerful office mate and on many occasions provided needed lines of code and critical discussion I will greatly miss.

Support for this research was provided by student fellowships of the University of Minnesota Department of Earth Sciences to Paul McKinney and by NSF and NASA grants awarded to Dr. Katsumi Matsumoto. All SAR images were provided by the European Space Agency through an approved Envisat principal investigator study. This work was carried out in part using computing resources at the University of Minnesota Supercomputing Institute.

Dedication

to Amy, Thomas and Hazel.

Abstract

Lake Superior's nearshore areas, including embayments, are warmer and more productive than the colder central lake basins. They are important habitat for a variety of species, and are also where human activities are concentrated. The distinction between nearshore and offshore areas is maintained by the lake's mean circulation, which is primarily shore-parallel in the nearshore. Exchange between nearshore and offshore areas occurs where and when this general pattern is disrupted, and affects important nearshore water quality parameters including concentrations of nutrients, pollutants and heat. This dissertation reports the results of three studies focused on Lake Superior nearshore exchange processes conducted with satellite data and numerical modeling.

In the first study, satellite Synthetic Aperture Radar (SAR) images of Lake Superior were examined, and eddies were identified and characterized. Eddies potentially contribute to exchange between nearshore and offshore areas of the lake because they typically form in turbulent flows, and long-lived eddies directly transport water from place to place. Forty one eddies were identified and basic statistics including their location, size, sense of rotation and distance to shore were compiled. The SAR images are of limited spatial extent, and each image only included a portion of the entire lake surface. The images reviewed covered the ice free months of 1992-1998. Comparison with satellite images of lake surface temperature showed the eddies were located within the region of high thermal gradient that characterizes the summer coastal circulation.

The second study was a sensitivity analysis conducted with a numerical model of lake hydrodynamics. Idealized model domains of varying bottom slopes characteristic of

Lake Superior were used to simulate the expansion of stratification from nearshore areas where it first occurs to the entire lake basin. The expansion was quantified by the advance of the 4 °C temperature front, known as the thermal bar, from the perimeter of the idealized basins to the center. The thermal bar is known to inhibit exchange between nearshore and offshore areas. Forcing for the simulations was varied systematically to predict the time scales over which thermal bars are expected in Lake Superior.

The third study used a realistically configured model and virtual tracers to characterize exchange between areas where water depth is less than 100 m and deeper parts of the lake. Two series of model simulations were conducted. The first covered the ten year period 2003-2012 and utilized an age tracer that showed the rate of exchange varied annually corresponding to the lake's cycle of vertical mixing and stratification. A second series of simulations covered the summer of 2004 and used passive tracers that showed offshore dispersal of nearshore water increased in late summer with the offshore expansion of stratification. The model resolved eddies at locations that included those reported in the first study and provided additional details about their contribution to exchange between the nearshore and offshore areas of the lake.

Appendix 1 is a report of observations of the thermal bar from the south shore of Lake Superior in the spring of 2012.

Appendix 2 is a summary of procedures for creating a nested grid configuration in the Regional Ocean Modeling System (ROMS).

Supplemental movie 1 illustrates the seasonal cycle of nearshore to offshore exchange using the *Age* tracer of the third study described above.

Supplemental movie 2 shows eddy locations and surface temperature anomalies in the simulations of the third study described above.

Table of Contents

List of Tables

Chapter 2:

Chapter 3:

Chapter 4:

List of Figures

Chapter 1:

Chapter 2:

Chapter 3:

Chapter 4:

List of Acronyms

ATSR: Along-Track Scanning Radiometer

AVHRR: Advanced Very High Resolution Radiometer

CDAT: CoastWatch Data Analysis Tool

CMAN: Coastal-Marine Automated Network

ERS: European Remote Sensing

ESA: European Space Agency

GLERL: Great Lakes Environmental Research Laboratory

KP: Keweenaw Peninsula

MODIS: Moderate Resolution Imaging Spectroradiometer

NARR: North American Regional Reanalysis

NASA: National Aeronautics and Space Administration

NDBC: National Data Buoy Center

NOAA: National Oceanographic and Atmospheric Administration

ROMS: Regional Ocean Modeling System

SAR: Synthetic Aperture Radar

SST: Sea Surface Temperature

Forward

This is a doctoral dissertation submitted as partial fulfillment of the degree of Doctor of Philosophy in Geology at the University of Minnesota, Twin Cities Campus. Chapters 2, 3, and 4 are papers prepared for publication with coauthors, so the collective "we" is used instead of "I". Coauthors of Chapter 2 are Ben Holt and Katsumi Matsumoto. Coauthor of Chapters 3 and 4 is Katsumi Matsumoto.

Chapter 1: Introduction to the thesis

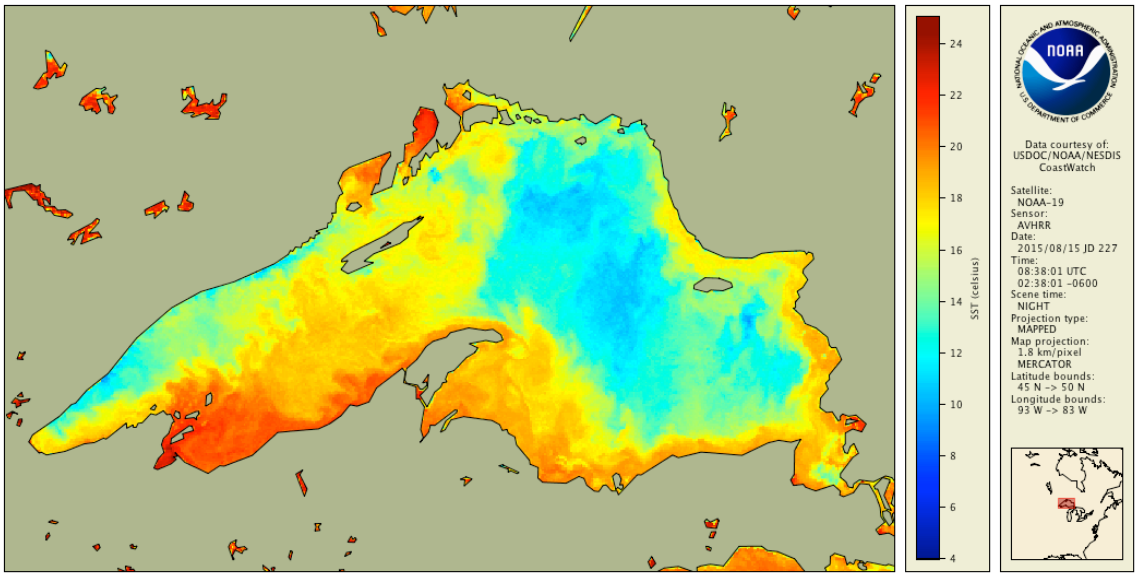

Figure 1. Satellite detected Lake Superior surface temperature on August 15, 2015.

Satellite images of Lake Superior's surface temperature in midsummer typically show central lake temperatures up to 10 °C cooler than temperatures along the coasts and within the embayments, where temperatures reach 20 °C (Figure 1). The boundary between the cooler areas offshore and warmer areas nearshore is marked by meanders and eddies characteristic of a dynamic mixing environment.

In this dissertation, remote sensing and numerical modeling are used to increase understanding of the temporal and spatial variability of the exchange between nearshore and offshore areas suggested by the meanders and eddies visible in the satellite images.

Understanding this variability is important because the nearshore is a vital freshwater resource, where human activities are focused and where a variety of species reside, and exchange processes control important nearshore water quality parameters including concentrations of nutrients, pollutants and heat.

In broad terms, nearshore areas include the dynamic zone between the surrounding watershed and the open waters of the lake, where nutrients and other inputs from the catchment first enter the lake's nutrient and energy cycles, and where existing sediments are resuspended by wave action. Periods when exchange between nearshore and offshore areas is high can improve nearshore water quality by diluting concentrations of pollutants. On the other hand, exchange can threaten nearshore ecosystems by rapidly cooling nearshore water temperatures, or by removing pelagic organisms from their preferred nearshore habitat.

Practical definitions of what constitutes the nearshore zone in the Great Lakes vary. A widely used (e.g. Yurista et al., 2011) definition is the maximum depth at which the seasonal thermocline intersects the lake bottom (Edsall and Charlton, 1997). This definition can lead to dramatic differences in the area described as nearshore between lakes. For example, at 20-30 m, Lake Erie's thermocline depth is roughly the average depth of the entire lake, and nearly the entire western basin is classified as nearshore. In deeper Lake Superior, the thermocline depth is typically 10-20 m, and only a small area is classified as nearshore due to its steeply plunging shoreline.

In Lake Superior, a broader definition of nearshore includes coastal areas where water depth is less than 100 m. Nearshore defined in this way includes the shore-parallel

coastal circulation which dominates the lake's mean circulation (Bennington et al., 2010) as well as the region of high thermal gradients and fronts where numerous eddies and meanders are typically observed in summer (Figure 1; Ullman et al., 1998; Mortimer, 1988; Budd, 2004). It also captures the coastal component of the lake's food web, composed of warm and cool water species and supported by benthic algae and invertebrates. The lake's offshore food web is composed of cold water species, and is supported by plankton (Gorman et al., 2011; Auer et al., 2013; Sierszen et al., 2014). The degree to which physical processes in Lake Superior connect these two communities is largely unexplored.

Chapter two is the first of three chapters reporting results of research on nearshore to offshore exchange processes in the lake. Originally published in the Journal of Great Lakes Research (McKinney et al., 2012), and reproduced here by permission of Elsevier, B.V., it is a remote sensing study in which eddies were identified and characterized in nearshore areas of the lake using Synthetic Aperture Radar (SAR) images obtained from the European Space Agency. Eddies participate in many processes in the ocean, including mass and tracer exchange. They continue to be the focus of extensive research (McWilliams, 2008). However, there have been few studies of their occurrence and properties in the Great Lakes and Lake Superior (Mortimer, 1988; Ralph, 2002; Budd, 2004). The basic characteristics reported in chapter two contribute to the scant observational record and provide a foundation for the subsequent chapters.

In chapter three, a numerical model with idealized model domains was used to simulate the springtime 4 °C thermal front, known as the thermal bar, under a range of

idealized forcing scenarios. The thermal bar inhibits nearshore to offshore exchange during Spring and Fall in large dimictic lakes as they transition to stratified conditions (Rao and Murthy, 2007). In Lake Superior, previous studies of the thermal bar are limited to the Keweenaw Peninsula region (e.g. Chen et al., 2001; Auer and Gatzke, 2004). The idealized modeling provides a framework for understanding how the thermal bar evolves in lakes like Superior that have a wide range of nearshore bathymetry.

Chapter four builds on the two previous chapters by using a realistically configured numerical model of Lake Superior to simulate its temperature and circulation over a 10 year period. Idealized passive tracers were used to quantify spatial and temporal variability of exchange between nearshore areas, defined as those where water depth is less than 100 m, and deeper areas of the lake. The grid size of the realistic model domain was appropriate for resolving the larger scale eddies described in the SAR study, and an eddy detection algorithm was used to locate and characterize eddies in the model output. This allowed an estimate of their contribution to exchange between nearshore and offshore areas in the lake.

Chapter 2 : Small eddies observed in Lake Superior using SAR and sea surface temperature imagery.

This chapter was published in full as McKinney, P., Holt, B., Matsumoto, K., 2012. Small eddies observed in Lake Superior using SAR and sea surface temperature imagery. Journal of Great Lakes Research 38, 786-797. Reproduced with the permission of Elsevier, B.V.

Abstract

Making use of the fine resolution of satellite SAR imagery, we observe small eddies during the spring and summer months in several locations in Lake Superior. During these months there is a thermal gradient between warmer nearshore waters and colder offshore waters which enhances cyclonic coastal currents. Using spaceborne SAR imagery from the European Space Agency's ERS-1 and ERS-2 missions from 1992 to 1998, we observe small eddies, identifying and mapping basic eddy characteristics including diameter, location, and rotational sense. In total, 45 eddies were located, of which 41 were cyclonic and 4 anticyclonic. Average diameter was 9.8 km and average distance to shore was 8.1 km. Based on sea surface temperature data from AVHRR, the eddies are located within the region of sharp thermal gradients of order 3-5 °C per 3 km. Spatial and temporal coverage was uneven, however, more eddies were seen in SAR images taken in late summer along the southern and eastern shores as well as areas where the boundary current interacts with topographic features including islands and promontories.

Introduction

An improved understanding of surface transport processes is necessary to predict the fate of sediment, pollutants and invasive species in Lake Superior. Numerical models are a potentially useful predictive tool in this regard, but they would benefit from having additional observational constraints. Satellite borne synthetic aperture radar (SAR) reveals fine details of surface circulation across large spatial scales, and can fill this need.

Long term observations of circulation within Lake Superior are limited to the summer season and include a drift bottle experiment from the 1890s (Harrington, 1895) and current meter data from the 1960s (Sloss and Saylor, 1976). Beletsky et al. (1999) compiled these and other results from smaller scale investigations, including the few winter season observations, in maps of winter and summer circulation. The maps provide the observational basis for numerical models of the lake's mean circulation (e.g. Bennington et al., 2010).

Mean circulation patterns within the lake vary seasonally according to changes in its thermal structure. As is common for deep lakes at mid latitudes, Lake Superior undergoes an annual cycle of density stratification in which it mixes twice yearly, in the spring and the fall (Bennett, 1978). During the stratified seasons, midlake circulation is distinct from nearshore, where thermally driven geostrophic boundary currents contribute to counterclockwise flow (Bennington et al., 2010). Lake Superior exhibits a persistent nearshore/offshore horizontal temperature gradient throughout the summer stratified season, beginning in spring during the thermal bar period (Ullman et al., 1998). Bottom slope directly contributes to the gradient strength, which is strongest where bottom slope

is steepest (Bennington et al., 2010). Variability of nearshore temperature structure and circulation in stratified basins is due to wind driven motions of the thermocline including internal waves and upwelling and downwelling (Troy et al., 2012; Austin and Lentz, 2002).

In Lake Superior, these combined influences contribute to the formation and variability of the Keweenaw Current (Chen et al., 2001; Zhu et al., 2001). The current travels to the northeast along the western coast of the Keweenaw Peninsula, and influences lakewide processes including sediment deposition patterns (Van Luven et al., 1999). Southwesterly wind associated with onshore Ekman transport and downwelling intensifies the current, and northeasterly wind associated with offshore Ekman transport and upwelling weakens it. Peak speeds above 75 cm s^{-1} occur during downwelling favorable wind conditions (Chen et al., 2001; Zhu et al., 2001).

The numerical model of (Chen et al., 2001) predicts the formation of a 26 km diameter warm core anticyclonic eddy downstream of where the Keweenaw Current detaches from the peninsula. The authors observed an eddy similar in scale and position in a satellite image of lake surface temperature, and suggested it is a recurring feature of the coastal circulation in that area. Budd (2004) observed and tracked a similar eddy, 50 km in diameter, in the same area east of the Keweenaw Peninsula using ocean color and lake surface temperature satellite data. In a lakewide study that combined satellite images of lake surface temperature and shipboard temperature and current measurements, Ralph (2002), reported a complex midlake circulation pattern filled with small scale eddies. She hypothesized the eddies formed by baroclinic and barotropic coastal processes and were

subsequently confined to the central lake basin. However, beyond the Keweenaw Peninsula, such eddy producing areas have yet to be reported.

To identify and characterize small scale circulation features in Lake Superior, we examined spaceborne SAR imagery of the lake to find small eddies and other types of detailed surface structure, like filaments and fronts, which are indicative of current variability. Remote sensing provides an excellent method for observing lake surface properties including circulation patterns over large scales (e.g. Steissberg et al., 2005). Previous remote sensing studies in Lake Superior, including those described above, have primarily been based on lake surface temperature. Horizontal resolution of the thermal images used in the previous studies was 1.1 km, and mostly limited to the waters surrounding the Keweenaw Peninsula. Detection of circulation features using thermal data requires cloud free conditions plus at least some thermal gradient for contrast between features.

In contrast, spaceborne SAR data provides a fine resolution (25-100 m), two-dimensional radar backscatter map of the roughness of the ocean surface. SAR imagery is largely unaffected by clouds and does not require sunlight because it provides its own radiating power, as opposed to passive sensors which detect emitted radiation (Holt, 2004). Because of its power requirements and capability for fine resolution, SAR sensors operate with a limited duty cycle so coverage is not continuous, as other water-detecting sensors such as scatterometers or medium resolution optical sensors such as MODIS or AVHRR.

SAR imagery of the sea surface has been used to detect a wide variety of phenomena including surface and internal waves, current boundaries and temperature fronts based on its sensitivity to changes in bathymetric, wind, and atmospheric patterns (Holt, 2004). SAR has also been widely used to detect both large and small eddies (Fu and Holt, 1982; Liu et al., 1994; Johannessen et al., 1996; DiGiacomo and Holt, 2001; Marmorino et al., 2010).

Large eddies (greater than 50 km in diameter) are generally observed in SAR data by wave-current interactions along the current shear at the outer eddy boundary, which appear as narrow bands of enhanced backscatter compared to the surrounding ocean (Fu and Holt, 1982; Holt, 2004). Smaller, submesocale eddies (less than 50 km) are seen most commonly by a series of dark, narrow, curvilinear bands that serve as tracers of the internal dynamics of the eddy flow field. The dark bands are composed of surfactants, including biogenic films, concentrated by convergent surface flows and retained at the surface into bands. The surfactants dampen capillary waves, reducing radar backscatter, and thus appear dark on SAR imagery and as highly reflective surfaces in sun-glint imagery such as most notably obtained via NASA's Space Shuttle program (Munk et al., 2000). The difference between imaging mechanisms for large and small eddies with SAR is likely associated with simple energetics, with large eddies being more energetic than small ones and thus enable stronger wave-current interactions that enhance the radar return, rather than suppress it as in the case of curvilinear surfactants.

In numerous SAR-based studies (Fu and Holt, 1982; Liu et al., 1994; Johannessen et al., 1996; DiGiacomo and Holt, 2001; Marmorino et al., 2010), smaller detected eddies

generally appear as several radar-dark filaments wound into a spiral. Rotational sense is predominantly cyclonic, diameters are less than 20 km in diameter, and spacing between the dark bands is 100 m – 1 km (Munk et al., 2000). Also, in many cases, similar surfactant bands are present but not aligned into eddy-like features. Such bands have recently been modeled as forming from the intensification of cold filaments (McWilliams et al., 2009). These studies showed that small eddies are generally associated with islands and coastal headlands, but little is presently known about their physical properties at depth, due primarily to the difficulty of in-situ sampling, due to the eddies' transient nature and small size (Marmorino et al., 2010). Efforts have been directed toward models of small eddy formation but these models have not yet been confirmed, primarily due, again, to difficulty in obtaining suitable time series from both in situ and remote sensing (e.g. Munk et al., 2000), while it can be assumed that in fact multiple generation mechanisms may exist.

In addition to the presence of surfactant lines in SAR images of eddies, there may be a contribution to radar backscatter due to horizontal temperature gradients and differences in atmospheric stability over water of different temperatures. The atmospheric boundary layer is more stable and surface windspeeds lower over colder water than adjacent warm water, so there may exist lower backscatter in the colder waters than in surrounding, warmer zones. When available, sea surface temperature maps generally confirm the presence, size, and sense of the small eddies (Johannessen et al., 1996; DiGiacomo and Holt, 2001; Marmorino et al., 2010). Lastly, Marmorino et al., (2010) used feature tracking to determine rotational sense from imagery obtained over short time

intervals. We believe this is the first study to examine SAR data for circulation patterns and eddies in Lake Superior, but SAR has been used to examine various atmospheric patterns including cold air outbreaks in the Great Lakes (Winstead et al., 2002).

We report the presence of small-scale eddies in Lake Superior from both SAR and AVHRR temperature data. These observational efforts complement our earlier numerical modeling work at the University of Minnesota in which a new realistically configured, dynamical model of the lake, coupled to ice and biogeochemistry, was developed (White et al., 2012). The data and analysis methods are described in Section 2. Eddy characteristics from SAR including locations, size distribution, seasonal patterns, and prevailing wind speed at the time of SAR image acquisition are presented in Section 3. In Section 4, representative SAR images are presented along with AVHRR data of key locations within the lake where eddies were observed. We conclude with a summary in Section 5.

Data and Methods

Data sets

We report the size, rotational sense, and distribution of small eddies observed in SAR images of Lake Superior during the ice-free months. We primarily examined SAR imagery from the two European Space Agency's (ESA) European Remote Sensing (ERS) satellite missions, ERS-1 and ERS-2. ERS-1 flew between 1991 and 2000. ERS-2 was launched in 1995 and was retired in 2011. The period 1992-1998 includes nearly all the ERS-1 and ERS-2 SAR images that include Lake Superior. We limited the study to the

months April through October, which include isothermal as well as summer stratification periods, and avoids months when the presence of ice complicates interpretation.

SAR images were obtained from the European Space Agency's archive. The SARs on both ERS-1 and ERS-2 have identical configurations. Each SAR is a C-band (5.3 GHz) sensor that operates in a single-channel mode with vertical transmit-vertical receive polarization (VV). The SARs have a fixed range of viewing angles between 20-26° and a swath width of 100 km, with an individual processed image frame being 100 km by 100 km in area and having a resolution of 30 m. The comparatively narrow swath compared to the lake size meant that only portions of the lake were imaged during each pass. With a 35-day repeat orbit, the best near-repeat coverage possible along a specific track was every 9-days, but coverage was sporadic. Reasonable time series of SAR images were thus difficult to obtain, but over time most of the lake was eventually imaged during a single season. Lastly, the satellites each were in sun–synchronous 98.5° orbit inclination with equator crossing times of ~11am and 11pm local time (04:00 UTC and 1600 UTC, respectively), which are known to be favorable for ocean feature detection with SAR for any nominal diurnal wind speed patterns that may exist.

The surface temperature of the lake was determined from AVHRR imagery with 1.1 km pixel resolution (local area coverage) obtained from NOAA's Comprehensive Large Array-data Stewardship System (CLASS) website[1]. Files were analyzed using the Coastwatch Data Analysis Tool (CDAT), part of the Coastwatch Utilities software

[1] http://www.class.ngdc.noaa.gov/saa/products/welcome

package, v.3.2.3, available online[2]. The AVHRR imagery requires cloud free conditions for lake surface detection, which reduced our ability to confirm the lake surface temperature for most the SAR imagery with detected features. The lake surface temperature was also measured at three buoys within the lake. Compared to the buoys, the AVHRR lake surface temperatures have a bias of .5 °C and a standard deviation of 1°C (Li et al., 2001). We obtained over-lake wind speed and direction from data recorded at the three midlake buoys (triangles, Figure 1) deployed during the shipping season and archived at the National Data Buoy Center (NDBC) website[3]. Data from the buoy closest to the part of the lake imaged by the SAR were used to characterize the wind field.

SAR-derived measurements of eddies

Simple geometric methods have been developed to identify the eddy center on SAR imagery and also the outer boundary of the eddy based on the spiraling-nature of the radar-dark narrow surfactant bands (e.g. Johannessen et al., 1996; DiGiacomo and Holt, 2001; Marmorino et al., 2010). In this study, we followed a process for eddy detection based on the method described in DiGiacomo and Holt (2001). Images were visually inspected for slicks and eddies that are visible in SAR images as surfactant bands that either appear as spirals with a clearly detectable outer ring or as nearly contained quasi-circular patterns, as described in section 1 above and in numerous other references (e.g. Johannessen et al*.,* 1996). The narrow bands are darker than the surrounding ocean radar returns due to suppression of the capillary waves by the surfactant material. No eddies

[2] http://coastwatch.noaa.gov/cwn/cw_software.html
[3] http://www.ndbc.noaa.gov/

were detected that had enhanced returns at the current shear boundary; a more prevalent feature of larger, mesoscale ocean eddies. Eddies were characterized by estimated diameter (from approximate center to outer boundary of concentric dark bands), distance to shore and rotation. Eddy diameter was calculated as the average of the major and minor axis lengths drawn through the center of the eddy. The diameter and distance to the closest point of land was measured from the eddy center (Figure 2). Any single eddy had to appear nearly enclosed by bands, otherwise it was not included.

Results

Of the 361 images examined, 57 of the images contained filament slicks. Although more images were taken at mid-day local time than in the evening, the percentage of frames containing slicks was the same (Table 1). After 1995 and the retirement of ERS-1, all images were acquired at mid-day. The monthly distribution of SAR frames slightly favored the months of July and August; slicks and eddies were more likely to be seen in those months than any other (Table 2). We only roughly categorized SAR images as covering the western, central, or eastern part of the lake, and spatial coverage of the lake was uneven, favoring the western and eastern areas. Despite this bias, slicks were seen in roughly the same percentage of images from each region, although the percentage of images containing eddies was higher for the central and eastern parts of the lake (Table 3). Windspeeds recorded at the NDBC buoy closest to the part of the lake imaged by the SAR were low to moderate, as expected for SAR visualization of surface circulation (Figure 3).

The total number of eddies detected was 45, and over half were observed in SAR images taken in August (Figure 4a). Forty-one of the eddies were cyclonic (counter clockwise rotation) and 4 were anticyclonic. Due to cloud cover, corresponding AVHRR images were not available for all the SAR images. Where available, they showed cyclonic eddies were cold core and anticyclonic eddies were warm core. Eddy diameters were measured in the SAR images and were between 2.6 and 21.0 km. The average diameter was 9.7 km (Figure 4b, c). This size range is smaller than eddies reported previously from AVHRR images of the Keweenaw Peninsula region of the lake (Budd, 2004; Chen et al., 2001). The fine resolution of the SAR images also allowed us to measure more precisely the position of the eddies and related filaments relative to shore. Distance from the eddy center to shore varied between 1.8 and 21.0 km and averaged 8.1 km (Figure 4d). Model results show this range of distances corresponds to the high velocity boundary current typical of summer (Figure 5).

The filaments and eddies were observed under low to moderate wind conditions (Table 4). Visual detection of eddies via surfactant lines in C-band SAR images is dependent on low to moderate windspeeds, typically between 3-7 m s^{-1} (DiGiacomo and Holt, 2001). Wind speeds below 3 m s^{-1} do not generate enough ocean backscatter, thus the surrounding ocean appears as dark as the slicks themselves and thus the slicks are not distinguishable. Higher wind speeds disperse the surfactants, also rendering the slicks and eddies not detectable (Wurl et al., 2011).

Eddy Examples

Figure 6 is a characteristic summertime thermal pattern for the lake observed on August 22, 1994, 22:03 UTC. The corresponding local time is 18:03 in the eastern part of the lake bordering Michigan and Canada, and 17:03 in the southwestern arm bordering Wisconsin and Minnesota. The essentially cloud free image is unusual; most thermal images of the lake contain extensive clouds over significant portions of the lake. In this figure, scattered clouds appear as small-scale cold features over parts of the southwestern lake and at the northwest tip of the Keweenaw Peninsula. The labeled boxes indicate locations of the images discussed below. The summertime pattern includes warm water concentrated along the southern and eastern coasts. As discussed above, this characteristic temperature structure exerts a first order control on nearshore circulation during summer, and promotes a counterclockwise coastal circulation, with the strongest currents occurring near the tip of the Keweenaw Peninsula.

Wind records from the central and eastern midlake buoys indicate that 18 hours previous to the time the image was taken the wind direction abruptly shifted from westerly to northeasterly, and windspeeds dropped from an average of 5 m s^{-1} to under 3 m s^{-1}. There is a gap in the data from the western buoy for this period and data is not available. Prior to the wind shift, winds had been from the west/northwest for 36 hours. This promotes upwelling along northwestern shore, and downwelling along the southern shore including the Keweenaw Peninsula. The effects of the prolonged westerly winds are still visible as a band of cold water is evident in the image along the northwest shore.

Numerous warm water plumes are visible within the coastal waters along the southern shore.

Figure 7 includes ERS-1 SAR (Figure 7a) and thermal (Figure 7b) images from August 5, 1992 covering the tip of the Keweenaw Peninsula and the area in the southeast. The Keweenaw Current is visible in the thermal image as a band of warm coastal water of temperature up to 16 °C. As discussed previously, the current is a persistent feature of the summertime circulation. The wind data from the eastern buoy, NDBC 45004, (Figure 7c) shows that 72 hours previous to the SAR image, the winds were from the northwest, which directs the current to the southeast of the peninsula (Van Luven et al., 1999). In the SAR image, filaments are generally aligned with the southeast flow. The AVHRR image shows water temperatures in this area are between 8 and 15 °C.

An anticyclonic, warm core eddy 19 km in diameter is centered 21 km from the peninsula tip ("a" in Figure 7a, b). This corresponds to the location of the persistent summertime eddy found in previous remote sensing observations of surface water temperature (Budd, 2004) and numerical modeling studies of the Keweenaw Current (Chen et al., 2001). Temperatures are warmer at the eddy center, as expected for geostrophic anticyclonic rotation. Temperatures determined using the CDAT image analysis tool are 10 °C at the edges of the eddy and 13.7 °C at the eddy center. Along the southern shore, a cold core cyclonic eddy 17 km in diameter has formed where cooler water from offshore has intruded into a backward breaking meander of the warmer coastal flow ("b" in Figure 7a, b). As expected for cyclonic rotation, temperatures are

colder at the eddy center. Temperatures according to the CDAT tool are 15.4 °C at the eddy edge and 13.3 °C at the center.

The wind vector chart (7c) shows that 28 hours before the SAR image, windspeeds dropped abruptly for 6 hours, and wind direction shifted from the prevailing westerly winds to strong northerly winds. Niebauer et al. (1977) reported the variability of the Keweenaw Current is directly related to the changing wind conditions associated with passing weather systems. Examination of regional weather maps for this period showed the drop in wind speed occurred as a low pressure system moved out of the area. The stronger northerly winds were due to an approaching high pressure system. Eight hours before the SAR image time, wind direction shifted again, to westerly. This comparatively short period between the shift in wind direction and SAR image acquisition may have reduced the visibility of filaments in the SAR image compared to Figures 8-10 below. In those examples, the time gap between the most recent change in wind conditions and SAR image acquisition is longer, providing more time for the surface expression of the eddies to re-form as the boundary current responds to changing wind conditions, and for filaments to align with the underlying dynamics.

The thermal image of Figure 8 expands Figure 6 in the southwestern part of the lake for a closer examination. The accompanying ERS-1 SAR image (8a) was taken 6 hours later than the thermal image (8b). Multiple small eddies between 4.2 and 9.5 km in diameter are visible within Whitefish Bay, and a larger anticyclonic eddy 20 km in diameter has formed in the lee of Whitefish Point. The wind record from the eastern buoy, NDBC ID 45004, indicates that 24 hours prior to acquisition of the SAR, winds

shifted from strong northwesterly winds to weak southeasterly winds (8c). Examination of regional weather maps showed a low pressure system centered south of the lake moved east during this time and the southeasterly winds that begin roughly 16 hours prior to the SAR image time were due to an approaching high pressure system. The northwesterly winds strengthen the cyclonic coastal current along the southeast shore, and weak upwelling associated with the southeast winds weakens it. The time between the change in wind conditions and the SAR acquisition is longer than in Figure 7, 16 hours versus 8 hours, improving the visibility of the filaments and eddies, as described above.

Figure 9, from August 19, 1997, includes a northern section (A) and a southern section (B) in the eastern region of the lake (Figure 6). There was no single date for which both areas were cloud free, and AVHRR images from separate dates (right) are used for comparison with the ERS-2 SAR (left). Within the northern section, including the area near Michipicoten Island, temperatures between the coastal and offshore waters vary by 6.5 °C, from 8.5 – 15 °C. Multiple filaments and two cyclonic eddies are visible, a 15 km diameter eddy (a) and an 18 km diameter eddy (b). In the southern section (B), the nearshore to offshore temperature difference is 5.5 °C (22.3 – 16.8 °C) (right). A cyclonic eddy (c) 21 km in diameter is at the outer half of the coastal band. The wind record from the eastern buoy, NDBC 45004 indicates winds were from the northwest and west from 72 to 22 hours prior to the time of the SAR image, followed by light and variable winds in the hours just before the time of the image (C). Examination of the surface weather map for the period indicated the northwesterly winds were due to a low pressure system that passed south of the lake. The light and variable winds correspond to

a subsequent high pressure system that passed over the lake. The wind record shows the low wind period before SAR acquisition is over 24 hours long. As discussed above, this longer period likely contributes to the sharper definition of the eddies relative to Figure 7. Figure 10a, from August 10, 1994, shows the eastern extent of the Apostle Islands area. No thermal images were available from this period, due to cloud cover. Six cyclonic eddies (a-f) with diameters between 3.6 and 11.9 km have formed in the waters surrounding the islands (A). The diagram of wind vectors from the western buoy, NDBC 45006, (B) shows that 60 hours prior to the SAR image time, winds shifted from southerly to northerly and were moderately strong for the following 12 hours. Subsequently, winds were light and variable. Examination of the synoptic weather map for those dates showed the northerly winds were associated with a low pressure system that passed directly over the lake, and the subsequent low wind period corresponded to a high pressure system passing over the lake. The length of the low wind period preceding SAR image acquisition is longest for this image compared to Figures 7, 8 and 9, which likely contributes to the comparatively sharper definition of eddies in this image.

Discussion and Summary

A combination of SAR and AVHRR satellite imagery reveals small-scale spiral eddies and filament slicks within the nearshore waters of Lake Superior during the summertime heating season. Filament patterns indicate significant complexity across a wide range of scales within the lake, however we limited our survey to small, spiral-type

eddies, similar to those described in multiple coastal ocean studies (e.g. Johannessen et al., 1996; DiGiacomo and Holt, 2001).

The eddies formed in the nearshore region along thermal fronts and shear zones associated with the boundary current that dominates the summertime coastal circulation pattern. Eddy rotation was primarily cyclonic, and appeared to have seasonal and geographic distribution although some bias may have been due to wind aliasing and the irregular coverage of the lake by the collected images. Small eddies were more frequently seen in images of the lake taken during August. Slow current speeds offshore, combined with the frequency of windspeeds that disperse the surfactants necessary for SAR visualization may have reduced our ability to detect eddies away from the coastal waters where they formed.

Wind measurements recorded by the midlake buoys may not accurately describe conditions nearshore. On one hand, windspeeds nearshore are typically lower than offshore due to the land's influence. On the other hand, warmer water temperatures nearshore contribute to a less stable atmospheric boundary layer and higher windspeeds relative to offshore, where colder water leads to a more stable boundary layer. In addition, diurnal wind patterns can lead to differences between the offshore and nearshore wind fields. To assess the effect of these factors, we compared the buoy wind data to wind data acquired at land based weather stations and CMAN stations near shore for selected images and found no substantial differences between the two data sets at the time of the SAR image.

Besides suitable windspeeds, SAR imagery is dependent on the presence of surfactants in the surface layer. In our survey, we observed higher concentrations of slicks and eddies in Lake Michigan than in Lake Superior when the SAR images included parts of both lakes. Wind conditions as expressed in the SAR appeared to be similar, and the difference is likely due to a higher concentration of surfactants in Lake Michigan, which we intend to examine in a follow-up study for comparisons with Superior. As described above, biotic and abiotic surfactants in the surface layer dampen small-scale capillary waves and reveal the local underlying circulation pattern.

Lake Superior is an oligotrophic, minimally impacted environment, so surfactant concentrations are likely to be low compared to more eutrophic environments. Total dissolved phosphorus concentrations are near the detection limit, typically 20-30 nmol L^{-1} (Field and Sherrell, 2003). The low phosphorus levels limit primary production to between 200 and 350 mg C m^{-2} d^{-1} (Sterner, 2010). In comparison, characteristic values within Lake Michigan during the 1990s were between 400 and 1,200 mg C m^{-2} d^{-1} (Fahnenstiel et al., 2010). The higher production rate likely results in higher concentrations of biotic surfactants (Wurl et al., 2011). Lake Michigan also has a higher human population within its watershed, so concentrations of abiotic surfactants are also likely to be higher than in Lake Superior. Therefore, the hydrodynamic features evident in the SAR images may be more abundant in Lake Superior than we were able to detect due to low concentrations of surfactants.

An analysis of selected images suggests that the eddies formed within 24 hours of a reduction in wind speed and shift in wind direction. The low windspeeds near the time

of image acquisition aided visual identification of the features. Results from a recently completed hydrodynamic model of mean circulation indicate the response of the nearshore zone to changes in wind stress is delayed compared to offshore, where currents respond the same day (Bennington et al., 2010). If the eddies reported here form as part of the nearshore response to changing wind conditions, our results suggest this process occurs most often along the southern and eastern shore and is most likely to occur later in the summer. The timing of wind shifts relative to image time, the short lifetime of these features, and low concentrations of surfactants in the surface layer may explain the number of images that were acquired under similar wind speeds, but did not include eddies.

Eddies observed in April, May and June were on average smaller than those observed later in the season; their diameters were less than 6 km, whereas those observed in August averaged over 10 km diameter (Figure 4c). The horizontal length scale associated with geostrophic processes in a 2-layer stratified model of upper thickness and density h1 and ρ1 and lower thickness and density h2 and ρ2 is the first baroclinic Rossby radius of deformation defined as $R_1=(g'h')^{1/2}/f$, where g' is reduced gravity, $g(\rho 2 - \rho 1)/\rho 2$, the effective depth of the mixed layer h' is defined as h1h2/h1+h2, and f is the Coriolis parameter, 10^{-4} s^{-1} for mid-latitudes. R_1 varies depending on stratification strength and thickness of the mixed layer, and a typical value for the Laurentian Great Lakes is between 5 and 10 km (Csanady, 1975). The smaller size of eddies in April and May is consistent with a shallower mixed layer and smaller deformation radius earlier in the heating season.

Thirty three percent of eddies were located between 6 and 9 km from shore (Figure 4d), corresponding to the expected location of the geostrophic current's outer boundary (Zhu et al., 2001; Chen et al., 2004). Unfortunately, the collected SAR images did not include time series of images that would be useful to determine the timescales of eddy formation or persistence. The possibility of rapidly-repeating imagery would enable the derivation of rotational velocity fields from feature extraction (Marmorino et al., 2010).

The size and distribution of the eddies reported here provides additional observations to guide numerical modeling of the lake's circulation and biogeochemical cycling. An example of recent modeling results is included in Figure 5, which shows a subset of the historical run between 1985 and 2008 from the model of White et al. (2012). The time period corresponds to the 1992-1998 period of SAR imagery used here. The model is based on the ROMS architecture of Shchepetkin and McWilliams (2005), and includes a dynamic and thermodynamic ice module. The Lake Superior model reasonably simulates the spatial and temporal variability of temperature and ice cover as observed and has the capability to simulate a lower order ecosystem. The results show a high speed coastal current around the lake's perimeter. The coastal current is cyclonic and coincides to first order with where eddies have been observed with SAR. Further model refinement to capture the eddies in the model, and determine their contribution to the transport and fate of sediment, pollutants and invasive species in the lake is underway.

This report presents the results of a study of SAR imagery in which spiral eddies were observed in Lake Superior. Images were acquired by the ESA ERS-1 and ERS-2

satellites during the ice free months of 1992-1998. The sizes and locations of the eddies are reported, as well as the wind speeds under which they were observed. Although their specific impact on mixing cannot be determined without further detailed investigations, their spatial and temporal distribution suggests impacts increase during the heating season, peaking in late summer along the southern and eastern shores as well as areas where the density driven boundary current interacts with topographic features including islands and promontories. Further research is required to determine the formation mechanisms responsible for these features, eddy energetics, and the extent to which they contribute to mixing processes within Lake Superior. This could be accomplished by combining numerical modeling with more detailed observations, which could be provided by more rapidly sampled SAR time series together with SST imagery.

Acknowledgements. Support for this research was provided by student fellowships of the UM Department of Earth Sciences to PM and by NSF grant OCE-0825576 and McKnight Land Grant Professorship awarded to KM. BH was supported by the National Aeronautics and Space Administration through a contract with the Jet Propulsion Laboratory, California Institute of Technology. All SAR images were provided by the European Space Agency through an approved Envisat principal investigator study (BH).

TABLES

image time	1992	1993	1994	1995	1996	1997	1998	total	
4:00 UTC	8(2)	48(7)	16(3)	9(1)	0(0)	0(0)	0(0)	81(13)	16%
16:00 UTC	40(11)	46(5)	41(7)	30(1)	47(8)	37(9)	39(3)	280(44)	16%
total	48(13)	94(12)	57(10)	39(2)	47(8)	37(9)	39(3)	361(57)	16%

Table 1. Number of images for ERS-1 and ERS-2 SAR covering Lake Superior May-October 1992-1998. The number of SAR images used in the study is shown by acquisition time. The number in parentheses indicates the number of images that contained slicks.

Year	Apr	May	Jun	Jul	Aug	Sep	Oct	Nov	Total
1992	5(1)	2(0)	5(1)	7(4)	10(5)	7(1)	8(1)	3(0)	47(13)
1993	4(0)	16(0)	13(3)	18(1)	15(6)	14(2)	14(0)	0(0)	94(12)
1994	0(0)	13(0)	12(3)	13(4)	9(2)	6(1)	4(0)	0(0)	57(10)
1995	0(0)	1(0)	9(1)	8(0)	2(1)	12(0)	7(0)	0(0)	39(2)
1996	0(0)	11(1)	5(0)	8(1)	9(5)	7(0)	7(1)	1(0)	48(8)
1997	0(0)	7(1)	3(1)	6(3)	9(4)	6(0)	6(0)	0(0)	37(9)
1998	7(0)	4(0)	4(1)	5(1)	9(1)	6(0)	4(0)	0(0)	39(3)
Total	16(1)	54(2)	51(10)	65(14)	63(24)	58(4)	50(2)	4(0)	361(57)

Table 2. Monthly Distribution of SAR Images. The number of SAR images used in the study is listed by month. The number in parentheses indicates the number of images containing slicks.

Lake region	Central	Eastern	Western	Total
Number of frames viewed	64	124	173	361
Frames with slicks	10	23	24	57
Frames with eddies	4	8	6	18
Percentage of frames with slicks	16%	19%	14%	16%
Percentage of frames with eddies	6%	6%	3%	5%
Percentage of frames with slicks also containing eddies	40%	35%	25%	32%

Table 3. Spatial distribution of SAR images. Spatial coverage of Lake Superior by the SAR images used in the study. The Lake was approximately divided into thirds based on the locations of the three NOAA buoys, 45001 (central), 45004 (eastern), and 45006 (western). See Figure 1 for buoy locations.

Windspeed (ms^{-1})	0-1	1-2	2-3	3-4	4-5	5-6	6-7	7-8	8-9	9 +	Total
Frames with eddies	1	1	3	6	7	0	0	0	0	0	18
Frames with slicks	5	4	12	14	13	9	0	0	0	0	57
Frames without slicks	11	24	48	47	34	38	30	23	12	37	304
Total	16	28	60	61	47	47	30	23	12	37	361
Percent with slicks	31%	14%	20%	23%	28%	19%	0%	0%	0%	0%	16%

Table 4. Windspeed of SAR images. Number of SAR images used in the study that contained filament slicks and eddies relative to wind speed recorded at the nearest NDBC buoy. Buoys are deployed during the ice free season.

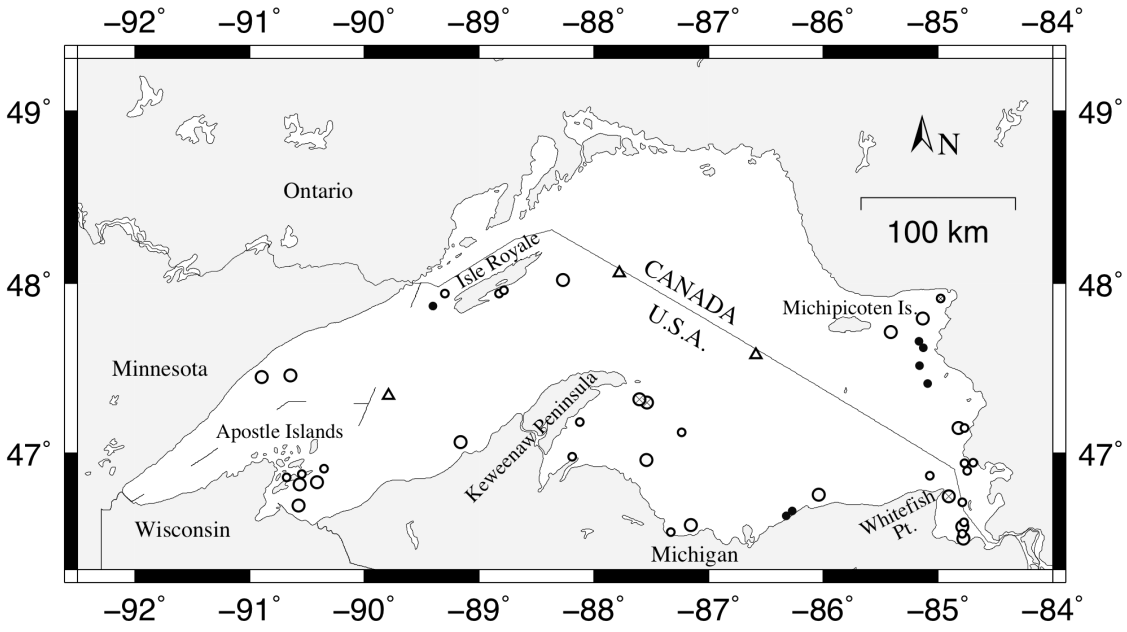

Figure 1. Map of Lake Superior showing buoy locations and eddy locations. Triangles indicate locations of the NDBC buoys used for wind analysis. The western buoy number 45006 is located at 47.335 N 89.793 W. The central buoy 45001 is located at 48.064 N 87.777 W. The eastern buoy 45004 is located at 47.584 N 86.587 W. Small circles represent eddies under 10 km in diameter, large circles represent eddies larger than 10 km in diameter. Filled circles mark the location of eddies seen in SAR images taken in April-June, all of which were cyclonic. Open circles mark location of eddies seen in SAR images from July-Sept. Those enclosing an "x" indicate anticyclonic rotation.

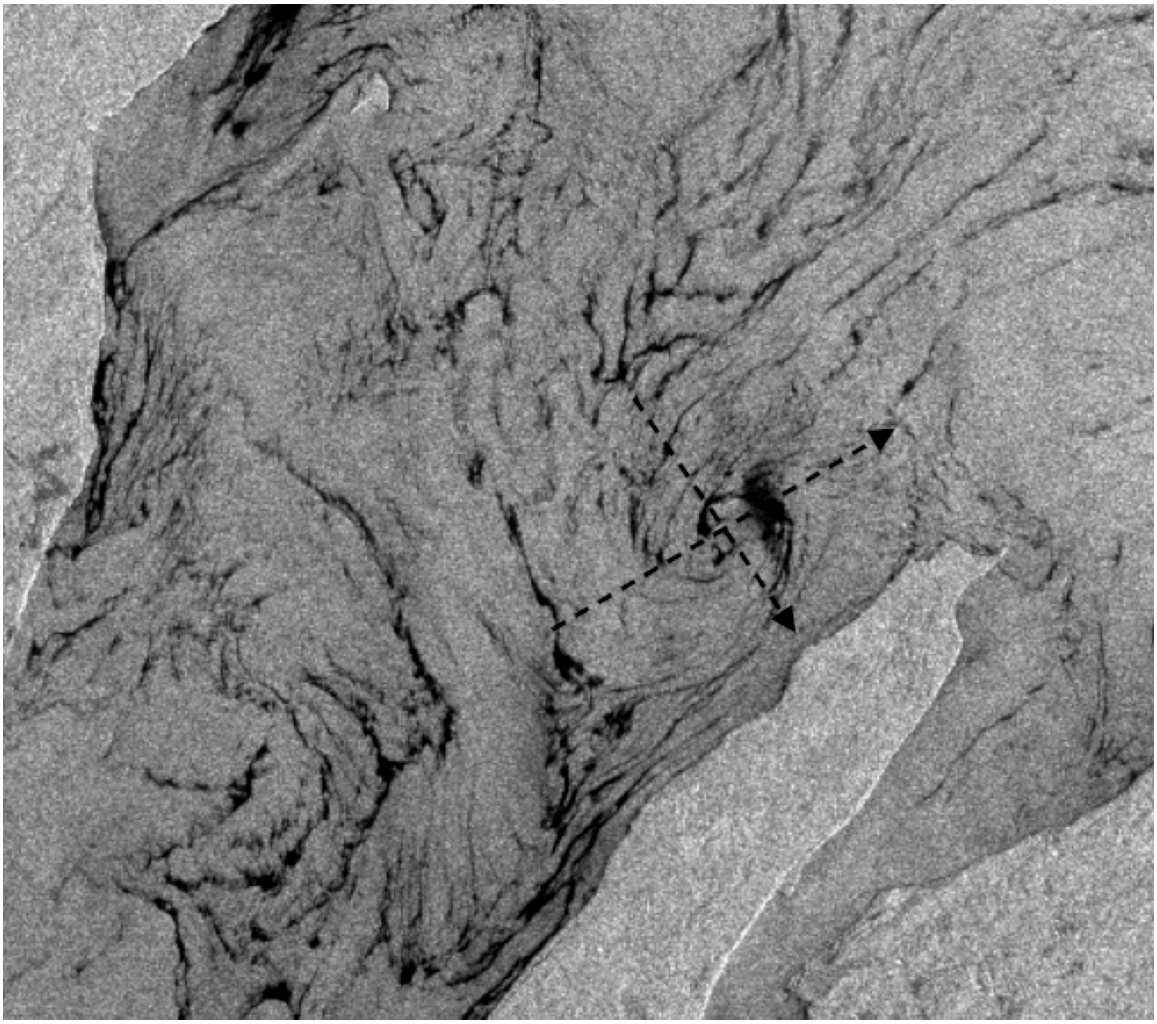

Figure 2: ERS-1 SAR image of an 8 km diameter Lake Superior coastal eddy shows how eddies are measured. Eddy diameter was calculated as the average of the major and minor axes. The distance to shore was measured from the eddy center. See text. The image was acquired on July 23, 1993, at 16:44:19 UTC, corresponding to local time 12:44:19 EDT. All SAR images copyright European Space Agency.

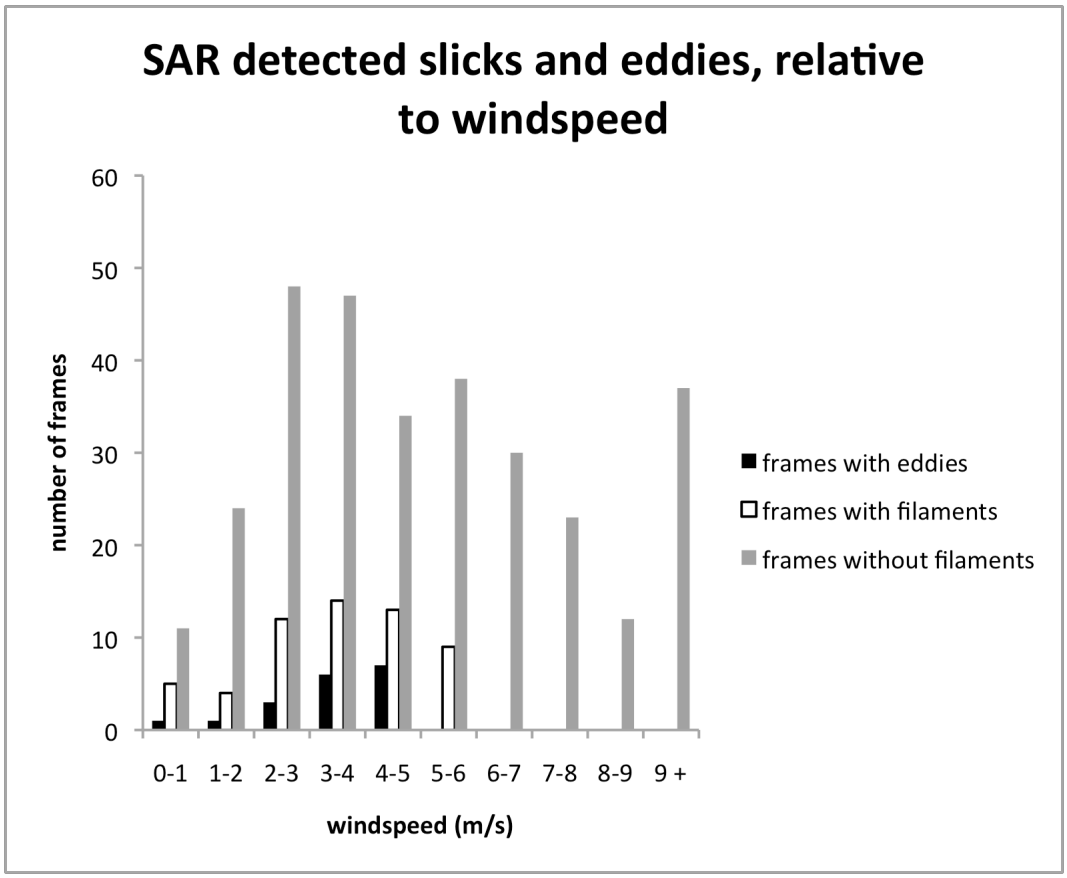

Figure 3. Distribution of wind speeds for SAR frames. No slicks or eddies were observed over 6 m s^{-1}.

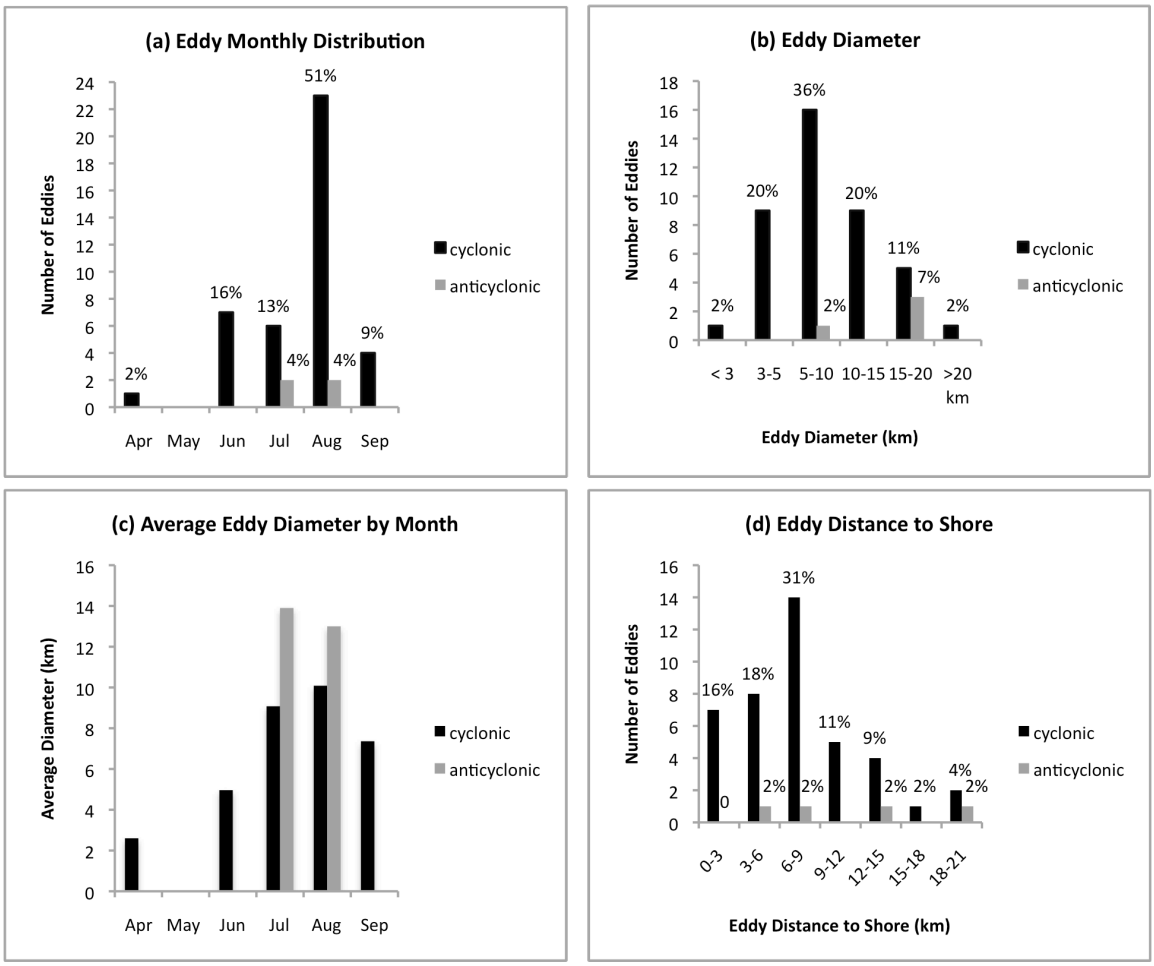

Figure 4. Statistics of eddy measurements in SAR images of Lake Superior. (a) Monthly distribution of eddies in April-November 1992-1998. Fifty five percent of the eddies were observed in August. (b) Distribution of eddy diameters. (c) Average eddy diameter by month. (d) Eddy distance to shore. Anticyclonic eddies were on average further from shore.

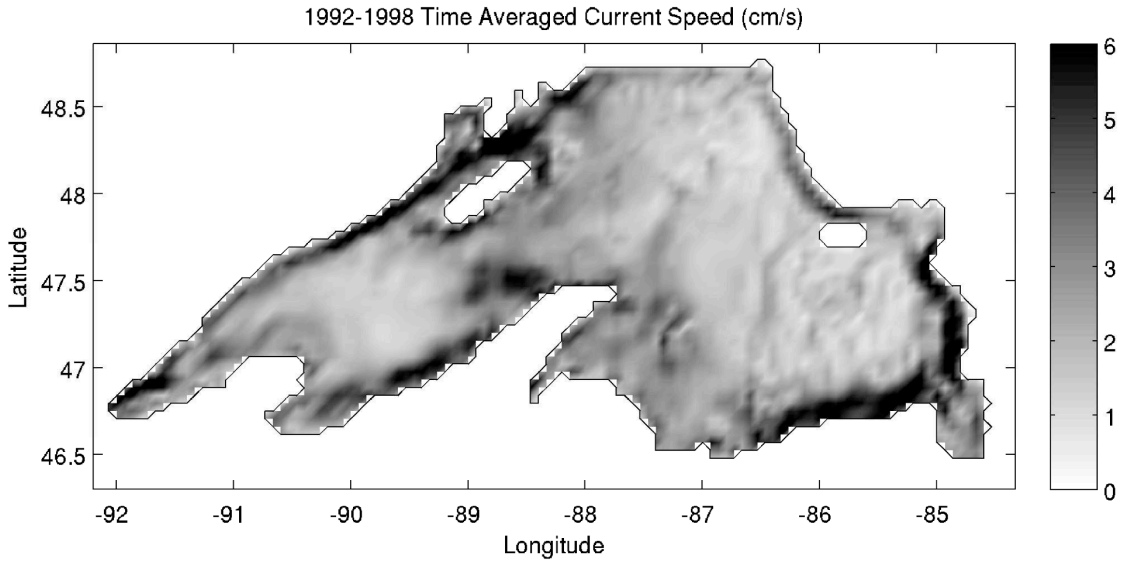

Figure 5. Mean August surface current speed in Lake Superior 1992-1998. Current speed in the top 10 m over 1992-1998 period from the Lake Superior model of White et al. (2012). Unit is cm s^{-1}. Note the higher speeds in the lake perimeter reflecting strong cyclonic coastal currents.

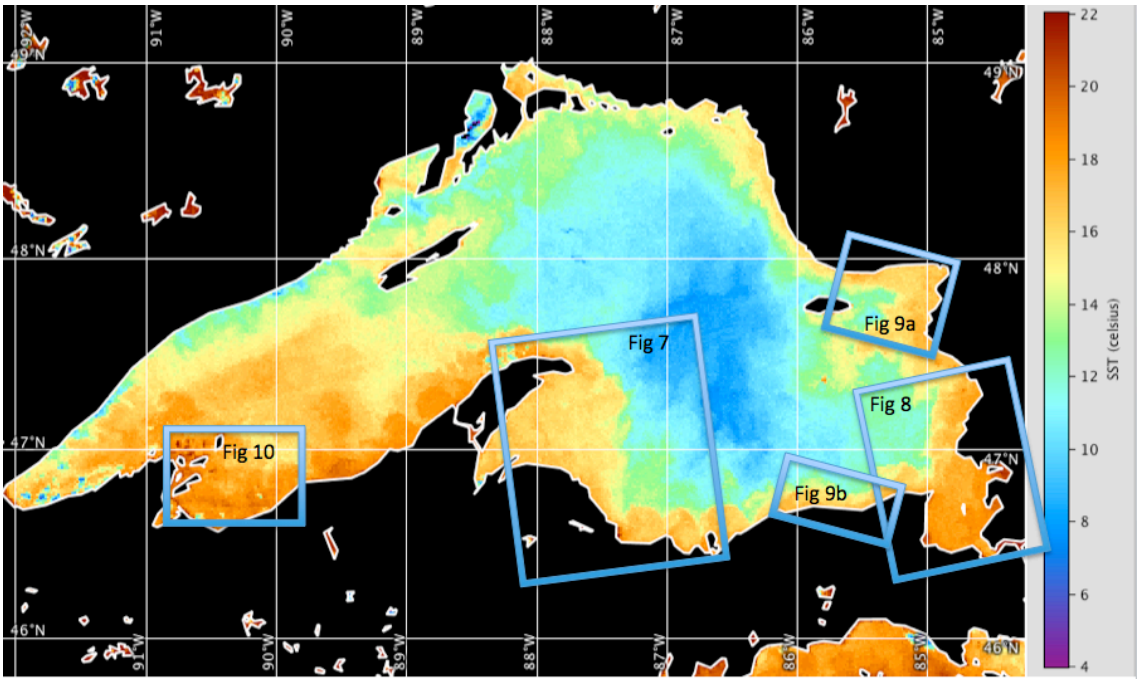

Figure 6. AVHRR image showing Lake Superior water temperatures. Image from August 22, 1994, a typical summertime pattern. The warm coastal boundary layer is clearly seen. Time of acquisition is 22:03 UTC. The corresponding local time is 18:03 in the central and eastern parts of the lake, and 17:03 in southwestern part of the lake. The temperature gradient between coastal and offshore waters at the tip of the Keweenaw Peninsula, determined with the CDAT image analysis tool, reaches a maximum of 3 °C km^{-1} 10 km offshore. The labeled boxes indicate the approximate areas covered by Figures 1.7 – 1.10.

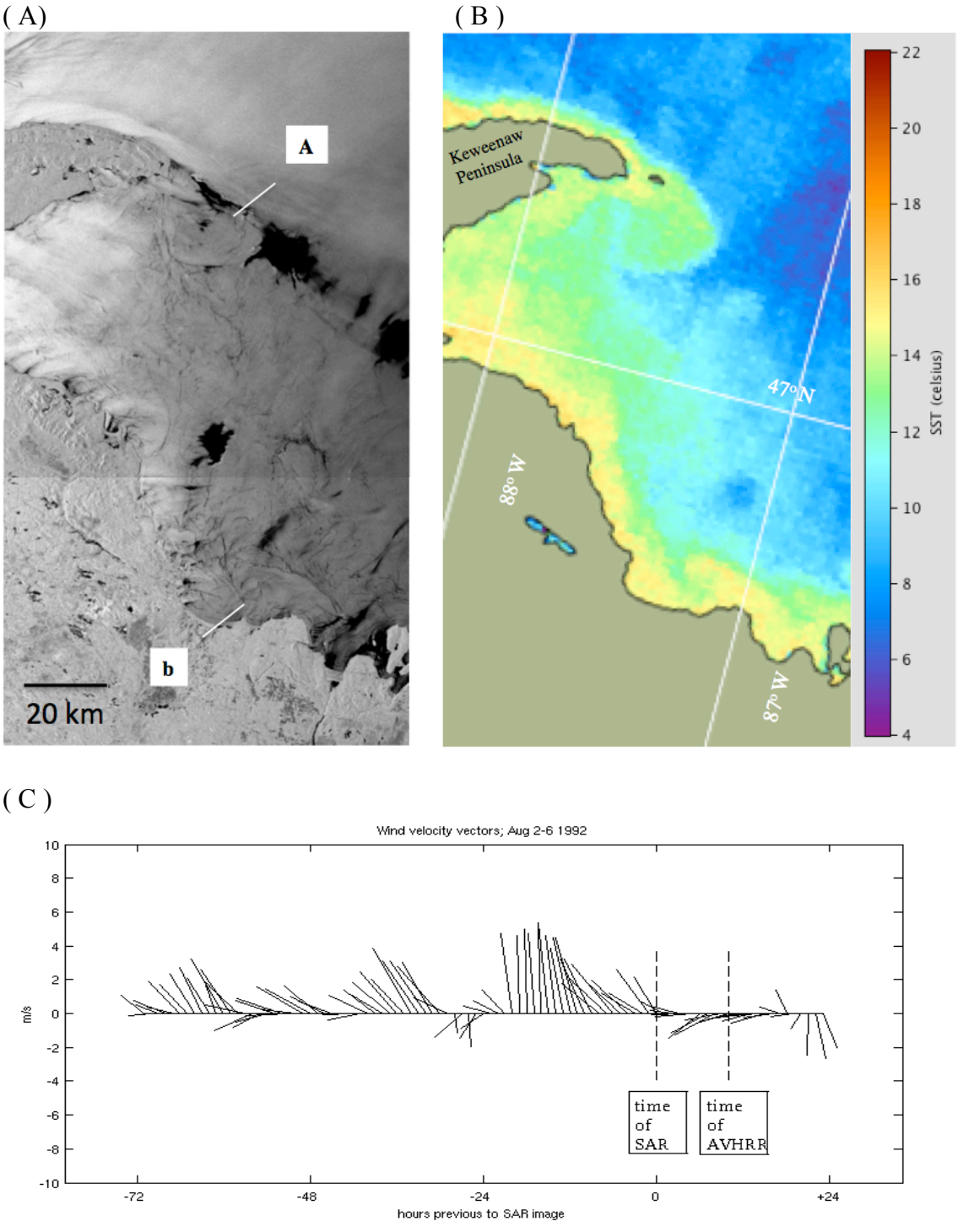

Figure 7. Eddy example 1; August 5, 1992 SAR and AVHRR images. Nearly coincident ERS-1 SAR (A) and AVHRR (B) images show a 19 km diameter anticyclonic eddy “a” 21 km from the tip of the Keweenaw Peninsula. SAR acquired August 5, 1992,

at 3:58 UTC, local time August 4, 1992, 23:58 EDT. AVHRR acquired August 5, 1992, at 9:43 UTC, local time 5:43 EDT. A 17 km diameter cyclonic eddy “b” is centered 8 km from shore. Hourly wind data (C) from the eastern buoy, NDBC number 45004, is shown beginning 72 hours prior to the time of SAR acquisition to 24 hours afterwards. Vectors indicate direction wind is from. See text for discussion. SAR image copyright European Space Agency.

(A)

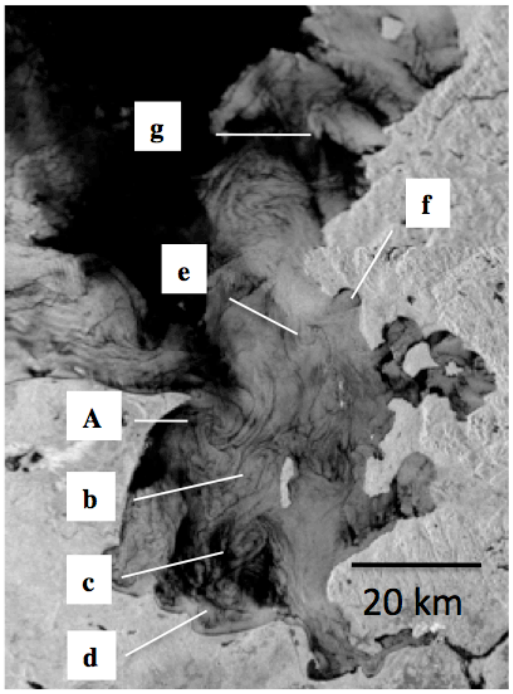

(B)

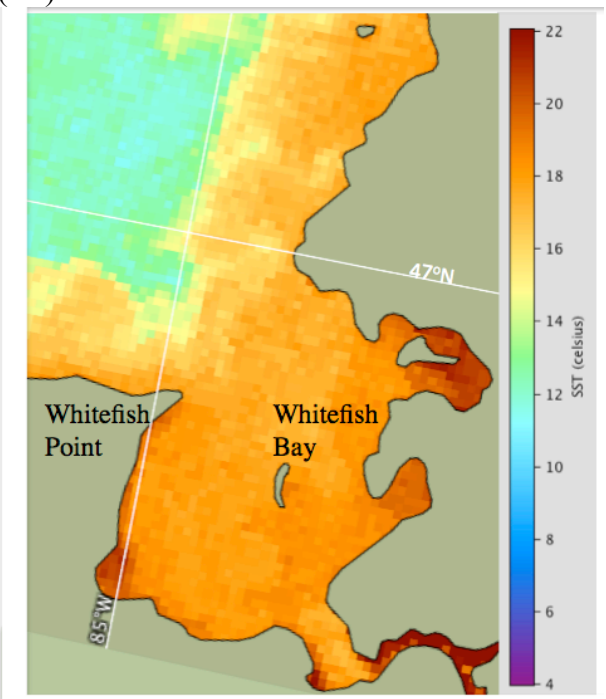

(C)

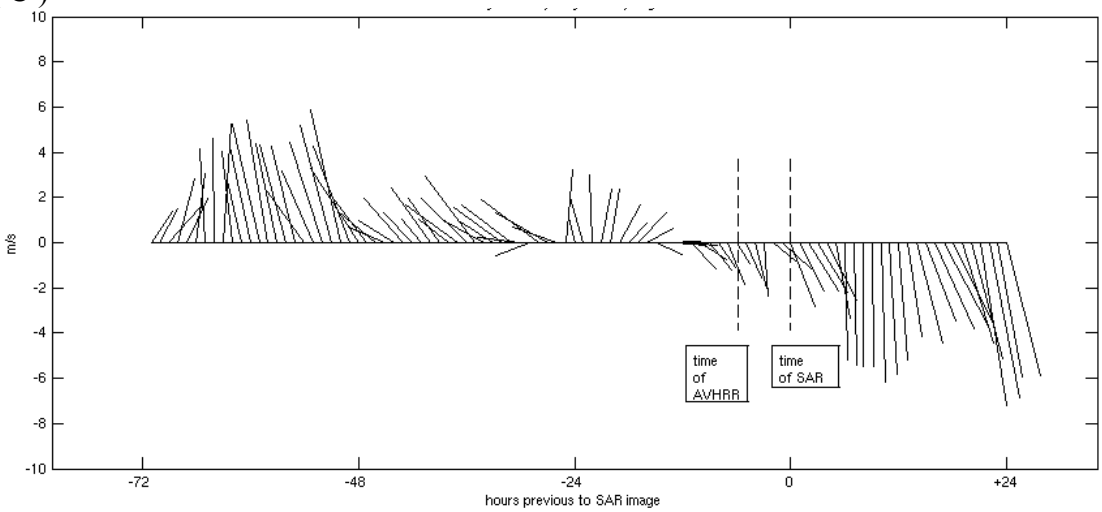

Figure 8. Eddy example 2; August 23, 1994 SAR and AVHRR images. Multiple eddies in Whitefish Bay are visible in ERS-1 SAR (A). SAR acquisition August 23, 1994, at 3:48:05 UTC. Local time is August 22, 1994, 23:58:05 EDT. Small temperature differences in this area reduce the visibility of the features in the nearly coincident AVHRR image (B). AVHRR acquisition August 22, 1994, at 22:03 UTC, local time 18:03 EDT. A 20 km anticyclonic eddy "A" is located in the lee of Whitefish Point where the prevailing cyclonic coastal current enters the bay. Other eddies "b"- "g" are cyclonic and range from 4.8 km diameter "f" to 9.45 km "d". Hourly wind data (C) from the eastern buoy, NDBC number 45004, is shown beginning 72 hours prior to the time of SAR acquisition to 24 hours afterwards. Vectors indicate direction wind is from. See text for discussion. SAR image copyright European Space Agency.

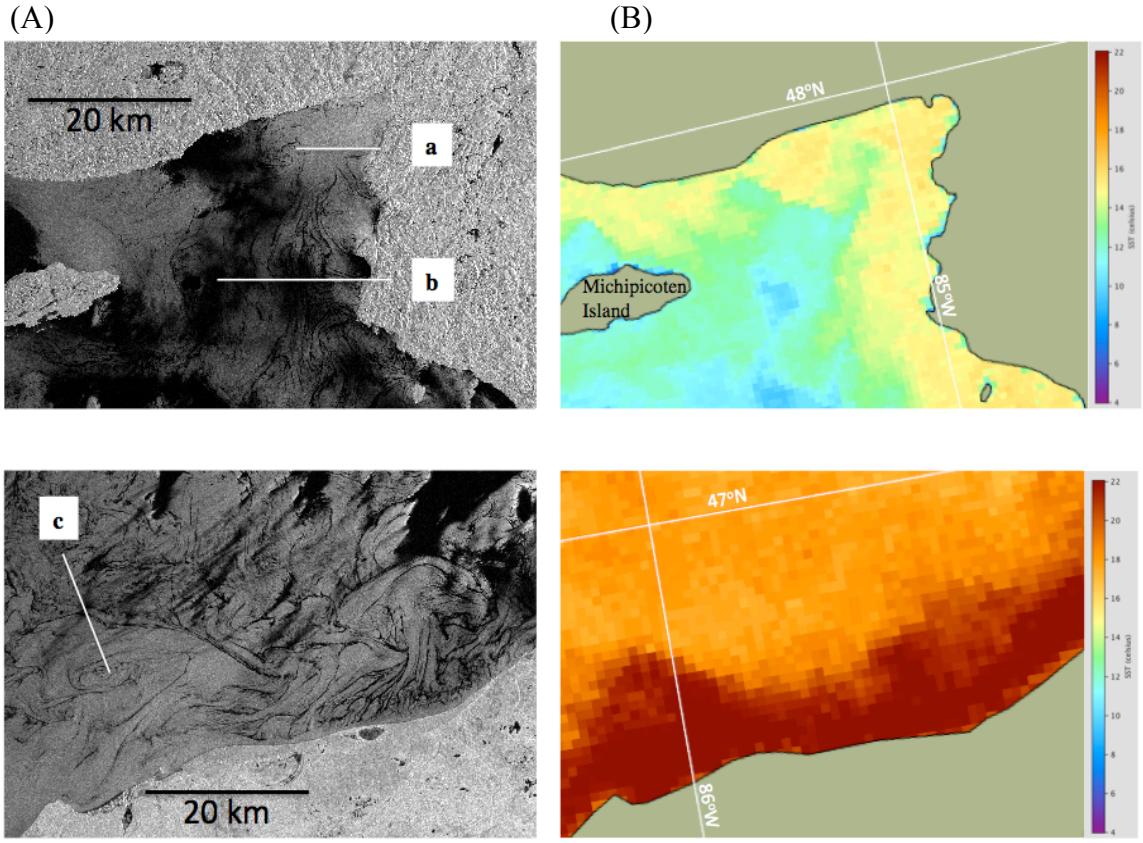

(C)

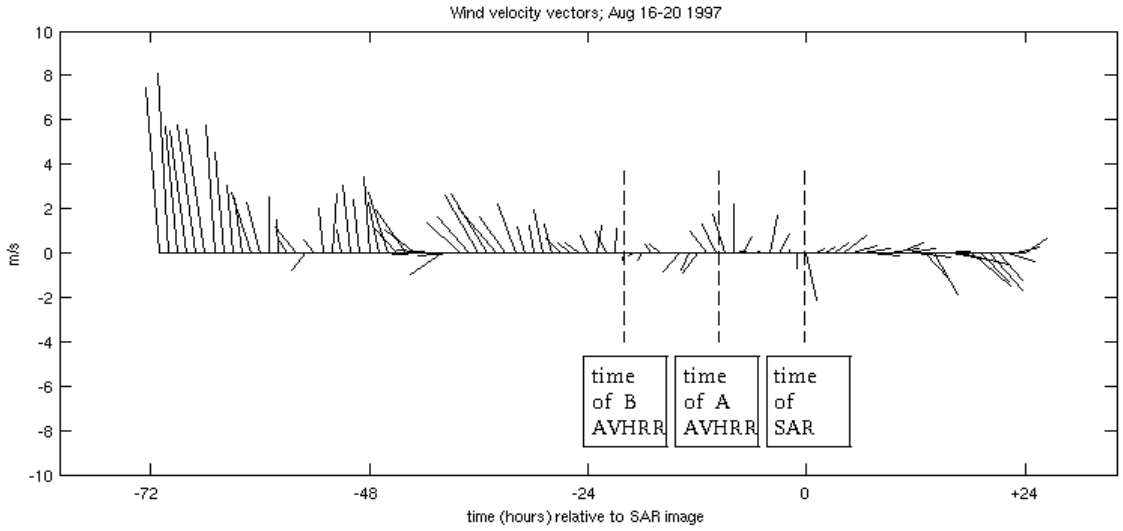

Figure 9. Eddy example 3; August 19, 1997 SAR and AVHRR images. Filaments and eddies are visible in ERS-2 SAR (left) images of the northern (A) and southern (B) shore of eastern Lake Superior. SAR acquisition August 19, 1997, at 16:32:36 UTC (northern, A) and August 19, 1997, at 16:32:51 (southern, B). The corresponding local time is 12:32 EDT. Temperature differences between nearshore and offshore in the areas are shown in the nearly coincident AVHRR images (right). AVHRR acquisition August 19,1997 at 8:18 UTC (4:18 EDT) (northern, A) and August 19, 1997 at 22:57 UTC (18:57 EDT) (southern, B). Hourly wind data (C) from the eastern buoy, NDBC number 45004, is shown beginning 72 hours prior to the time of SAR acquisition to 24 hours afterwards. Vectors indicate direction wind is from. See text for discussion. SAR image copyright European Space Agency.

(A)

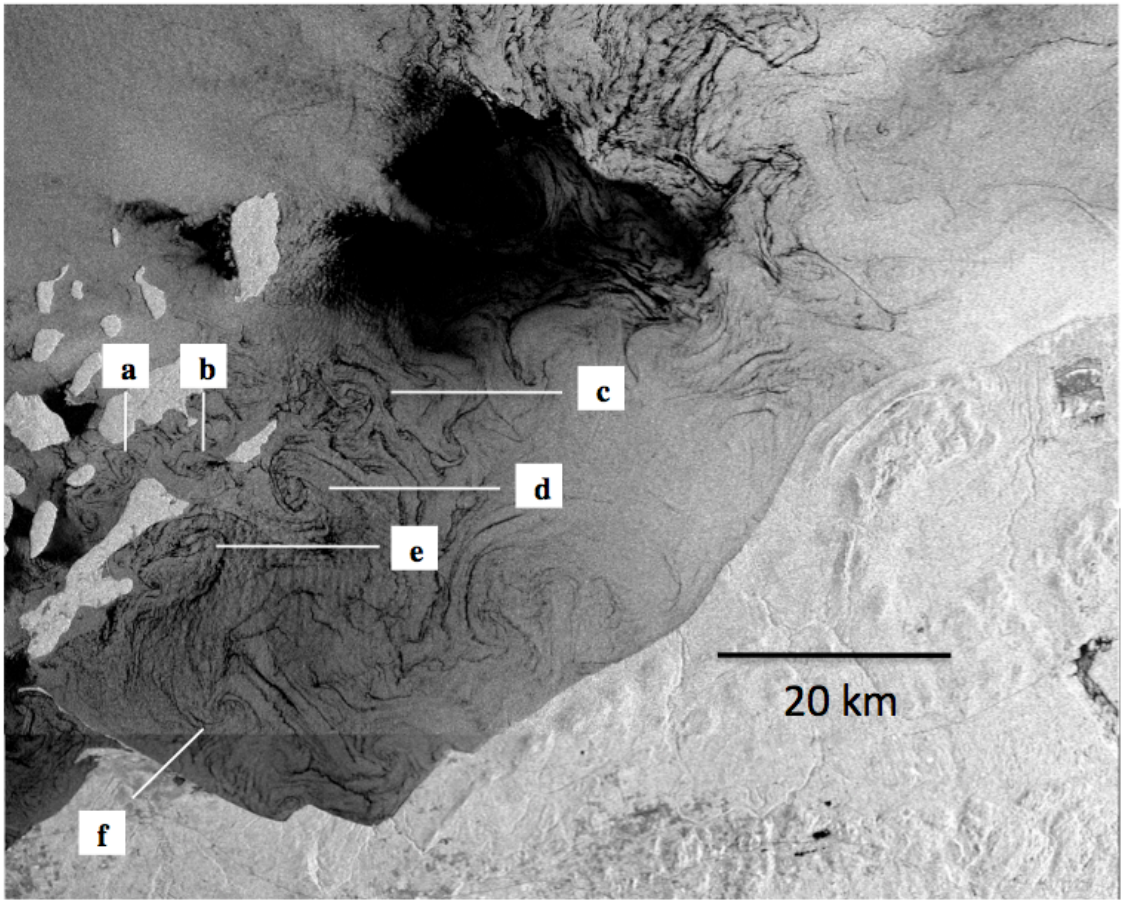

(B)

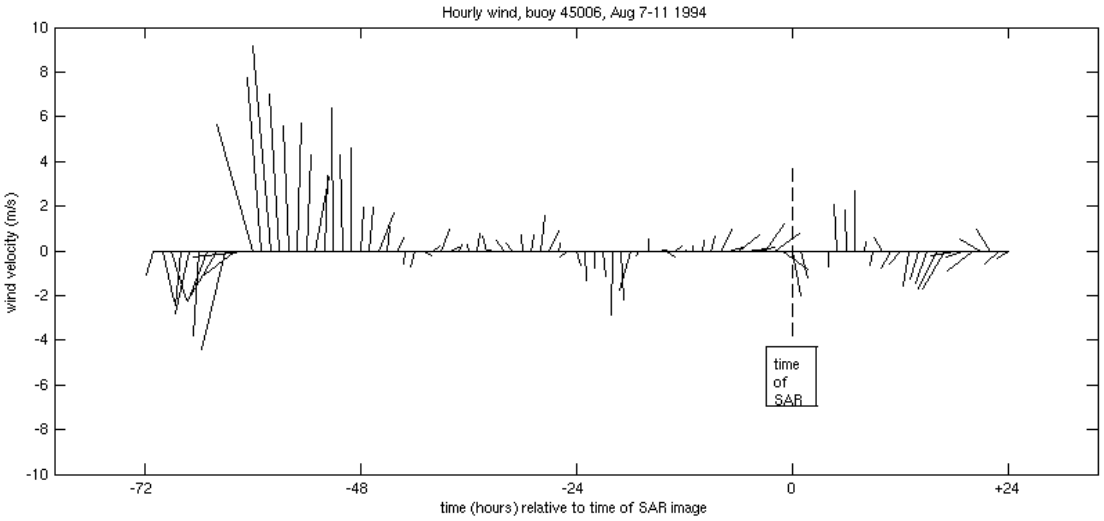

Figure 10. Figure 10. Eddy example 4; August 10, 1994 SAR image. Multiple small eddies are visible in the ERS-1 SAR image from the Apostle Islands area (A). SAR

acquisition August 10, 1994, at 16:51 UTC. The corresponding local time is 11:51 CDT. No corresponding AVHRR image is available due to cloud cover. Eddy sizes range from 3.5 to 13 km in diameter. Hourly wind data (B) from the western buoy, NDBC number 45006, is shown beginning 72 hours prior to the time of SAR to 24 hours afterwards. Vectors indicate direction wind is from. See text for discussion. SAR image copyright European Space Agency.

Chapter 3: Formation and offshore migration of the springtime thermal bar; a numerical model sensitivity study.

Introduction

The thermal bar is a temperature front that forms in dimictic lakes in spring and fall when the nearshore-offshore surface temperature gradient spans freshwater's temperature of maximum density (T_{md}), roughly 4 °C (Ullman et al., 1998). First described by Forel (1880) in Lake Leman, thermal bars have been the subject of studies in Lake Ladoga (Tikhomirov, 1963; Malm et al., 1993, 1994), Baikal (Likhoshway et al., 1996), Ontario (Rodgers, 1966; Gbah and Murthy, 1998) Michigan (Moll et al., 1993; Consi et al., 2009) and Superior (Hubbard and Spain, 1973; Auer and Gatzke, 2004). A review of thermal bar research is presented in Holland and Kay (2003).

In response to seasonal changes in surface heat flux, shallower nearshore waters reach T_{md} and stratify before deeper areas offshore, and a downwelling plume of water at T_{md} (the 'bar') forms at the convergence as a result of cabelling instability (Kantha and Clayson, 2000). In spring, surface temperatures inshore of the thermal bar front are above T_{md}, while offshore they are below. Due to freshwater's nonlinear equation of state, both are less dense than the 4 °C water which forms at their convergence as a result of lateral mixing. In fall, temperatures on either side of the bar are reversed. Seasonal cooling leads to inverse stratification in shallow areas first, with surface temperatures below T_{md}.

In addition to its characteristic surface temperature expression, the location of the thermal bar can be identified by a sharp contrast in the appearance of the surface water (Figure 1), and high concentrations of floating detritus (Appendix 1). In remotely sensed images of lake surface temperature, closely packed isotherms associated with the front are typically aligned parallel to shore along bathymetric contours (Figure 2a, Figure 2b). The frontal boundary is also visible in remotely sensed Synthetic Aperture Radar (SAR) images due to contrasts in air-sea interactions over the frontal zone as well as high concentrations of surfactants trapped in the convergent zone (Ivanov et al., 1995; McKinney et al., 2012).

The presence of the thermal bar inhibits exchange between nearshore and offshore water masses due the downwelling plume of water at T_{md} and the coastal circulation induced by the horizontal density gradient (Holland and Kay, 2003). The circulation consists of geostrophic, shore parallel flow that travels counterclockwise inshore of the front and an opposing clockwise flow offshore.

This report presents the results of a sensitivity analysis conducted with idealized configurations of a three dimensional numerical model of lake hydrodynamics. The objective of the sensitivity analysis was to predict the range of dates over which thermal bars affect nearshore to offshore exchange in Lake Superior. We focus on the role played by meteorological parameters, bottom slope and initial water temperature, although near river mouths, interannual differences in the volume of runoff can affect the date when thermal bars form (Moll et al., 1993; Rodgers, 1966; Auer and Gatzke, 2004).

The model is based on the Regional Ocean Modeling System (ROMS) (Shchepetkin and McWilliams, 2005), which was previously configured to simulate the thermal cycle and deep chlorophyll maximum of Lake Superior (White et al., 2012; White and Matsumoto, 2012; Matsumoto et al., 2015). In this study, ROMS is applied to idealized, circular model domains with parabolic depth profiles characteristic of nearshore bottom slopes in Lake Superior. Results from the idealized cases will inform subsequent numerical modeling using a realistically configured ROMS of the entire lake. In the following section, the model configuration is presented, followed by results, discussion and conclusion.

Data and Methods

Simulations were carried out using three idealized lake basins. Each circular basin was 100 km in diameter with minimum depth of 8 m in the perimeter of the basin. Maximum depths were 125 m (shallow basin), 250 m (intermediate basin) and 500 m (deep basin) (Table 1). Large lakes, including Superior, typically have numerous embayments. To investigate their effect on thermal bar formation, a fourth idealized basin was designed by adding a flat-bottomed, 10 by 20 km embayment to the western boundary of the 250 m depth basin. The depth of the embayment was 10 m.

ROMS uses an orthogonal computational grid and terrain following (sigma) vertical coordinate system. The horizontal grid spacing in each of the model domains was set to 1 km. The vertical grid used 20 sigma layers, concentrated in the top 50 m to resolve surface processes. Following other freshwater applications of ROMS (Austin and

Allen, 2011; White et al., 2012) the model used an equation of state developed specifically for freshwater (Chen and Millero, 1986). The Coriolis parameter was set at 10^{-4} s^{-1}, corresponding to the value at mid-latitudes. Sub grid scale turbulence was modeled using the Mellor-Yamada level 2.5 turbulence closure scheme.

Model forcing was prepared from three hour North American Regional Reanalysis (NARR) data for air temperature, specific humidity, downward shortwave and downward longwave radiation covering Lake Superior for the years 1979-1997. The data was obtained from the NARR website[4] and the mean, standard deviation and range of each parameter were calculated at each three hour interval. A simulation was conducted using the mean of each parameter and results were used as the control in the sensitivity analysis. Sensitivity simulations were carried out by varying each of the meteorological parameters (Figures 3a, 3b, 3c, 3d) and NARR wind from 1989 (Figure 4).

Fluxes of sensible and latent heat and momentum between the lake surface and the atmosphere were determined using the COARE (Coupled Ocean Atmosphere Response Experiment) bulk flux algorithm (Fairall et al., 1996). Total heat flux Q_{net} to the lake surface was determined by

$$Q_{net} = SW_{down} + LW_{net} + Q_{sensible} + Q_{latent} \qquad \text{Eq. (1)}$$

Shortwave radiation was attenuated within the water column using parameters of Jerlov water type 1 and shortwave radiative flux was approximated by NARR downward shortwave radiation, consistent with optically clear, oligotrophic waters with low albedo, as exist in Lake Superior. Net longwave radiation LW_{net} was determined as

[4] http://www.esrl.noaa.gov/psd/data/gridded/data.narr.monolevel.html

$$LW_{net} = LW_{down} - \varepsilon\sigma T_s^4 \qquad \text{Eq. (2)}$$

where the second term on the right is the upward longwave radiation and $\varepsilon = 0.97$ is the emissivity of the lake surface, $\sigma = 5.67 \times 10^{-8}$ $Wm^{-2}K^{-4}$ is the Stefan-Boltzmann constant and T_s is the surface temperature in Kelvin. Turbulent sensible heat flux $Q_{sensible}$ was determined using

$$Q_{sensible} = C_p \rho_A C_{st} (T_A - T_S) u_A \qquad \text{Eq. (3)}$$

where C_p is the specific heat of water, ρ_A is the density of air, C_{st} is a stability function determined using the Monin-Obukhov similarity parameters of Liu et al. (1979), T_A is the air temperature, T_S is the surface temperature and u_A is the windspeed. Turbulent latent heat flux Q_{latent} was determined using

$$Q_{latent} = L \rho_A C_{st} (q_z - q_0) u_A \qquad \text{Eq. (4)}$$

where L is the latent heat of water and q_z is the specific humidity measured at 2 m above the water's surface, and q_0 is the specific humidity of saturated air at the temperature of the water surface.

The offshore position of the thermal bar was determined by averaging the distance from the western, eastern, southern and northern boundaries of the idealized lake basins to where the temperature of the top 1 m of the water column was 4 °C. The influence of the thermal bar on cross shelf exchange was investigated by adding a conservative, passive dye tracer throughout a 10 by 20 grid cell area of the western boundary at the beginning of each model run. In the grid that included an embayment, the tracer was added to the entire embayment.

Results and Discussion

Figure 5 shows the thermal bar distance offshore for each basin, using the control forcing. The thermal bar formed first and moved offshore at the fastest rate in the shallow basin (Figure 5, dotted line). Visual analysis of the plot suggests the initial rate of offshore migration was approximately 0.5 km day^{-1} until model day 35, when the thermal bar was approximately 15 km from shore. After day 35, the speed increased, and the thermal bar moved the final 30 km to the lake center over 15 days. A similar increase occurred in the intermediate depth basin (Figure 5, solid line), where the initial migration to 15 km offshore occurred over 35 days. In the later stage, the thermal bar moved from 15 km to 45 km over 15 days. In the case of the deep basin (Figure 5, dash-dot line) the thermal bar formed around day 40 and moved to a distance 20 km offshore over the following 50 days, which was the end of the simulation.

Models and observations indicate thermal bars move offshore in two stages, an initial slow stage, and a late fast stage (e.g. Farrow, 1995). The speed increases in the late stage due to additional heating at the frontal boundary from warm water advected from behind (shoreward). This contrasts with the slower initial stage in which the rate is explained by simple analytical models that consider only surface heat flux, bathymetry and initial water temperature. For example, Elliot (1971) showed the heat Q_s required to change the temperature of a well-mixed layer of thickness h by ΔT is described by

$$Q_s = \rho C_p h \Delta T \qquad \text{Eq. (5)}$$

per square meter, where C_p and ρ are the heat capacity and density of water, and ΔT is the difference between 4 °C and the water temperature at the beginning of the heating

season. The rate R at which the thermal bar moves offshore is likewise described by

$$R = Q_{sfl\ u\ell} / \rho C_p \Delta T s \qquad \text{Eq. (6)}$$

where $Q_{sfl\ u}$ is the surface heat flux and s is the bottom slope.

Table 2 compares the thermal bar position in each of the idealized basin after 50 days to the position predicted by the simple analytical model described by Eqs. (5) and (6). In each case, the simulated thermal bar is further from shore than predicted. The difference indicates that by this time, the thermal bars in each of the basins have entered the late, fast stage of their offshore migration.

Figure 6 shows surface temperature (contours) and concentration of passive tracer in each idealized lake basin at the same timestep, corresponding to model day 50 (May 20). The location of the 4 °C isotherm, the thermal bar, is indicated by the white line. Surface temperatures inshore of the thermal bar are warmer indicating the seasonal density stratification in the nearshore areas. In the shallow-sloping basin (Figures 6a, 6b), the thermal bar has advanced to approximately 40 km offshore, and the passive tracer is distributed in the southwest quarter, to an offshore distance of 20 km. A small amount of tracer is located clockwise from the starting point, close to shore. In the intermediate basin (Figures 6c, 6d), the thermal bar has advanced approximately 15 km offshore. The tracer distribution shoreward of the thermal bar indicates circulation travels in two directions. From shore to approximately halfway to the thermal bar, the tracer has moved clockwise, to the north, whereas the outer half has spread counterclockwise, to the southwest. In the deep basin (Figures 6e, 6f), the thermal bar has advanced less than 10 km from shore, and the tracer shows a completely different pattern, in which it has

crossed the thermal bar into the unstratified central lake area. The thermal bar itself meanders and instabilities occur along the leading edge of the front in the western half of the domain.

Additional images of the intermediate basin (not shown) indicated that before the thermal bar formed, the dye spread along shore under the influence of wind and was well mixed vertically. After the thermal bar formed, it moved offshore where it encountered the dye patch. Inshore dye concentration increased and offshore concentration decreased due to entrainment of offshore water in the convergence and downwelling, until all the dye was inshore of the front and concentrated below the thermocline. Downwelling is also evident in the orientation of isotherms in the area shoreward of the 4 °C front. The zone of downwelling approximately halfway from shore to the front was also observed in a field survey of the thermal bar in Lake Superior (Appendix 1).

In the field, identifying the position of the thermal bar is complicated by meanders and eddies that form on the frontal boundary (e.g. Rao et al., 2004; Hubbard and Spain, 1973). Similar meanders are evident in the simulation using the deep basin (Figure 6e). There, the dye distribution suggests the front is an active area of stirring and mixing rather than a barrier. In addition, the simple analytical model was least predictive in this basin (Table 2).

To assess the contribution of frontal instabilities to the offshore migration of the thermal bar, model results were evaluated using an eddy detection algorithm which locates eddies in ROMS output using the geometry of the current vectors (Nencioli et al.,

2010). Figure 7 shows the cumulative number of eddies in each basin, and confirms eddy numbers are higher in the deep basin where the frontal boundary is more sinuous.

The results above are consistent with models and observations of the thermal bar that reveal advection of heat from behind the thermal bar is important in the latter stages, and increases the rate of migration (e.g. Farrow, 1995). We hypothesized the presence of an embayment would provide additional warm water that could increase the rate of thermal bar migration during the fast stage above the rate in a similar basin without an embayment. To evaluate this hypothesis, the offshore distance of the thermal bar in the basin that included an embayment was compared to the round basin with similar bottom slope (Figure 8a, 8b).

Within the embayment, surface temperatures exceed 12 °C and the thermal bar was 25 km from the western shore, or 15 km into the main lake. In the basin with no embayment, the thermal bar was 1.5 km closer to shore. The depth averaged temperature inshore of the thermal bar was 6.2 °C for the grid that includes the embayment, and 6.0 °C for the circular basin. Average surface temperatures were 7.5 and 7.0 °C. Temperature contours in map view showed lake water intruded into the embayment in the south, and warmer embayment water exited from the north. Forcing for both runs was identical, suggesting exchange of warm embayment water to the main lake contributed to the offshore progress of the thermal bar. This effect would be important for nearshore water quality near embayments, where faster progress of the thermal bar away from shore would mitigate the negative effects of trapped runoff.

To investigate the relationship between meteorological parameters and the position of the thermal bar, we first compared the surface heat flux on the convecting side of the thermal bar under each forcing scenario. Each meteorological parameter contributes to the total heat flux as discussed in the methods section above and Eqs. 1-4. Shortwave radiation in units of W m^{-2} contributes directly to surface heat flux in the model, whereas net fluxes of longwave radiation, sensible heat and latent heat are functions of surface water temperature. Note that the value we used for water temperature in determining these fluxes was not an independent variable, but was a function of the model itself.

In each perturbation simulation, one of the four meteorological parameters was changed by an amount that was based on our statistical analysis of NARR data. For example, the $+\sigma$ perturbation to air temperature forcing is on average, 3.8 °C higher than the control value (Fig. 3c), and is statistically as likely as the $+\sigma$ perturbation to shortwave radiation, which is 77 W m^{-2} greater, on average, than the control value (Figure 3b). The minimum and maximum values captured the full range of variability of each parameter in the NARR-based climatology, similar to a 3 sigma change. Of all the perturbations, the minimum shortwave caused the largest drop in net surface heat flux relative to the control simulation (not shown). The values in the minimum shortwave perturbation run were 170 W m^{-2} lower on average than the control, a decrease in over 50% of the total heat flux.

Wilson et al. (2013) estimated the NARR shortwave radiation value has a positive bias of 50 W m^{-2} over Lake Ontario, due to underestimating cloud cover. Accounting for

the bias by lowering the shortwave radiation flux would lengthen the time required for the thermal bar to form. The bias would not affect the maximum solar heat flux perturbation since it represents cloudless conditions. The same underestimate of cloud cover has the opposite effect on downward longwave radiation. Markovic et al. (2009) found downward longwave radiation was underestimated by ~10 W m^{-2} in the NARR.

The presence of the thermal bar is most likely to affect nearshore water quality during the initial slow stage when it is close to shore. Figure 9 shows the time window in which the thermal bar is between 3 and 15 km from shore in each basin, and for each change to the meteorological inputs. In the shallow basin control simulation, the thermal bar is 3 km offshore on April 17 and moves offshore over the next 19 days, an average rate of 0.6 km d^{-1}. In the intermediate basin, it forms 4 days later, on April 21, and moves to 15 km offshore over the next 31 days, an average rate of 0.4 km d^{-1}. In the deep basin it forms on May 11, and moves offshore over 33 days, an average rate of 0.4 km d^{-1}. Taken as a whole, these results show that within a lake where nearshore bottom slope ranges from to 0.004 to 0.02, a thermal bar will be nearshore somewhere within the lake where it can affect the nearshore distribution of nutrients and runoff from mid-April through mid-June under the control forcing, representing typical meteorological conditions. When the initial water temperature on April 1 was raised from 2 °C to 3 °C, this period was shortened from mid-April to mid-May, and when shortwave radiation was changed to values representing record minimums, it was lengthened from mid-May to mid-August.

For comparison, Figure 10 shows the results of observations of the first appearance and last appearance of the 4 °C isotherm at the surface of Lake Superior

between 2003-2011 from in-situ and remote sensing. The in-situ observations of first appearance dates are estimated from United States Geological Survey (USGS) data. Staff conduct annual surveys of lake state and fish abundance (Mark Vinson, personal communication). The last appearance in-situ dates are estimated from NDBC buoy 45004, deployed in the eastern basin of the lake during the ice free months. The satellite detected temperatures are based on analysis of ATSR data, and provided by NASA scientist (Michelle Gierach, personal communication). The two data sets illustrate the range of thermal bar appearance and disappearance over the 9 years and generally confirm the range of dates shown in Figure 9.

Summary and Conclusions

Variability in springtime air temperature, humidity, shortwave radiation and downward longwave radiation change the time window in which thermal bars exist in nearshore waters over a range of different bottom slopes characteristic of Lake Superior. Nearshore to offshore exchange is affected by the presence of thermal bars in two ways; through downwelling associated with the formation of water at T_{md} , and by the shore parallel flow that results from the horizontal temperature gradient. Simulations presented here were conducted using model domains with horizontal grid spacing of 1 km, too coarse to resolve thermal bar itself in detail, since it typically is on the scale of 100 m (Appendix 1). However, the model reproduced some interesting features of the circulation associated with thermal bars including the initial slow stage and the later fast stage, and offshore advection of nearshore dye tracer.

We treated the four meteorological parameters as independent variables although there are interactions between them. For example, downward longwave radiation is dependent on air temperature, and reductions in shortwave radiation imply additional cloud cover that was not included in the calculation of longwave radiation. The values we used for the meteorological parameters were taken from NARR, a "best-guess" of meteorological conditions based on observations and model results. NARR has positive (high) bias in air temperature (Bennington et al., 2010), shortwave radiation (Wilson et al., 2013) as well as a negative (low) bias for downward longwave radiation (Markovic et al., 2009). We also ran the model with idealized uniform temperatures, and began our forcing at April 1. Starting earlier or later would cause warming to be correspondingly slower or faster, based on the increase in surface heat flux over the springtime heating season.

Of the meteorological parameters, changes in shortwave radiation values caused the largest shifts in thermal bar position relative to the control, reflecting its status as the largest component surface heat flux during the springtime warming period. Reductions in shortwave radiation relative to the control caused the largest changes; thermal bars formed up to 40 days later and persisted up to 22 days longer in the nearshore waters between 3 and 15 km from shore.

A consequence for lakes is that the persistently cloudy years in which rainfall is most likely are also those in which thermal bars remain in shallow areas for a longer time. This would increase the effects of runoff on nearshore water quality relative to years where storm systems pass more frequently, with intervening sunny periods. This

effect may be more important in areas of steep bathymetry due to both the longer duration the thermal bar near shore in those areas in general and the lack of estuaries and low relief shoreline, which tend to act as a buffer and reduce direct runoff to the main lake.

Overall, changes to meteorological parameters were better predictors of thermal bar position in the shallow basin than in the deep basin due to frontal instabilities that formed in the deep basin. An eddy detection algorithm was applied to the model output and showed eddies formed more frequently in that basin. The contribution of horizontal advection behind the frontal boundary to the overall migration rate was also higher in that basin, suggesting the presence of eddies and meanders accelerates the thermal bar in the later stages of development in areas of steep bathymetry.

An additional simulation using a basin that included an embayment showed the migration rate during the latter stage of thermal bar migration depends on the coastal configuration behind the thermal bar. The embayment was a source of additional warm water that when advected into the main lake basin increased the horizontal thermal gradient and the distance of the thermal bar from shore relative to a basin without an embayment. This effect may play an important role in sustaining the nearshore to offshore thermal gradient and coastal circulation along the eastern shore of Lake Superior where numerous embayments are located.

TABLES

Basin	Radius	Maximum depth	Bottom slope (approximate)
Shallow	50 km	125 m	0.004
Intermediate	50 km	250 m	0.01
Deep	50 km	500 m	0.02

Table 1. Description of the three circular model domains. An additional basin was used in which a 10 kilometer wide by 20 kilometer long embayment was attached to the western boundary of the intermediate circular basin. Basins have parabolic depth contour so bottom slope is approximate.

				depth ave T=4		surface T=4	
	surface T	Qs (Wm^{-2})	predicted h (m)	h (m)	d offshore (km)	h (m)	d offshore (km)
shallow	2.7	189	97	108	32	112	34
intermediate	2.4	194	100	117	13.8	122	14.5
embayment	2.4	194	100	124	24.8	129	25.5
deep	2.2	196	101	129	7.6	145	8.5

Table 2. Thermal bar distance offshore; predicted value and model results. Position after 50 days of control forcing in each circular model domain. Predicted depth is calculated using (1), and time averaged surface heat flux (Q_s) from model results. Difference in Q_s is due to slight differences in surface temperature at basin centers reflecting different water column depths.

FIGURES

Figure 1. Photograph of Lake Superior thermal bar June 11, 2013. Photo shows the contrast in surface state that typifies the area of steep temperature gradient at the convergence of water masses with surface temperatures straddling freshwater's temperature of maximum density, roughly 4 °C. At the time the photo was taken, surface temperature on the inshore side of the slick (to the right) was 11 °C. Surface temperature within the slick approximately 100 m away, was below 6 °C. Surface temperature on the offshore side of the slick (not shown) was below 4 °C. Floating debris concentrated in the slick is mostly pine and spruce pollen. A year earlier, under different meteorological conditions, the thermal bar formed in this area along the Wisconsin shore east of Duluth a month earlier, in mid-May.

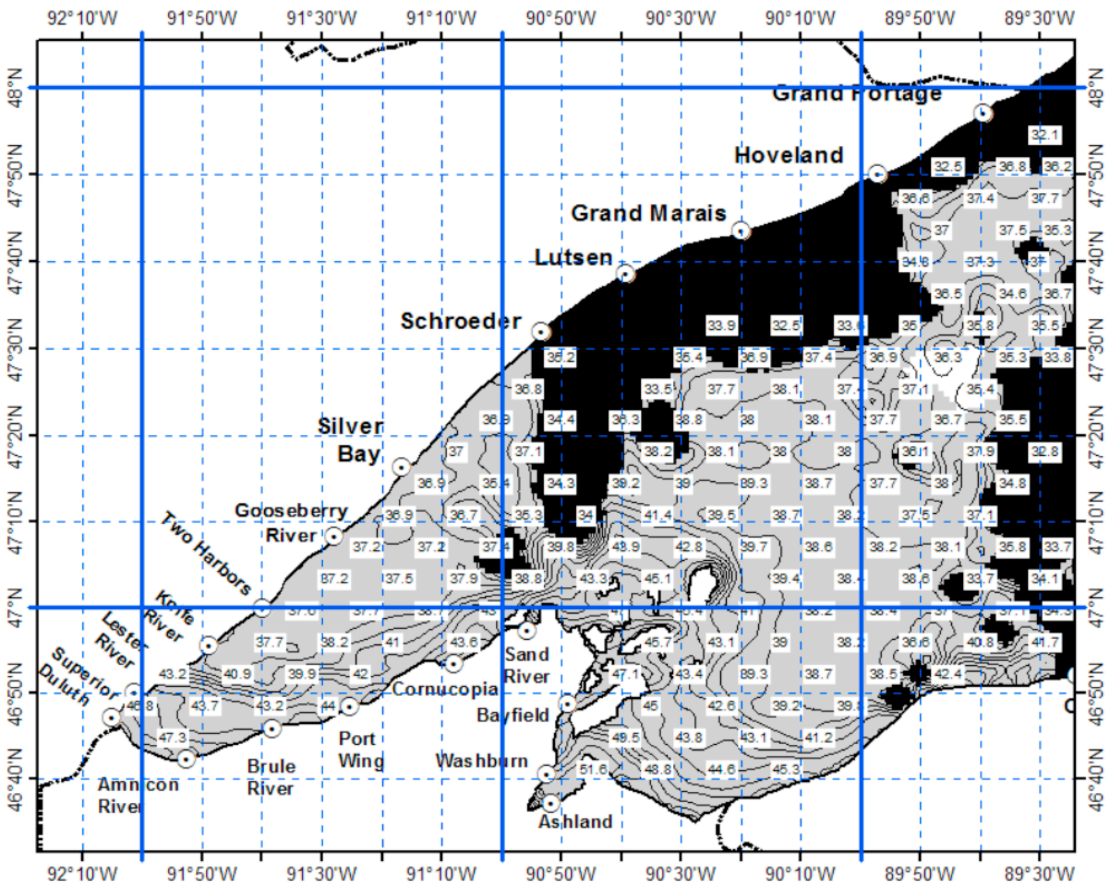

Figure 2a. Western Lake Superior AVHRR surface temperature; May 10, 2012. The high temperature gradient occurs on the shore side of the thermal bar, and follows nearshore depth contours. Nearshore temperatures are above T_{md} , (~ 39 °F) indicating seasonal stratification has set in there. Black regions indicate cloud cover. AVHRR images from NOAA/GLERL Coastwatch program, Michigan State University Remote Sensing and GIS Research and Outreach Services.

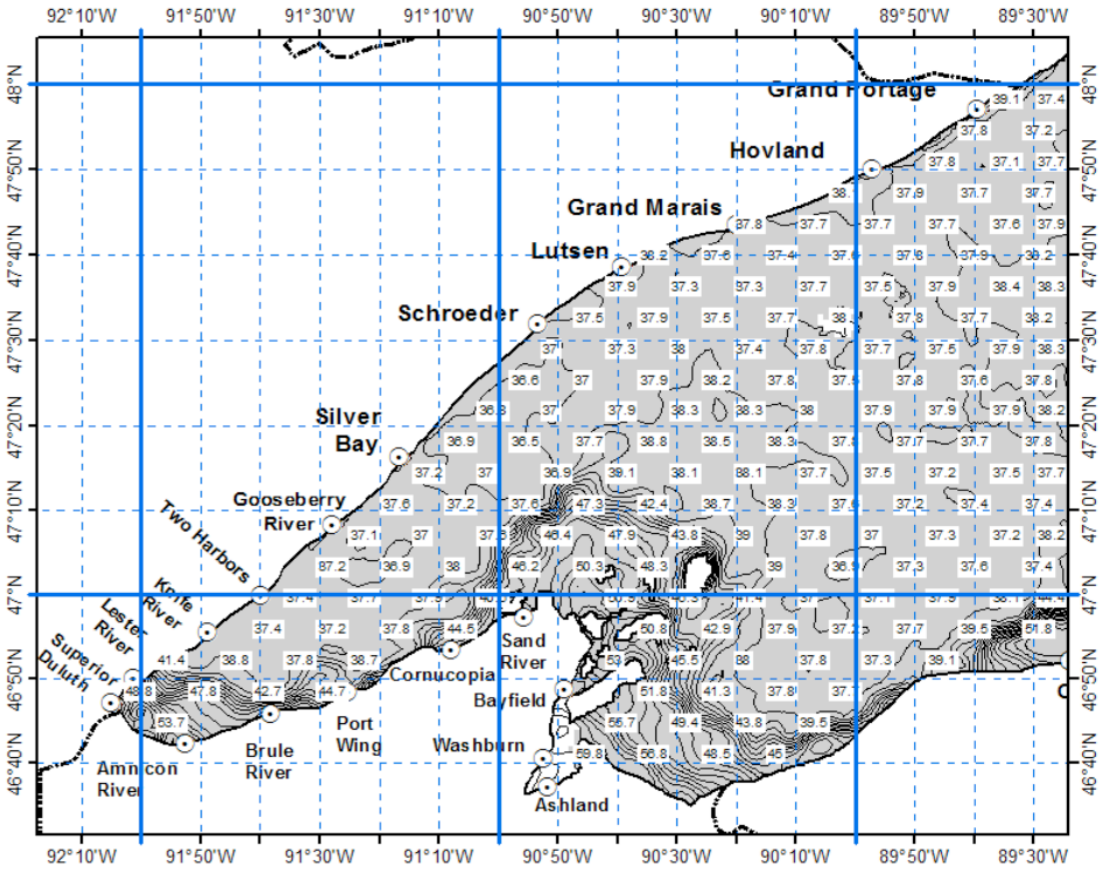

Figure 2b. Western Lake Superior AVHRR surface temperature; June 11, 2013. The high temperature gradient occurs on the shore side of the thermal bar, and follows nearshore depth contours. Nearshore temperatures are above T_{md} , (~ 39 °F) indicating seasonal stratification has set in there. AVHRR images from NOAA/GLERL Coastwatch program, Michigan State University Remote Sensing and GIS Research and Outreach Services.

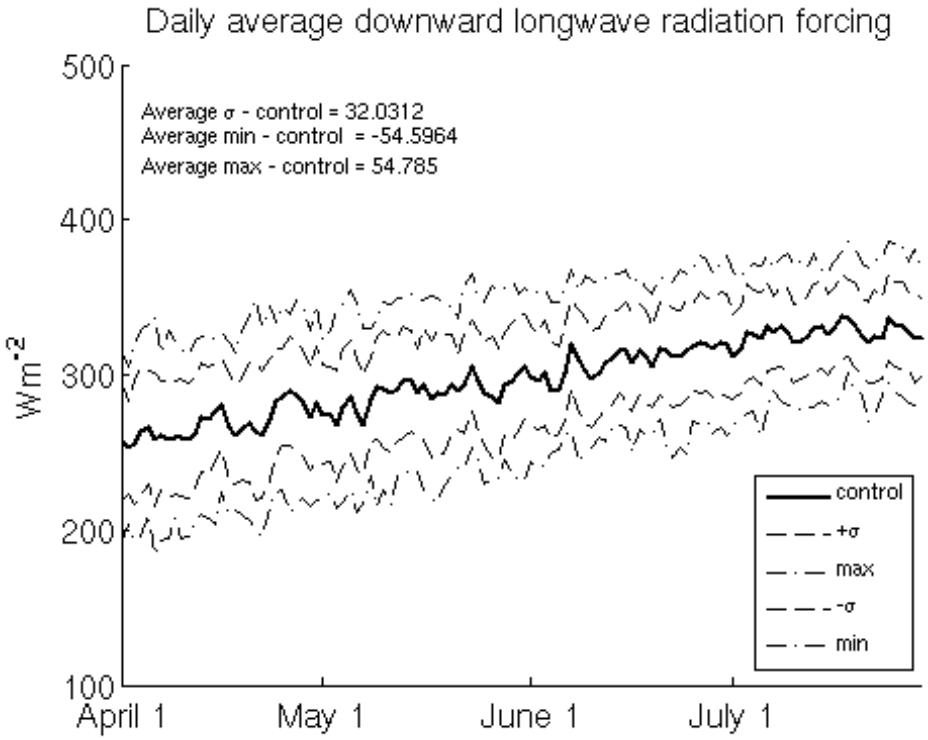

Figure 3a. Forcing used in the sensitivity simulations, longwave radiation.

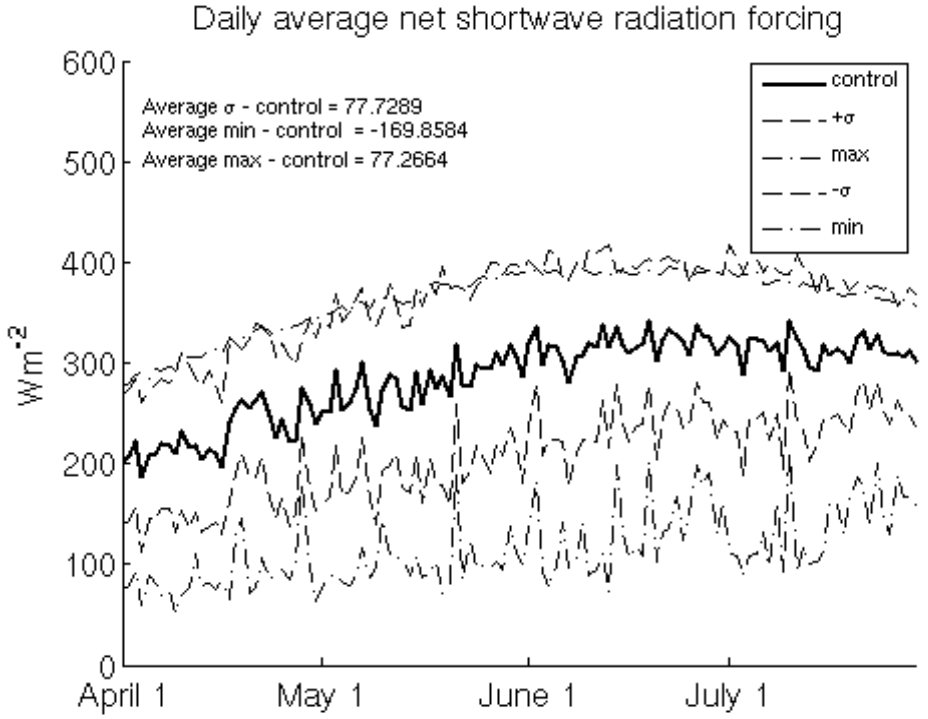

Figure 3b. Forcing used in the sensitivity simulations, shortwave radiation.

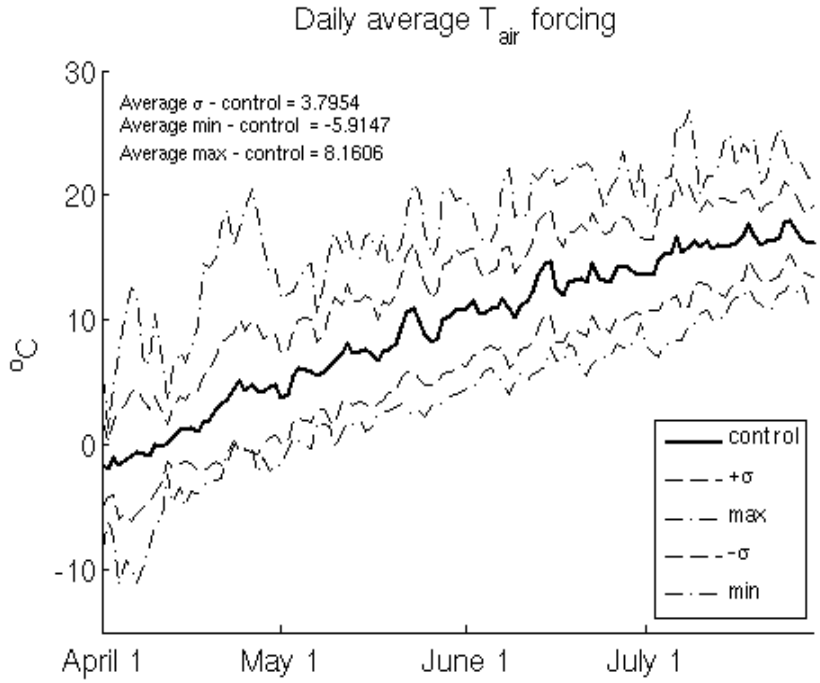

Figure 3c. Forcing used in the sensitivity simulations, air temperature.

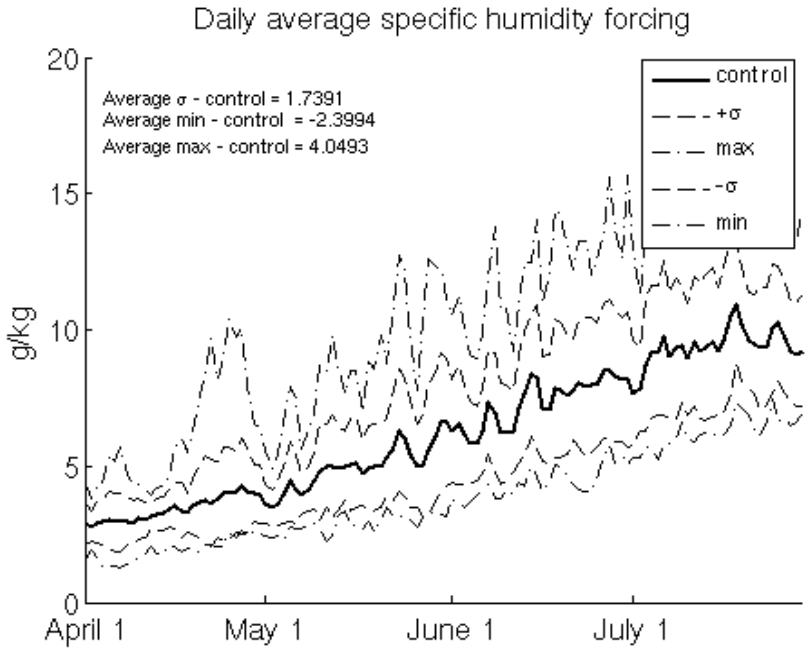

Figure 3d. Forcing used in the sensitivity simulations, specific humidity.
Control forcing is the mean value of the parameter determined by analysis of 1979-1997 NARR covering Lake Superior. Three hour data was interpolated to the 100 x 100 km model domains used in the simulations. Perturbation forcing is 1 sigma above or below the mean value for the selected parameter, or the maximum or minimum value.

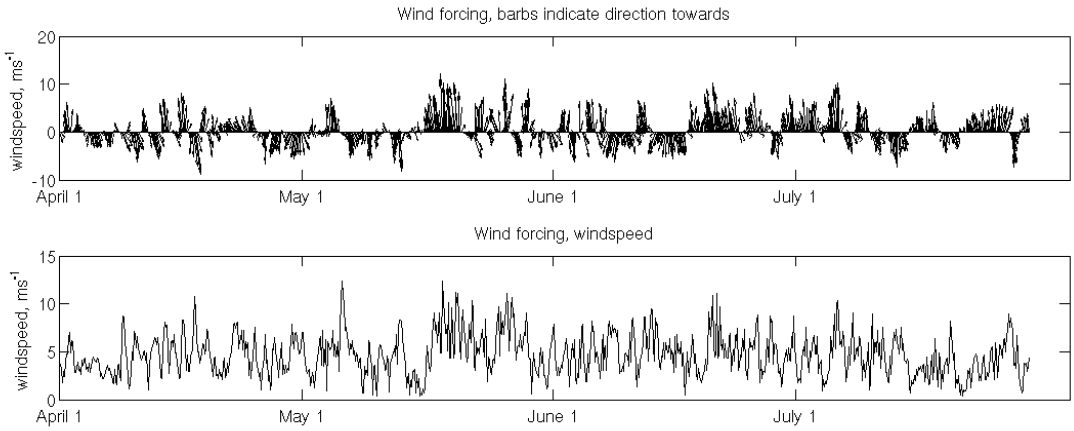

Figure 4. Wind forcing used in the sensitivity simulations. Shown are the wind vectors (upper) and windspeed (lower) at the center of the model domains. Barbs in the upper plot indicate the direction wind is blowing towards. Three hour wind data from 1989 NARR covering Lake Superior was interpolated to model domains.

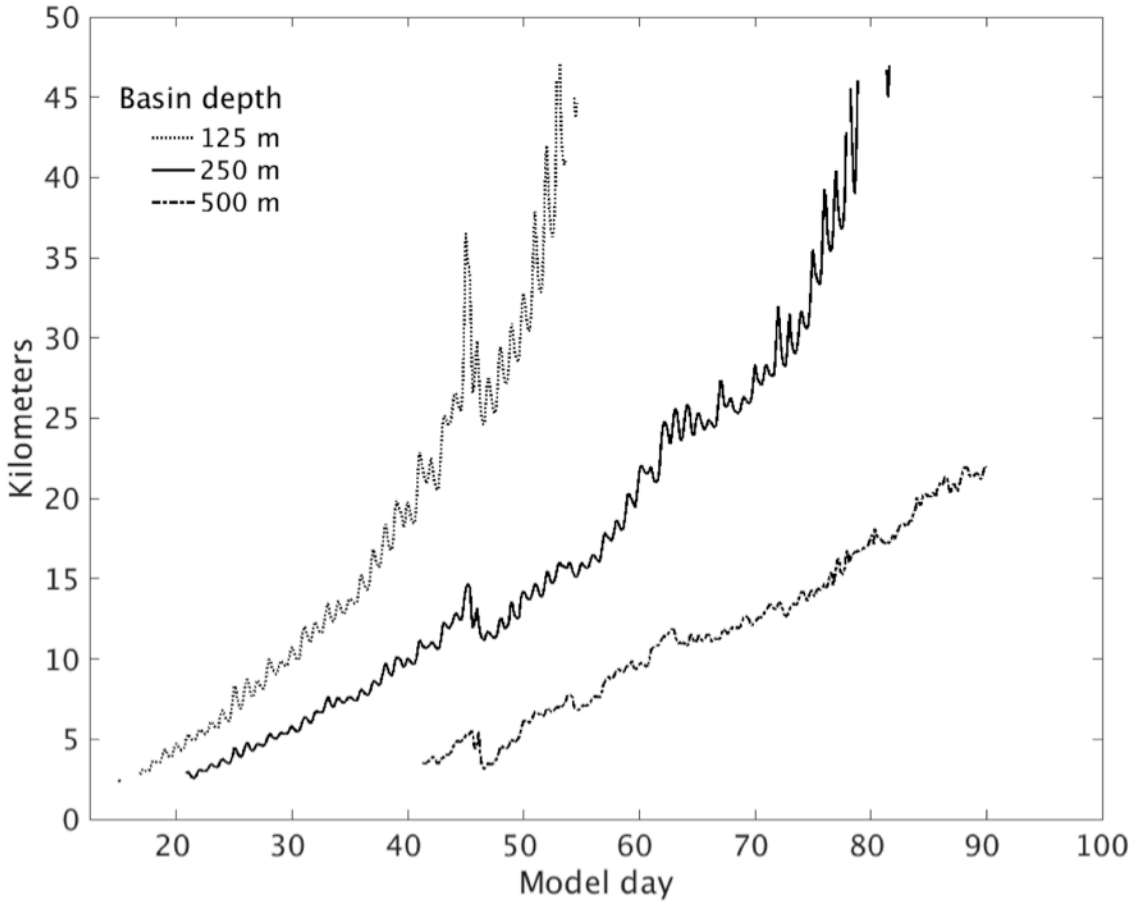

Figure 5. Thermal bar offshore migration in each basin under the control forcing. Computed by averaging the distance from the east, west, north and south boundaries to the 4 °C isotherm (thermal bar) at the surface. The distance after the thermal bar is 3 km offshore is shown. The rate the thermal bar retreats away from shore increases after the thermal bar is more than 15 km offshore where bottom slope is shallow (dotted line) and intermediate (solid line).

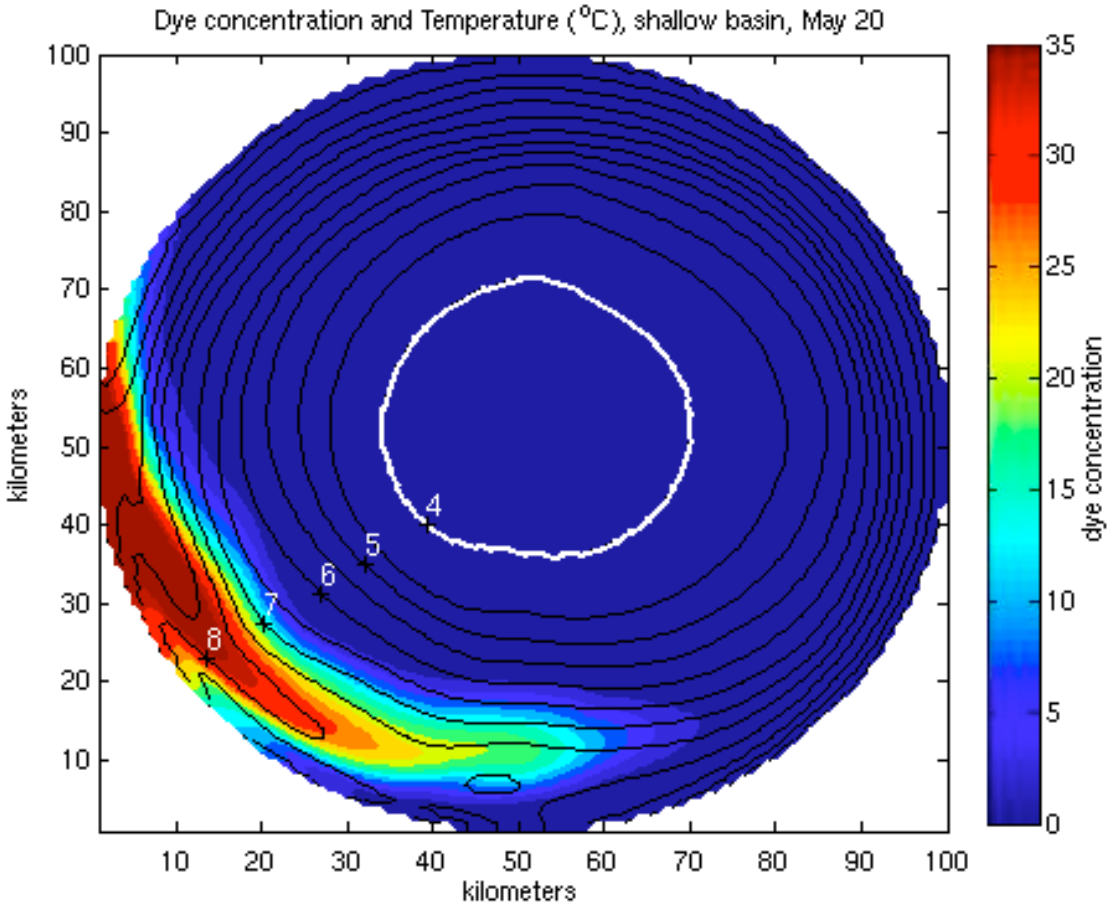

Figure 6a. Shallow basin, map view temperature and passive tracer concentration on model day 50. Values plotted in the map view are the average of the top 1 meter of the water column. Dye was added once at the beginning of the model run to a 20 x 10 grid cell area along the western shore. Initial dye concentration was 100 on the scale provided and was uniform throughout the water column.

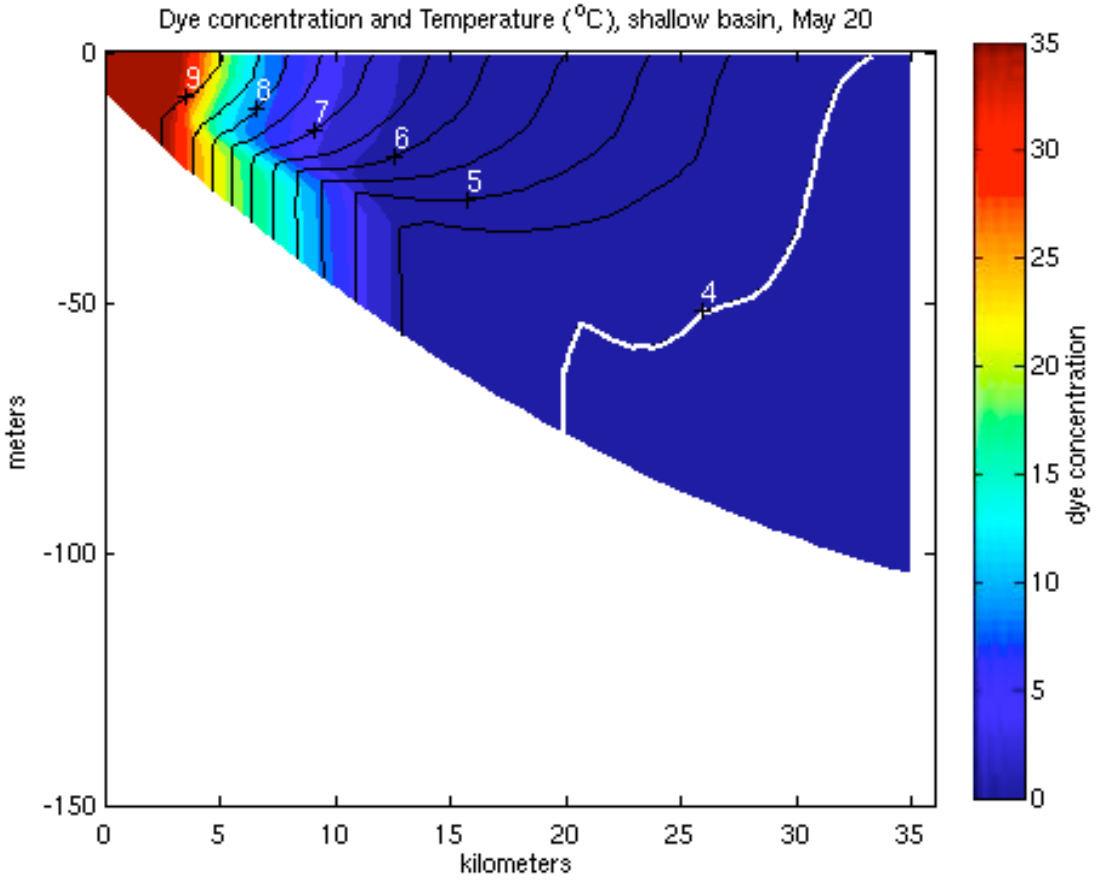

Figure 6b. Shallow basin, cross section of temperature and passive tracer concentration on model day 50. Cross section view is from the midpoint of the western (left hand side) boundary. Dye was added once at the beginning of the model run to a 20 x 10 grid cell area along the western shore. Initial dye concentration was 100 on the scale provided and was uniform throughout the water column.

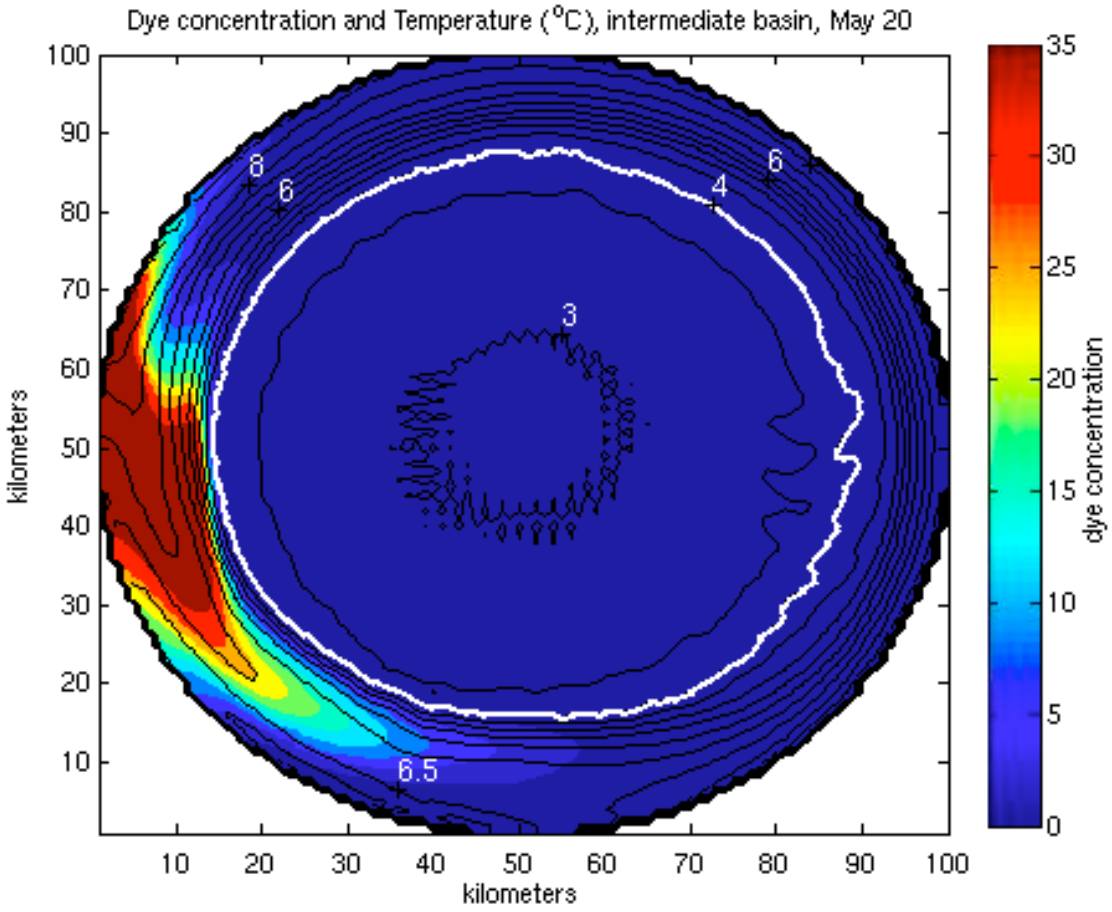

Figure 6c. Intermediate basin, map view temperature and passive tracer concentration on model day 50. Values plotted in the map view are the average of the top 1 meter of the water column. Dye was added once at the beginning of the model run to a 20 x 10 grid cell area along the western shore. Initial dye concentration was 100 on the scale provided and was uniform throughout the water column.

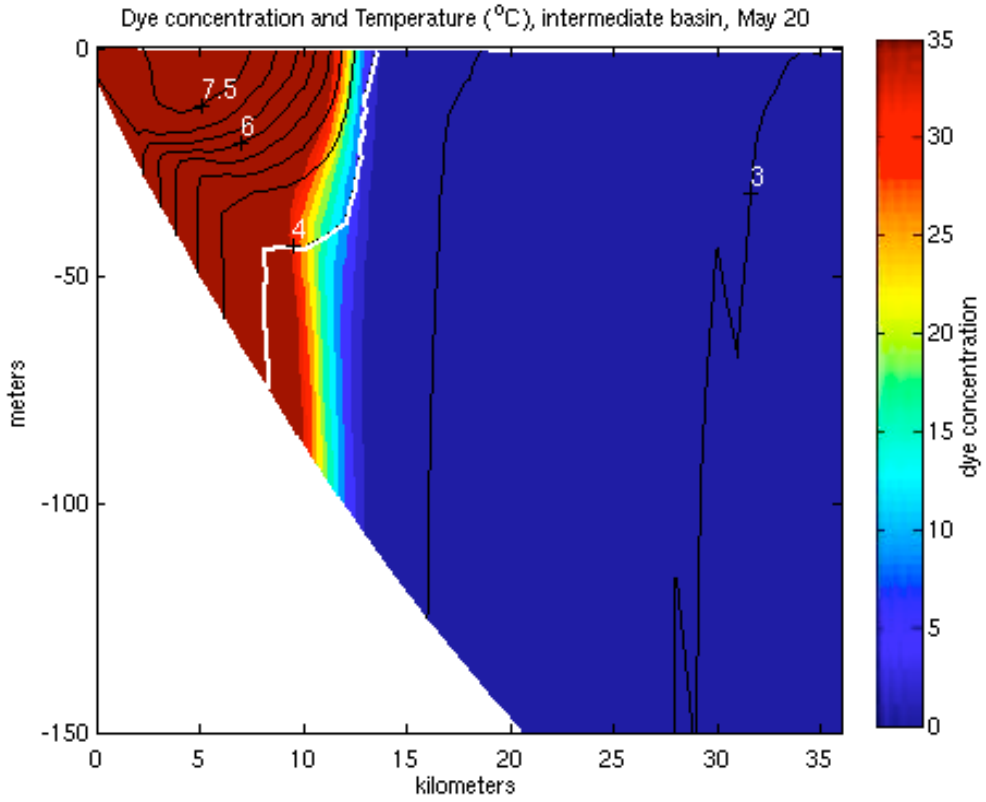

Figure 6d. Intermediate basin, cross section of temperature and passive tracer concentration on model day 50. Cross section view is from the midpoint of the western (left hand side) boundary. Dye was added once at the beginning of the model run to a 20 x 10 grid cell area along the western shore. Initial dye concentration was 100 on the scale provided and was uniform throughout the water column.

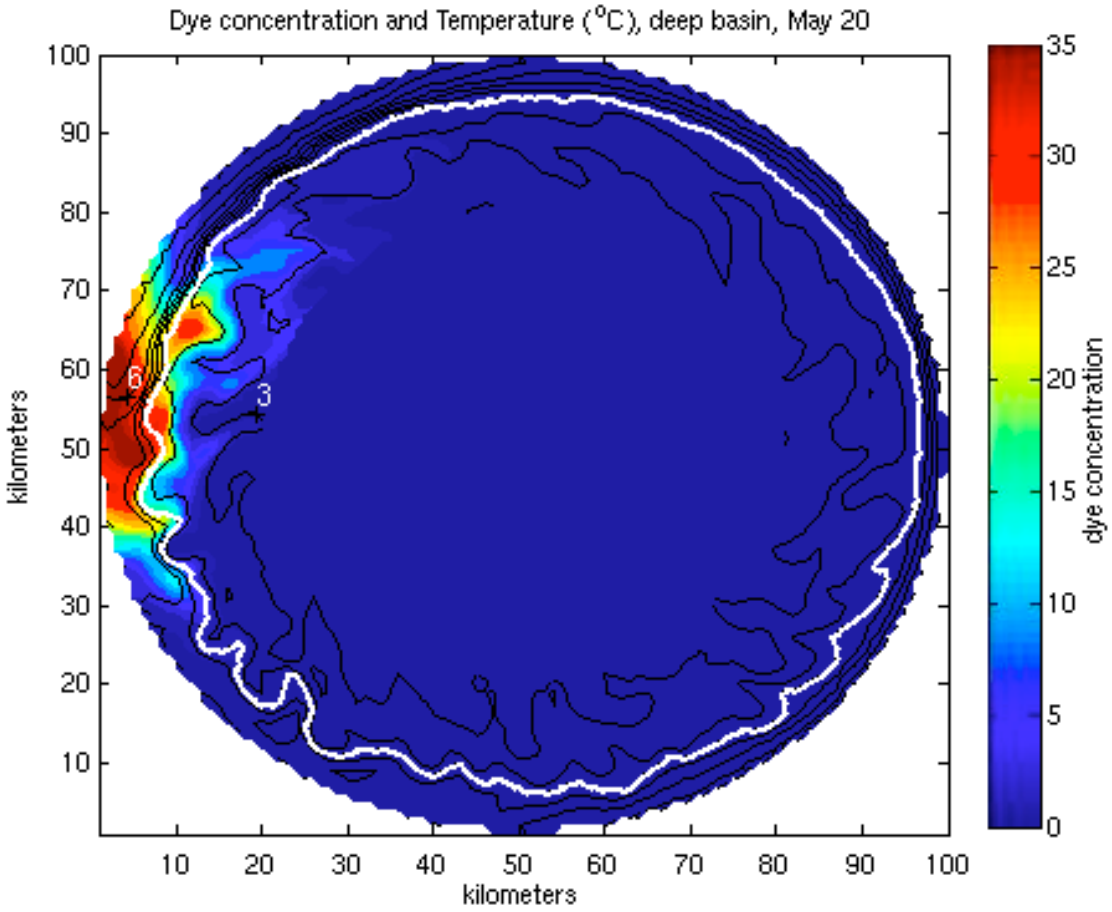

Figure 6e. Deep basin, map view temperature and passive tracer concentration on model day 50. Values plotted in the map view are the average of the top 1 meter of the water column. Dye was added once at the beginning of the model run to a 20 x 10 grid cell area along the western shore. Initial dye concentration was 100 on the scale provided and was uniform throughout the water column.

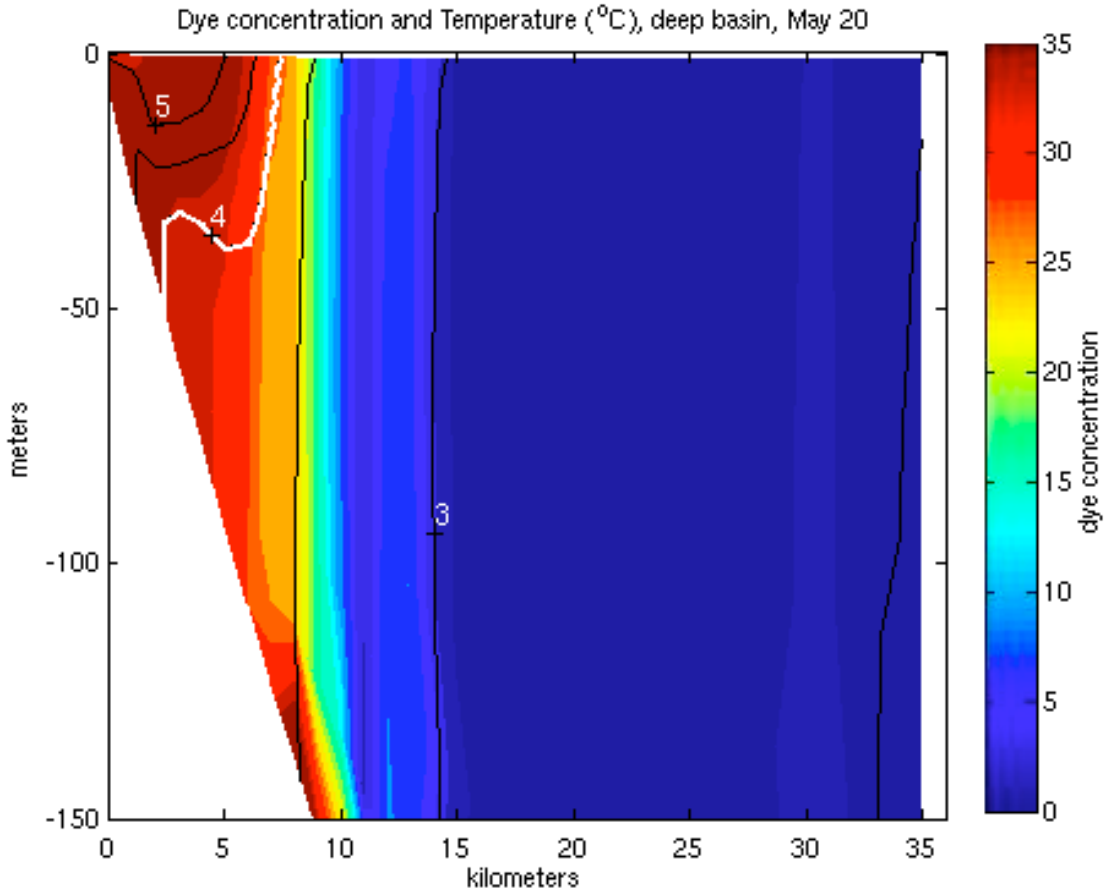

Figure 6f. Deep basin, cross section temperature and passive tracer concentration on model day 50. Cross section view is from the midpoint of the western (left hand side) boundary. Dye was added once at the beginning of the model run to a 20 x 10 grid cell area along the western shore. Initial dye concentration was 100 on the scale provided and was uniform throughout the water column.

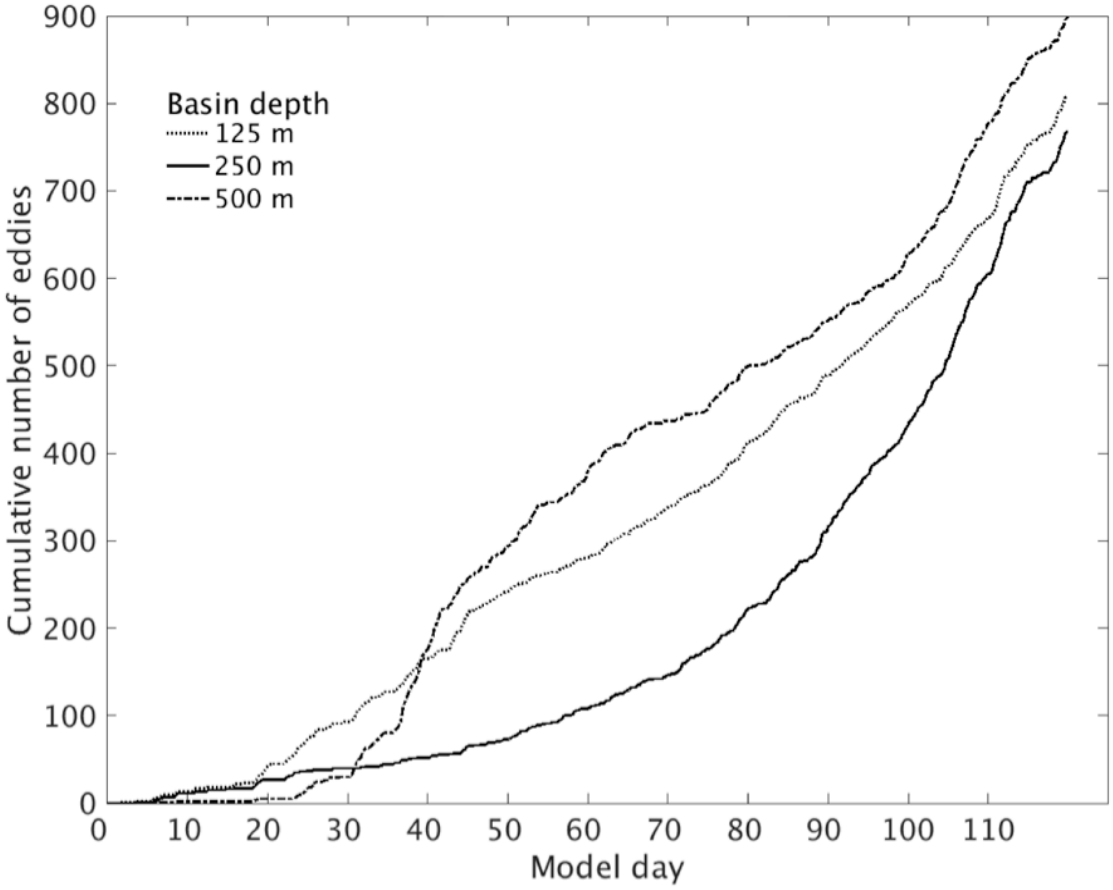

Figure 7. Cumulative number of eddies detected in the surface of each idealized basin under the control forcing.

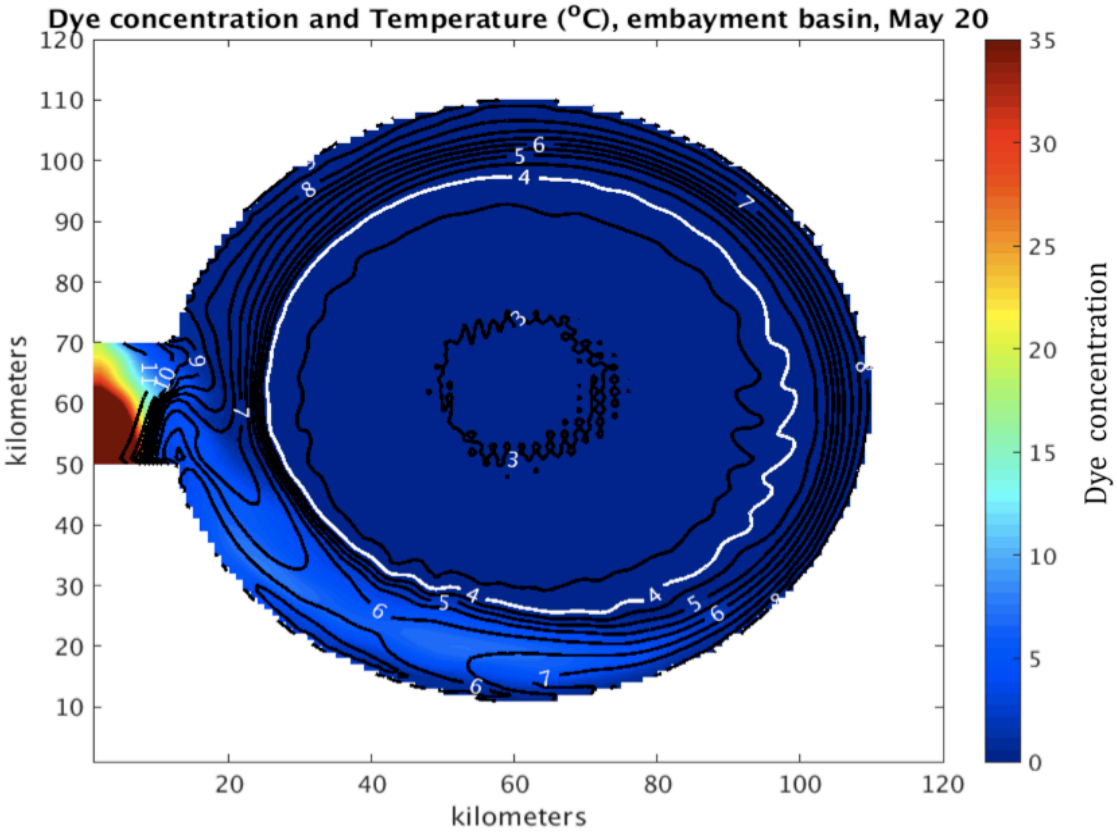

Figure 8a. Embayment basin, map view temperature and passive tracer concentration on model day 50. Values plotted in the map view are the average of the top 1 meter of the water column. Dye was added once at the beginning of the model run to a 20 x 10 grid cell area within the embayment along the western shore. Initial dye concentration was 100 on the scale provided and was uniform throughout the water column.

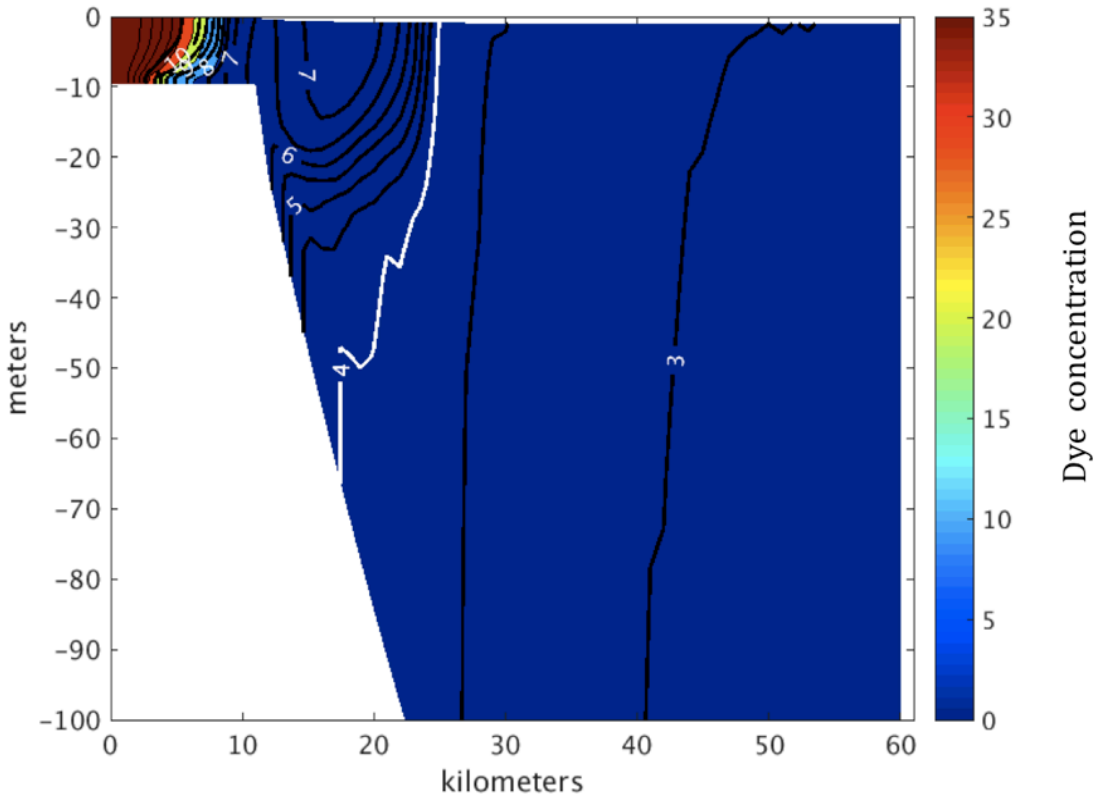

Figure 8b. Embayment basin, cross section temperature and passive tracer concentration on model day 50. Cross section view is from the midpoint of the western (left hand side) boundary. Dye was added once at the beginning of the model run to a 20 x 10 grid cell area within the embayment on the western shore. Initial dye concentration was 100 on the scale provided and was uniform throughout the water column.

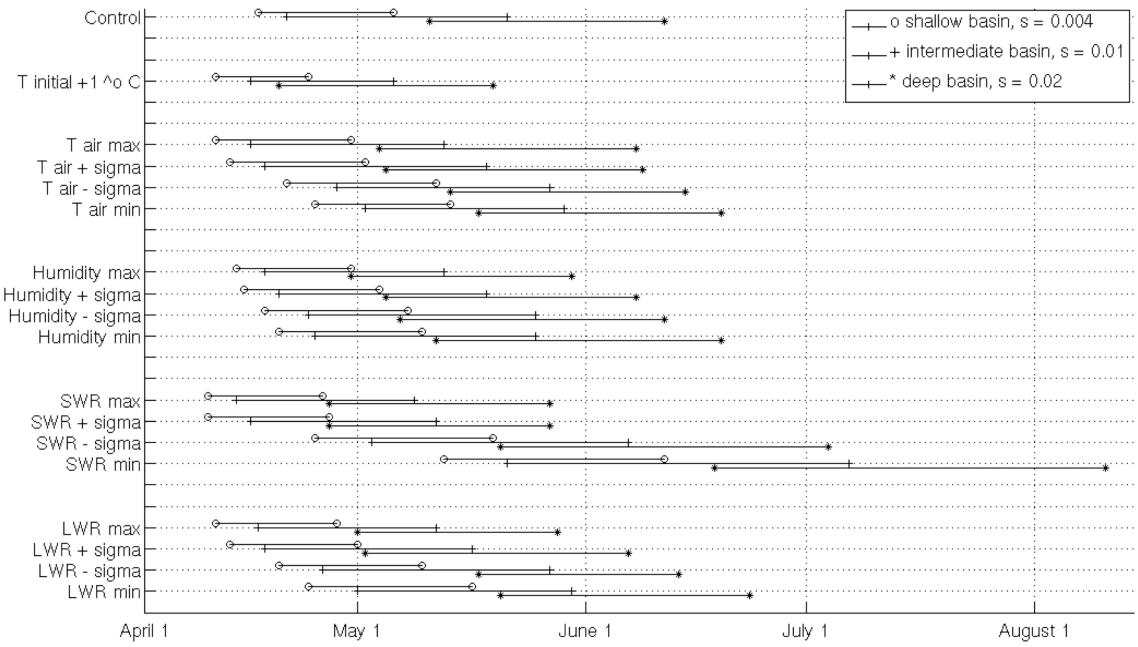

Figure 9. Nearshore duration of the thermal bar under alternate forcing scenarios. Duration of the thermal bar between 3 km offshore (left hand side of horizontal line) and 15 km offshore (right hand side) for each forcing scenario.

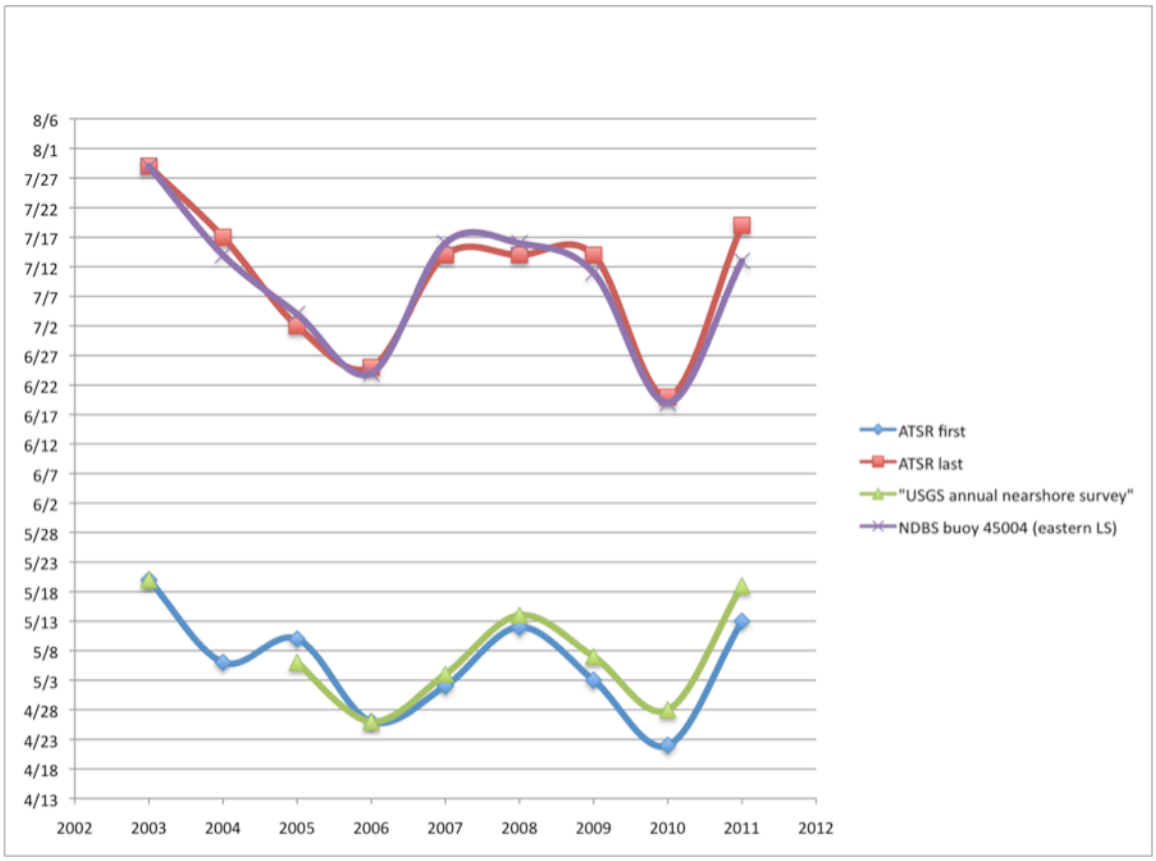

Figure 10. First and last appearance of 4 °C isotherm, Lake Superior, 2003-2011. In situ observations of surface temperature from USGS annual nearshore survey (Mark Vinson, personal communication) and NDBC buoy 45004. Satellite observations of surface temperature from ATSR data product (Michelle Gierach, personal communication).

Chapter 4: Nearshore-offshore exchange in Lake Superior, a numerical model study

---

Introduction

Circulation within the Great Lakes is dominated by shore parallel flow that tends to segregate nearshore zones from offshore (Beletsky et al., 1999; Rao and Schwab, 2007). As a result, concentrations of nutrients and pollutants are higher in nearshore areas, and reflect the character of the surrounding landscape (Yurista et al., 2011). Exchange processes between nearshore and offshore zones dilute the elevated concentrations and control nearshore water quality parameters, including heat content, that are vital to lake ecosystem functioning. The objective of this study is to investigate the spatial and temporal variability of transport between nearshore and offshore areas of Lake Superior, the world's largest lake by surface area, using a three dimensional numerical model of lake hydrodynamics and virtual tracers.

Lake Superior is the headwaters of the Laurentian Great Lakes, the world's largest freshwater ecosystem. With a maximum depth of 406 m and a mean depth of 147 m, it is the deepest of the lakes, and contains approximately 10 percent of the world's surface freshwater, roughly the same amount as the other four combined. Compared to the lower lakes, there is little development in its watershed, and as a result it is relatively pristine. Its catchment is made up of thin and unproductive soils derived from the surrounding igneous and metamorphic bedrock, and covers a small area relative to the lake's surface area (Schertzer and Rao, 2009). As a result nutrient (i.e., phosphate) levels are low, and it

is classified as oligotrophic. Biomass is dominated by microbes (Cotner et al., 2004). Its one outlet has a modest flow, and the residence time is the longest of the Great Lakes at 191 years (Quinn, 1992).

The lake's mean coastal circulation is primarily cyclonic (counterclockwise) year-round, driven by wind stress curl in the winter and combined wind stress and thermally driven coastal currents in summer (Bennington et al., 2010). Associated with the coastal circulation are nearshore thermal fronts, meanders and eddies, commonly observed in satellite images of the lake surface temperature throughout the summer (Ullman et al., 1998; Budd, 2004).

In a previous study (McKinney et al., 2012), we identified small eddies in the nearshore using a combination of satellite-based Synthetic Aperture Radar (SAR) and thermal imagery. Eddies were more frequently observed in images of the lake surface in late summer, however detection of eddies in SAR images is limited to low wind periods and also depends on the presence of surfactants, concentrations of which are expected to be generally low in the oligotrophic and unpolluted surface waters of Lake Superior. In addition, the set of SAR images did not include repeat passes that would have provided time series information regarding the lifetime and fate of the eddies. One of the goals for the modeling study presented here is to learn more about the generation and fate of eddies in the nearshore areas of the lake, and their role in cross shore exchange.

We focus on exchange between nearshore areas defined as those where water depth is less than 100 m and deeper areas of the lake (Figure 1). The 100 m isobath roughly corresponds to the outer extent of the high velocity coastal circulation in

previous model studies (e.g. White et al., 2012). Surveys of fish (Gorman et al., 2011) and benthic zooplankton (Auer et al., 2013) as well as stable isotope analyses (Sierzsen et al., 2014) suggest the 100 meter depth contour also divides the lake's food web into nearshore and offshore components.

The paper is organized as follows. The following section briefly describes the modeling system including the passive tracers. This is followed by results from the two series of simulations, a discussion and summary.

Model description

Lake Superior's thermal structure and circulation during 2003-2012 was simulated using the Regional Ocean Modeling System (ROMS) (Shchepetkin and McWilliams, 2005). ROMS is a free surface, hydrostatic primitive equations ocean model utilizing a terrain-following vertical coordinate system that is widely used by an ocean modeling community in applications covering a wide range of scales, including Lake Superior (White et al., 2012; White and Matsumoto, 2012; Matsumoto et al., 2015). For this study, we used the model of Lake Superior by White et al. (2012), including fresh water equation of state, and Mellor-Yamada 2.5 vertical turbulence closure scheme. The model of Matsumoto et al. (2015), also derived from White et al. (2012), contains some modifications to the radiation code as it relates to ice, but those modifications are not included here. The biological module used in the previous studies was omitted.

The model utilized a two km orthogonal grid and 16 terrain following vertical layers spaced unevenly throughout the water column so that vertical resolution was

higher near the surface. The thickness of the surface layer averaged 1.4 m whereas the thickness of the bottom layer averaged 22 m. Meteorological forcing was obtained from the North American Regional Reanalysis (NARR) (Mesinger, 2006), which is widely available. The model calculated fluxes of latent and sensible heat as well as momentum internally from the NARR using the TOGA-COADES bulk flux algorithm (Fairall et al., 1996). Radiative fluxes were input directly from the NARR, and shortwave radiation was attenuated in the water column using the Jerlov water type 1 parameter, corresponding to oligotrophic conditions (Paulson and Simpson, 1977). The ROMS uses a split-explicit time stepping scheme for computational efficiency. The baroclinic equations timestep was set to five minutes and the barotropic equations were solved 60 times between each baroclinic timestep. Daily averages were calculated internally in ROMS and saved for analysis.

Eddies were identified and characterized in the surface layer of the model output using an automated eddy detection algorithm originally developed for use with ROMS and described in (Nencioli et al., 2010). The algorithm identifies eddies based on the geometry of the simulated currents a specified number of grid cells from each grid point, and eddy centers are identified where current speed is lowest within a specified area within closed streamlines. The distance parameter ('a') was set to 3 grid cells, and the eddy center parameter ('b') was set to 2 grid cells.

Two series of model simulations were conducted. Each series of simulations used a different passive tracer configuration to examine nearshore-offshore exchange. The first series covers the entire period from 2003-2012, and uses three virtual tracers. The first

tracer is an aging tracer and is referred to as '*Nearshore Age*', (hereafter *Age)*. *Age* increases in value with each timestep where water depth is less than 100 m, the nearshore zone. In deeper areas, *Age* is set to a constant value of zero. Mixing between the nearshore zone and deeper areas dilutes the concentration of *Age*, which is always less than or equal to the elapsed time of the model run. For example, it equals the elapsed time if no dilution has occurred. Although the overall value of *Age* cannot be greater than the total elapsed time of the simulation, mixing between a cell with low *Age* and a neighboring cell with high *Age* can temporarily increase *Age* in the cell where *Age* was initially lower by more than the model's timestep.

The two additional tracers used in the first series of simulations were passive tracers. The initial concentration of a tracer referred to as 'offshore tracer' was set to zero in nearshore areas and one in offshore areas. Initial concentration of a complementary tracer referred to as 'nearshore tracer' was set to zero in offshore areas and one in nearshore areas. As the simulation progressed, exchange between nearshore and offshore areas increased the concentration of each tracer in the part of the lake where it was initially zero. When the entire lake reaches a uniform concentration of one, the tracers offer no new information. The tracer concentrations were reset to their initial values on January 1 of each year.

The model was initialized by spinning up from rest and uniform temperature of 4 °C and running for three years using NARR forcing for years 2000, 2001 and 2002. The model was then run for 10 additional years using NARR forcing for 2003-2012.

The second series of simulations consisted of two model runs, each covering a 90 day period from the summer of 2004. The first model run covered the first 90 days of the summer stratification period, and the second covered the second 90 days. Virtual passive tracers were placed in selected nearshore areas at the start of each model run (Figure 1). Exchange between nearshore and offshore areas in early summer was compared to exchange in late summer by evaluating the differences in the distribution of the tracers in each model run. In general, Lake Superior's temperature structure in early summer is characterized by the presence of the thermal bar, a shore parallel temperature front at freshwater's temperature of maximum density (T_{md}), roughly 4 °C, that inhibits nearshore to offshore exchange (Ullman et al., 1998; Rao and Schwab, 2007). The year 2004 was selected for the second series of simulations because the first series of simulations (2003-2012) showed a well formed thermal bar in the model output for that year.

The tracer was initially released at nine 200 km^2 areas around the perimeter of the model lake. At each location, the initial concentration of the tracer was uniformly set to unity throughout the water column. The first 90 day simulation began with April 1, and was initialized from the model state on that date in the first series of simulations. The dyes were reset to their initial concentrations for the second 90 day simulation, which began with July 1.

Results

Figure 2 shows the climatology of model mean summer (June, July, August) surface temperature and surface currents over the entire 2003-2012 simulation period.

The model reproduced the typical pattern of summer lake surface temperatures seen in AVHRR images (e.g. Budd, 2004) and the cyclonic (counterclockwise) coastal circulation (Bennington et al., 2010). In addition, the model reproduced cold temperatures along the northwest shore, which are due to upwelling that typically occurs there due to prevailing southwesterly winds.

Figure 3 shows the 10 year climatology of *Age* (left axis) and temperature (right axis) in the entire nearshore zone for the surface 10 m and bottom sigma layer. The concentration of *Age* is reported in days for the nearshore zone only (< 100 m water depth). In the absence of mixing, *Age* would increase at the rate indicated by the one-to-one aging line (dash-dotted line).

Between mid-November and May, *Age* (Figure 3, left axis) values were similar in surface and bottom layers and temperatures (right axis) were nearly isothermal, an indication of vertical mixing. A short period of winter stratification occurred during February and March, when surface temperatures dropped below bottom temperatures. *Age* gradually increased throughout the winter, but the rate at which *Age* increased remained below the slope of the hypothetical 'no-exchange' one-to-one aging line (dash-dotted line), indicating that exchange between nearshore and offshore zones weakened during the winter, but did not stop completely. In the surface layer (solid line), *Age* reached its annual maximum in early June, just after the start of summer stratification.

The summer seasonal density stratification occurs when surface temperatures warm above T_{md} (4 °C, horizontal line). The temperature of the bottom layer rose above T_{md} as well (dashed line), but increased more slowly and remained colder than in the

surface. This indicates that on average, the depth of the summer thermocline was deeper than depth of the bottom layer in the nearshore zone since in general, the temperature below the thermocline in dimictic lakes is T_{md}. While *Age* reached its maximum in the surface in June, it continued to increase in the bottom until early July. As a result, the maximum value of *Age* was higher in the bottom than in the surface.

The period during which *Age* declined in the surface is indicated in Figures 3-6 by the shaded vertical bar. A period of sharp decline occurred in the surface beginning in June, coinciding with the period of strengthening seasonal stratification. The seasonal density stratification is indicated in Figure 3 by the divergence of surface and bottom temperatures between June through August. Surface *Age* reached its annual minimum in mid September when the difference between surface and bottom temperatures was at its maximum. The decline in bottom *Age* reaches a similar constant value in early November.

Vertical mixing occurred between surface and bottom layers in late August. The mixing is indicated by a simultaneous decrease in surface temperatures and increase in bottom temperatures (Figure 3). The mixing also increased the rate at which bottom layer *Age* decreased, since the surface water being mixed downward had lower *Age*.

Figure 4 shows the nearshore tracer concentration in the offshore area of the model. The tracer concentration is reset to zero on January 1 of each year. The plot is consistent with the result of the *Age* tracer shown in Figure 3 in that nearshore tracer concentration stabilized near a baseline value in March and then increased sharply in the surface and more slowly in the bottom during the period of rapid *Age* decline in the

surface (shaded vertical bar). Late summer vertical mixing was also evident as nearshore tracer concentration declined in the surface in September while increasing in the bottom layer. The concentration did not reach 1 by the end of the year, indicating nearshore tracer did not spread completely throughout the offshore areas of the model. This is consistent with the modeling work of Lam (1978), who found the mixing time of the lake was approximately three years.

Figure 5 shows the climatology of nearshore surface and bottom current speeds (left axis) and windspeed (right axis). Surface and bottom current speeds diverged between May and September, corresponding to the period of thermal stratification and the period of rapid exchange between nearshore and offshore areas when surface *Age* declined from its annual maximum (shaded vertical bar).

The number of eddies detected in the surface layer (Figure 6) reflected both the stratification state of the nearshore water column as well as wind forcing. A slight increase in eddy numbers occurred in mid-April, corresponding to an increase in windspeed (Figure 5). Surface and bottom temperatures during this time were isothermal (Figure 3). Eddy numbers increased dramatically during midsummer when stratification was strong and exchange between nearshore and offshore areas was vigorous in the surface layer (shaded vertical bar). Windspeeds during this time were low (Figure 5). The number of eddies decreased slightly in September corresponding to the period of increased vertical mixing discussed above, and then increased to its annual maximum in mid November, when windspeeds increased and stratification was again weak.

Lake Superior has a complex coastline and the width of the zone that extends from shore to the 100 meter isobath varies from place to place reflecting differences in bottom slope. The highest bottom slopes and narrowest shelf areas are found along the Minnesota shore and the northern tip of the Keweenaw Peninsula (KP). The broadest shelf areas are found along the southern and eastern shores. In addition, midlake reefs in the eastern and northern basins also include areas where water depth is less than 100 m. In order to compare how *Age* varies in each of these areas, the nearshore area was divided into sectors (Figure 7a, Table 1).

Figure 7b-h shows the climatology of model temperature and *Age* for each of the nearshore sectors. In the sectors where bottom slope is moderate (Table 1; MI, CE, WI), *Age* increased and decreased according to the seasonal cycle of stratification described above for the entire lake. In sectors where bottom slope is steep and shelf width narrow (Table 1; MN, KW), *Age* was low year-round, indicating exchange between nearshore and offshore zones continued throughout the winter period. The high values of *Age* in the eastern Canada sector (CE) were due to the inclusion in that sector of the isolated large embayment in the southeast (Whitefish Bay), which in general had the highest value of *Age* of any area in the lake.

Mean nearshore surface temperature and *Age* concentration is shown for the entire 10 year simulation in Figure 8. Trends in annual maximum temperature and *Age* suggest an inverse relationship in which higher *Age* values are correlated with colder summers. A linear regression was conducted to find significant (p value $< .05$) correlations between *Age* annual minimum and maximum values and lake state variables including

stratification date, the length of the mixing period, surface temperature and current speed (Table 2).

Nearshore age maximum value and increase were both significantly correlated with winter (January, February, March) windspeed and current speed. Neither was correlated with the length of the winter period (January 1 until the date of summer stratification), the mean winter surface temperature, or the number of eddies detected in winter (Table 2a).

The minimum value of nearshore age in a given year was significantly correlated with summer (June, July, August) surface temperature and the number of eddies detected lakewide, and not correlated to the date of stratification, or summer windspeed (Table 2b). The decrease in age tracer was significantly correlated with summer current speed (Table 2b). The difference between age tracer minimum and decrease is that once the minimum is reached, no additional exchange can occur.

The correlation analysis was completed for each nearshore sector (Table 3). Higher maximum nearshore age values were significantly correlated to higher winter current speeds in sectors CE and MI and WI, where bottom slope is moderate (Table 3a). And in the same sectors, lower nearshore age values were significantly correlated to higher summer current speeds and surface temperatures (Table 3b).

Figure 9(a-b) compares surface nearshore *Age* and eddy locations on June 1, the date of maximum surface *Age* in the climatology (Figure 3), when relatively few eddies were detected (Figure 6) and September 1, the date of climatological minimum age, when the number of eddies was near its annual maximum. On June 1 (Figure 9a), age exceeded

100 days over most of the southern shelf and eddies were concentrated in the eastern basin. On September 1 (Figure 9b), maximum age values were less than 100 days, and less than 50 over the southern shelf. Eddies were widespread and more numerous than on June 1, consistent with the eddy climatology (Figure 6). Multiple eddies were located near the 100 meter contour (white dotted line), including along the western and northwestern coasts of the KP, consistent with the SAR-based study (McKinney et al., 2012).

The second series of simulations consisted of two 90 day simulations covering the summer of 2004. Lake conditions during the first 90 day simulation (Figure 10, light shading) included warming and stratification of the nearshore, an increase in nearshore *Age* to its annual maximum, and the beginning of the mid-summer decline in nearshore *Age*. Over the course of the second 90 day simulation (Figure 10, dark shading), seasonal stratification reached its peak, and surface nearshore *Age* reached its annual minimum.

Passive dye tracers were released at the beginning of each 90 day simulation from nine locations around the lake perimeter, and their dispersal evaluated by their distribution in six offshore sectors (Figure 1). At the end of the first 30 day period (Figure 11a), dye tracer remained close to the nine starting locations, and dispersal to the offshore sectors was near zero (not shown). After 60 days (Figure 11b), tracer 7 had spread offshore into sector W2, located along the western shore of the KP, and tracer 4 had spread offshore into sector E2. Figure 11b also shows the locations where eddies were detected by the eddy detection algorithm, including the central part of the lake, where they appear to be associated with a northward flowing current.

Current vectors in Figure 11c indicate that after 90 days the model had reproduced the counterclockwise coastal circulation that typifies summer circulation in the lake. An exception occurred in the southwest part of the lake where clockwise circulation dispersed tracer 3 offshore where it was entrained in an eddy.

Other eddies in the west occurred along the front defined by the concentration of tracer 1 in sectors W1 and W2, and within a current that traveled between the northern tip of Isle Royale (IR) and the midpoint of western shore of the KP. A second current connected the southern tip of IR with the southwestern shore of KP.

In the eastern basin, eddies occurred along the front defined by the dispersal of dye tracer into sectors E2 and E3 as well as in the midlake reef areas. A number of eddies occurred near the 100 meter contour (white dotted line).

In general, tracers that had been released in the western half of the lake were more widely dispersed into the offshore areas than those in the east. The tracer with the widest dispersal was tracer 1, originally released in Thunder Bay. By the conclusion of the first 90 day period it had spread over 40 percent of the surface area of sector W1 (Figure 11c, bottom panel).

Dye tracers were reset and released from the same locations at the beginning of the second 90 day simulation. After 30 days (Figure 11d), tracer in the eastern basin was concentrated within the coastal current whereas in the western basin, tracer concentration offshore was higher than in the east due to transport by three currents (A, B and C in Figure 11d) that traveled southeast from the northwestern shore and another current (D) that traveled northwest from the midpoint of the KP. As a result of the southeasterly

currents, tracer from the northwest became entrained in the counterclockwise coastal current along southern shore, and spread into the eastern basin (Figure 11e).

After 90 days (Figure 11f), tracer in the eastern basin remained concentrated within the counterclockwise coastal current, with the highest concentrations in the embayments along the east shore. In contrast, nearly the entire offshore area of the western basin was covered with tracer, with the highest concentration occurring in the far southwest corner.

Discussion

The model adequately simulated Lake Superior's mean circulation and thermal structure, including the nearshore to offshore thermal gradient and coastal circulation (Figure 2). There were some shortcomings related to the model configuration, for example, in the first series of simulations, low values of *Age* tracer year-round indicated nearshore areas with steeply dipping bottom slope mix continually with offshore areas (Figure 7f-h). However, the 2 km grid size was as wide as the shelf in some steep areas. A nested grid configuration (Appendix 2) that increases horizontal resolution in steep nearshore areas would improve the understanding of the scales of horizontal exchange in those areas. For example, there could be a very narrow area close to shore where *Age* increases seasonally that the 2 km grid did not resolve.

In areas with moderate bottom slopes, shelf width was wider and *Age* exhibited an annual cycle that reflects a seasonal change in the scales of horizontal mixing. Low rates of exchange occurred during late winter and spring, when lake thermal structure was

isothermal or weakly stratified, and higher rates occurred after the onset of seasonal stratification (Figure 7a-d). The high rates in summer occurred first in the surface layer, and then in the bottom. The time lag resulted in the bottom layer reaching the highest nearshore *Age* values.

Maximum and minimum *Age* values were significantly correlated to current speed in both winter and summer (Table 1). However, wintertime exchange was also significantly correlated with higher windspeed, whereas in summer, higher exchange correlated with higher surface nearshore surface temperatures. The difference reflects the seasonal difference in the relative contributions of wind driven and thermally driven currents in our model of Lake Superior's circulation. Consistent with other model studies and available observations, baroclinic effects play a larger role in summer, when wind speeds are lower (Bennington et al., 2010).

In general, the isothermal period of winter and spring was a time when *Age* increased. However, in some years, including 2007, the annual increase was punctuated by abrupt declines (arrow, Figure 8). Figure 12 presents a closer view of the results covering 2007. A period of high exchange in spring is indicated by two sharp declines in *Age* (arrows, Figure 12a). These coincide with increases in the concentration of nearshore tracer in the offshore areas (Figure 12b), windspeed and current speed (Figure 12c), and the number of eddies (Figure 12d). As a result, the maximum value of nearshore *Age* in 2007 was lower from what it may have been had the two events not occurred.

Springtime wind events similar to these reduce the residence time of nearshore waters with potentially dire consequences for nearshore pelagic species. As an example,

cisco *Coregonus artedi* is a coldwater keystone prey fish species that spawns in the nearshore zone of Lake Superior in late fall. The eggs overwinter in nearshore areas and hatch in late spring (Myers et al., 2015) when temperatures and the availability of the spring plankton bloom (Auer et al., 2010) are favorable for rapid growth.

Although they spawn in great numbers annually, only a few cisco year classes survive to the juvenile stage. Thus, current stocks are sustained by a small number of year-classes, a concern for fishery managers because of the importance of cisco in the lake's food web. Analysis of cisco recruitment in Lake Superior indicates abiotic factors operating over regional scales drive recruitment (Rook et al., 2013). Myers et al., (2015) show cisco recruitment in Lake Superior is correlated to interannual variability in nearshore surface water temperature and windspeed. For example, 2007 was a year in which nearly the entire year class was lost. Peak windspeeds that spring were high. They found years with relatively higher recruitment included 2009, in which windspeeds were lower (Myers et al., 2015). This also the year with the highest value of *Age* in our study (Figure 13).

For a more complete view, Figure 14a-b compares the geographic distribution of the anomaly of the maximum value of *Age* in 2007, a year with poor recruitment success, to the anomaly in 2009, a year with relatively high recruitment success. In 2007, nearly the entire nearshore area has a negative *Age* anomaly, corresponding to more exchange between nearshore and offshore waters that spring. In contrast, the 2009 *Age* anomaly is higher in nearly the entire nearshore area. The high value of *Age* is due to reduced exchange between nearshore and offshore areas that spring. These conditions would

promote larval cisco survival by increasing the length of time they reside in warmer, more productive nearshore areas, a key factor in recruitment.

The second series of simulations compared the dispersal of tracers released in nearshore areas during the thermal bar period (Figures 11a-c) to their dispersal later in summer when the entire lake was stratified (Figures 11d-f). The model reproduced the expansion and strengthening of stratification from nearshore to offshore areas. Dispersal of the tracers by the end of the first 90 day period (Figure 11c) was roughly equivalent to the dispersal after only 30 days of midsummer conditions (Figure 11d). The differences between the two 90 day scenarios indicate rates of exchange vary over the course of the summer according to the strength of stratification and not simply due to the presence or absence of the thermal bar. It should be noted however that the two km resolution of the model grid is too coarse to resolve fine details of the thermal bar, which typically occur over scales of 100 m (Appendix 1). These details could be resolved by refining the model with a nested grid (Appendix 2).

The simulated coastal circulation exhibited an asymmetry in that the currents were stronger in the east than in the west. While this is broadly consistent with other model studies (Bennington et al., 2010, White et al., 2012) additional observations are very much needed to resolve this feature. The asymmetry was evident in the distribution of the nearshore dye tracers. For example, in the eastern basin, the coastal current remained close to shore and transported the tracers originating in the KP region (Figure 1, tracers 7, 8, 9) as well as those originating the eastern basin (Figure 1, tracers 4, 5, 6) far from their origin to the northern coast (Figure 11d-f, histograms). The highest

concentrations occurred within the eastern embayments, associated with stationary eddies that continually formed in the embayments. Tracer advected to the west was concentrated along the northern coast until the current was deflected to the southeast at the north end of Isle Royale (Figure 11d, C). Watson and Wilson (1978) found a similar pattern in the distribution of nearshore zooplankton that hatch in early summer in the embayments of southern and eastern Lake Superior. They hypothesized the plankton spread to the lake's northern perimeter via the coastal circulation, and into the north central lake basin in late summer. This migration may play an important role in the coupling of nearshore and offshore food webs (Sierszen et al., 2014).

The number of eddies increased during the summer (Figure 6) when offshore dispersal of tracer in the western arm increased (Figures 11d-f). A movie (Supplement 2) shows eddies repeatedly formed within the currents that spread dye tracer from nearshore to offshore areas in the western basin (Figure 11d, A-D). Figures 15a and 15b are two frames from the movie showing the location of an anticyclonic eddy that formed at the north end of Isle Royale on Aug 21 and drifted to the southeast over the following 15 days. This generally supports the hypothesis of Ralph (2002) that eddies formed through baroclinic and barotropic processes near shore before moving offshore, becoming trapped within the closed basin.

To better understand how the eddies reproduced in the model might contribute to nearshore-offshore exchange, the average water depth at eddy locations was determined. Figure 16 shows the climatology of average water depth and total daily number of eddies over the 10 year simulation. In winter, eddy numbers are at their annual minimum and

average water depth at eddy locations is roughly 160 m, slightly higher than the 145 m average depth of the model basin. After fluctuating near low values in spring, the number of eddies and the average water depth where they occur both increase, beginning around day 160.

The increase reflects an increase in the number of eddies of the appropriate size to be detected by the algorithm, which depends on both the horizontal scale of the model grid as well as parameters set by the user of the algorithm. The 2 km model is eddy-resolving only for those eddies that have a deformation radius of 8 km. For smaller eddies where the radius is between 2 and 6 km, the model is eddy-permitting. The horizontal scale of baroclinic eddies increases over summer as the baroclinic deformation radius increases, and as more eddies occur at larger scales, they are resolved in the model, and detected by the algorithm. Figure 17 shows the increase in the size of detected eddies that occurs in summer.

The increase in water depth could reflect the movement of coherent eddies from shallower to deeper areas, or an increase in the number of eddies forming in deeper water, which would be expected if they form along thermal fronts that move offshore as stratification expands to deeper areas of the lake. An attempt was made to determine the lifetime of the eddies, which would help determine if the increase in water depth was due to coherent eddies moving into deeper water, however this was inconclusive.

A comparison of eddy temperatures relative to their sense of rotation is presented in Figure 18. The sense of rotation of geostrophic eddies is related to the horizontal density gradient from their edge to their center. For anticyclonic eddies (clockwise in the

northern hemisphere), fluid density is lower at the center relative to the edge, whereas for cyclonic eddies (counterclockwise in the northern hemisphere), fluid density at the eddy center is higher than at the edge. Temperatures at the center of modeled anticyclonic eddies are warmer in summer, and colder in winter, consistent with the non-linear equation of state for freshwater, in which the temperature of maximum density is 4 °C. Cyclonic eddies are the opposite, having colder and thus relatively higher density centers in summer months and warmer, and thus denser, centers than anticyclonic eddies in the winter. The relationship is most clearly seen in the results for 2009, a cold winter (Figure 8). Overall, the number of cyclonic and anticyclonic eddies detected in the model output was similar.

We hypothesized that beginning in spring, eddies moving from warmer nearshore waters to cooler offshore areas could affect the heat content and contribute to the stratification of offshore water. Based on their temperature relationship, we checked results for anticyclonic (warm core) eddies moving from nearshore to offshore in the western basin where the relatively higher nearshore tracer concentrations indicate nearshore to offshore exchange is generally high. Figure 19 shows multiple anticyclonic eddies located near the 100 meter depth contour at multiple locations, including front parallel to the Minnesota shoreline where upwelling is frequently observed in summer.

To assess the contribution to the offshore heat content from the eddies, we calculated the daily change in depth-integrated heat content for each grid cell in the nearshore area in the southwest part of the lake, and subtracted the cumulative surface heat flux at the same cell over the same period. Differences between the two values are

an indication of lateral heat transfer. For example, where the change in heat content exceeds the net surface heat flux, excess heat has moved into the water column. Where the heat content is less, heat has been transported away.

Figure 20a shows integrated heat content of the Wisconsin (WI) nearshore sector (Figure 7a) and accumulated surface heat flux (Figure 20b). High frequency variations in heat content not attributable to surface heating (Figure 20c) occur throughout the summer period, when eddy numbers, depth of occurrence and size are increasing (Figure 6, Figure 16, Figure 17), suggesting eddies move heat laterally between the nearshore sector and its neighboring offshore neighbor at this time of year.

Summary

This study investigated exchange between nearshore and offshore areas of Lake Superior using a hydrostatic, free surface, three dimensional numerical model of the lake and realistic meteorological data covering 2003-2012. The model lake was divided into nearshore and offshore sectors based on the location of the 100 m depth contour and exchange was characterized by changes in virtual tracer concentrations. Nearshore areas were relatively isolated from offshore during the winter period, and nearshore *Age* tracer increased in value in areas where shelf width was greater, and where the coastline included embayments.

Interannual variability of *Age* within the nearshore zone was significantly correlated to winter windspeed. A one m s^{-1} increase in mean windspeed during JFMA correlated with a 16 day decrease in maximum *Age* (Figure 13). Over the 10 year

simulation period, the year with the highest mean *Age* was 2009, when *Age* reached 68 days.

Mixing between nearshore and offshore intensified during the stratified period and was significantly correlated to differences in the date of seasonal stratification and average summer surface temperature, although narrow shelf width areas had high rates of exchange year-round.

The dispersal of passive tracers released in select nearshore locations varied according to the strength of the summer stratification. In the early season, dispersal after 90 days was limited to offshore areas immediately adjacent to the release points. In the late summer, tracers were widely dispersed around the lake. Passive tracer initially released nearshore in the eastern basin was advected alongshore to the northwest within the coastal circulation. In the western basin, tracer released nearshore was broadly distributed offshore by currents and eddies that connect the basin's northern and southern shores. Tracer released in the southwestern end of the lake remained in the west throughout the simulation period, and was not mixed into the offshore waters of the eastern basin.

An eddy detection algorithm applied to the simulated surface currents revealed areas of high eddy activity consistent with previous satellite image observations of eddies in the lake. The temperature and sense of rotation of the eddies detected by the algorithm were consistent with geostrophy. The daily number of eddies detected in the modeled circulation varied according to fluctuations in windspeed, peaking in low wind periods. It

is assumed that wind energy input to the water column in high wind periods is fed to the eddies which are detected in the intervening low wind periods.

In the western lake basin, eddies were more uniformly distributed throughout the offshore area where they were associated with currents that bisect the basin than in the east, where they were concentrated nearshore and within the coastal circulation.

Daily changes in integrated heat content and surface heat flux over a selected nearshore area found high frequency changes in heat content occur during the late summer period when eddy activity peaks, suggesting the eddies transfer heat between nearshore and offshore areas of the lake.

Tables

Nearshore Sector	Average shelf width	Average Bottom Slope
Wisconsin (WI)	17 km	0.0059
Canada East (CE)	15 km	0.0067
Michigan (MI)	14 km	0.0069
Canada North (CN)	10 km	0.010
Keweenaw (KW)	3 km	0.038
Minnesota (MN)	2 km	0.043
Reefs (RF)		not defined (no shore)

Table 1. Shelf widths and bottom slopes for the nearshore sectors.

whole lake	iso length	JFM temp	JFM wind	JFM current	JFM eddies
age tracer maximum	$R^2 = 0.25$	$R^2 = 0.40$ $p = 0.05$	**$R^2 = 0.67$** $p = 0.0039$	**$R^2 = 0.45$** $p = 0.035$	$R^2 = 0.15$
age trace increase	$R^2 = 0.25$	$R^2 = 0.39$	**$R^2 = 0.58$** $p = 0.011$	**$R^2 = 0.40$** $p = 0.049$	$R^2 = 0.22$

Table 2a. Correlation of lake state variables and maximum *Age*.

whole lake	strat date	JJA temp	JJA wind	JJA current	JJA eddies
age tracer minimum	$R^2 = 0.5$	**$R^2 = 0.75$** $p= 0.0012$	$R^2 = 0.32$	$R^2 = 0.008$	**$R^2 = 0.6$** $p = 0.0082$
age tracer decrease	$R^2 = 0.051$	$R^2 = 0.014$	$R^2 = 0.044$	**$R^2 = 0.66$** $p= 0.0044$	$R^2 = 0.08$

Table 2b. Correlation of lake state variables and minimum *Age*.

CE	winter length	JFM temp	JFM windspeed	JFM current
age tracer maximum	$R^2 = 0.21$	$R^2 = 0.26$	$R^2 = 0.39$	**$R^2 = 0.6$ p = 0.008**
age tracer increase	$R^2 = 0.16$	$R^2 = 0.21$	$R^2 = 0.34$	**$R^2 = 0.64$ p = 0.0058**

MI				
age tracer maximum	$R^2 = 0.11$	$R^2 = 0.22$	**$R^2 = 0.85$ p = 0.0001**	**$R^2 = 0.46$ p = 0.031**
age tracer increase	$R^2 = 0.096$	$R^2 = 0.19$	**$R^2 = 0.89$ p = 0.00003**	**$R^2 = 0.54$ p= 0.016**

WI				
age tracer maximum	$R^2 = 0.12$	$R^2 = 0.23$	$R^2 = 0.3$	**$R^2 = 0.49$ p = 0.024**
age tracer increase	$R^2 = 0.1$	$R^2 = 0.2$	$R^2 = 0.23$	**$R^2 = 0.46$ p = 0.031**

CN				
age tracer maximum	**$R^2 = 0.54$ p = 0.015**	**$R^2 = 0.66$ p = 0.0044**	**$R^2 = 0.48$ p = 0.026**	$R^2 = 0.073$
age tracer increase	**$R^2 = 0.68$ p = 0.0033**	**$R^2 = 0.81$ p = 0.0004**	**$R^2 = 0.45$ p = 0.036**	$R^2 = 0.015$

MN				
age tracer maximum	**$R^2 = 0.56$ p = 0.013**	**$R^2 = 0.5$ p = 0.023**	$R^2 = 0.056$	$R^2 = 0.013$
age tracer increase	**$R^2 = 0.45$ p = 0.033**	**$R^2 = 0.47$ p = 0.029**	$R^2 = 0.004$	$R^2 = 0.0006$

RF				
age tracer maximum	$R^2 = 0.18$	$R^2 = 0.35$	$R^2 = 0.26$	$R^2 = 0..25$
age tracer increase	$R^2 = 0.066$	$R^2 = 0.17$	$R^2 = 0.11$	$R^2 = 0.24$

Table 3a. Correlation of lake state variables and maximum *Age*, by sector.

CE	strat date	JJA windspeed	JJA temp	JJA current
age tracer minimum	$R^2 = 0.42$	$R^2 = 0.27$	**$R^2 = 0.82$ p=0.0003**	**$R^2 = 0.89$ p=0.00003**
age tracer decrease	$R^2 = 0.0071$	$R^2 = 0.0007$	$R^2 = 0.0$	$R^2 = 0.026$

MI				
age tracer minimum	$R^2 = 0.23$	$R^2 = 0.27$	$R^2 = 0.41$	$R^2 = 0.21$
age tracer decrease	$R^2 = 0.039$	$R^2 = 0.18$	$R^2 = 0.0011$	$R^2 = 0.0014$

WI				
age tracer minimum	**$R^2 = 0.7$ p = 0.0026**	$R^2 = 0.22$	**$R^2 = 0.85$ p = 0.0001**	**$R^2 = 0.79$ p = 0.0006**
age tracer decrease	$R^2 = 0.023$	$R^2 = 0.0002$	$R^2 = 0.022$	$R^2 = 0.025$

CN				
age tracer minimum	$R^2 = 0.066$	$R^2 = 0.066$	$R^2 = 0.17$	$R^2 = 0.15$
age tracer decrease	$R^2 = 0.1$	$R^2 = 0.1$	**$R^2 = 0.78$ p = 0.0008**	**$R^2 = 0.49$ p=0.023**

MN				
age tracer minimum	$R^2 = 0.008$	$R^2 = 0.15$	$R^2 = 0.075$	$R^2 = 0.0037$
age tracer decrease	**$R^2 = 0.42$ p=0.04**	$R^2 = 0.37$	**$R^2 = 0.49$ p = 0.025**	$R^2 = 0.18$

RF				
age tracer minimum	$R^2 = 0.16$	$R^2 = 0.37$	**$R^2 = 0.56$ p=0.013**	**$R^2 = 0.77$ p=0.0008**
age tracer decrease	$R^2 = 0.16$	$R^2 = 0.086$	$R^2 = 0.0067$	**$R^2 = 0.075$**

Table 3b. Correlation of lake state variables and minimum *Age*, by sector.

Figures

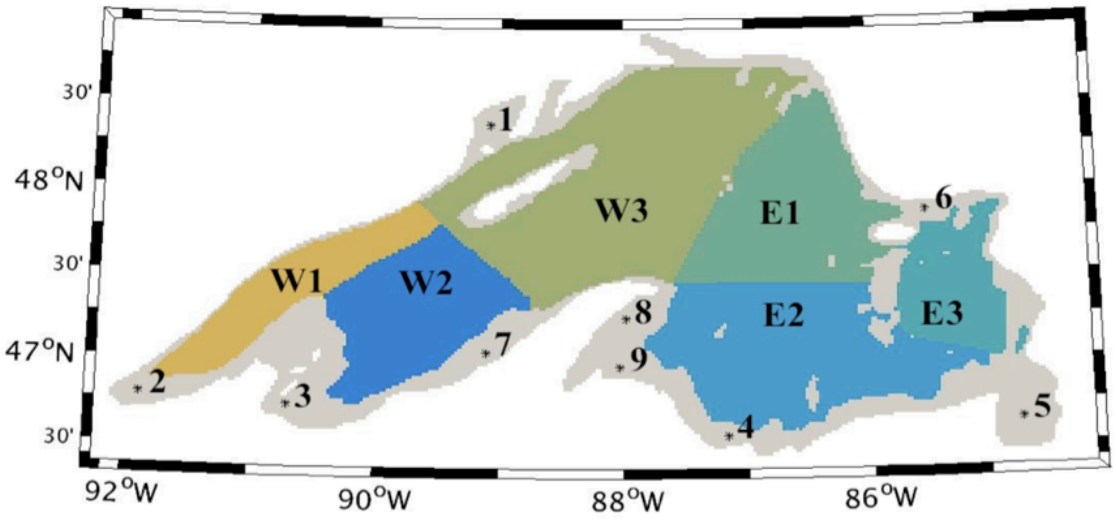

Figure 1. Nearshore and offshore zones of the model domain. Numbered points are located within the nearshore zone and indicate the starting locations for passive dye tracers used in the second series of simulations. The offshore zone is divided into western and eastern sectors identified by letter-number combinations.

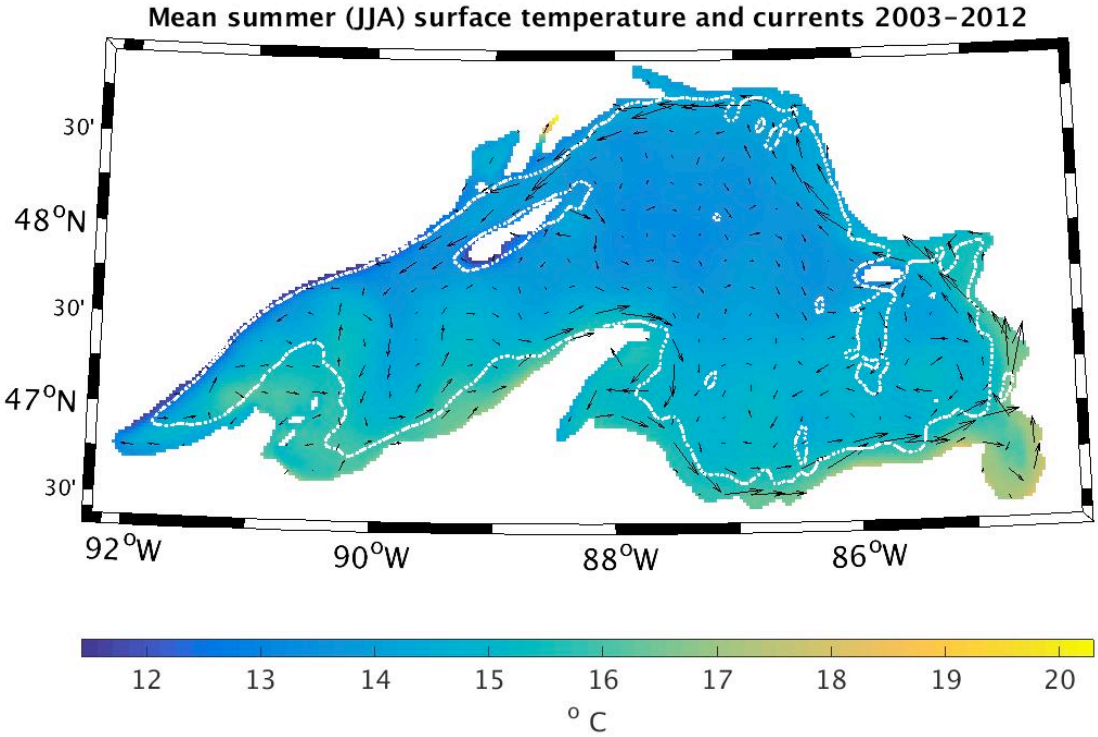

Figure 2. Simulated summer surface temperature and current direction 2003 - 2012. The mean of June, July and August is shown. White line indicates the 100 m depth contour.

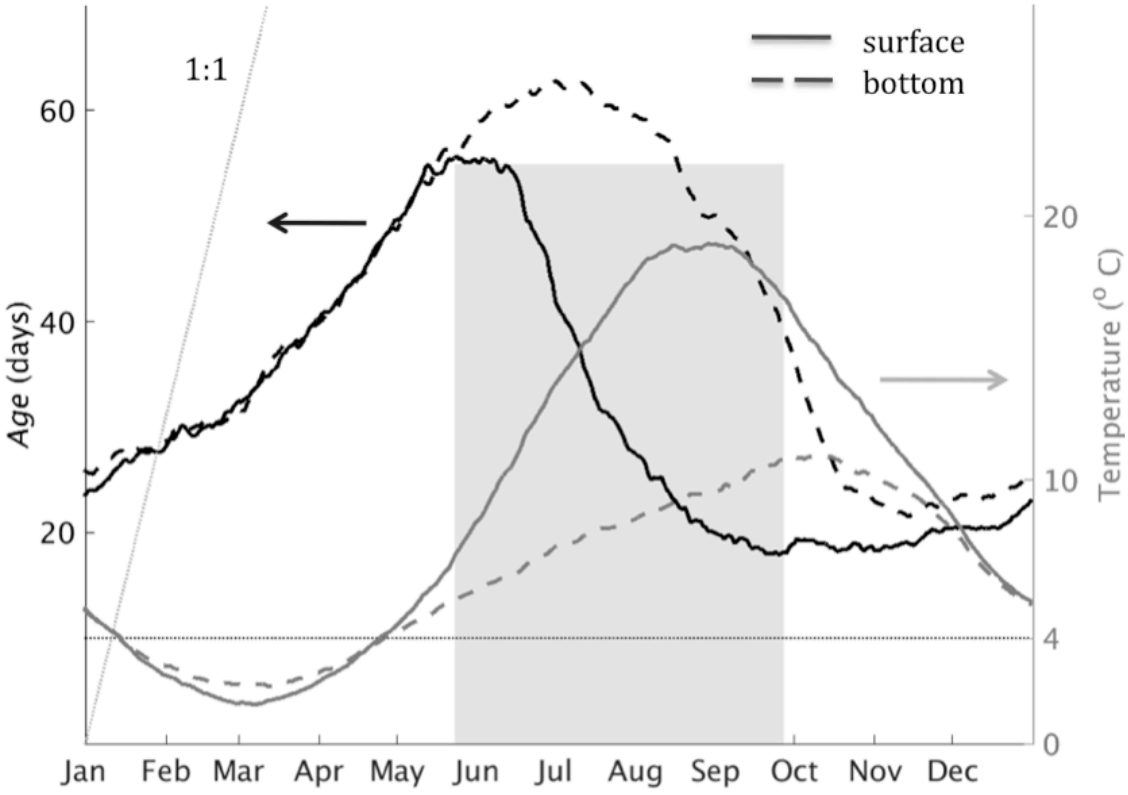

Figure 3. Climatology, mean *Age* tracer and temperature. *Age* values on left axis, temperature values on right axis. The mean calculated over the entire nearshore area of the model domain. The horizontal line indicates 4 °C, freshwater's temperature of maximum density (T_{md}). The 1:1 slope of the dash-dotted line indicates the rate of aging with no mixing between nearshore and offshore areas. Shading indicates period of maximum nearshore-offshore exchange in the surface.

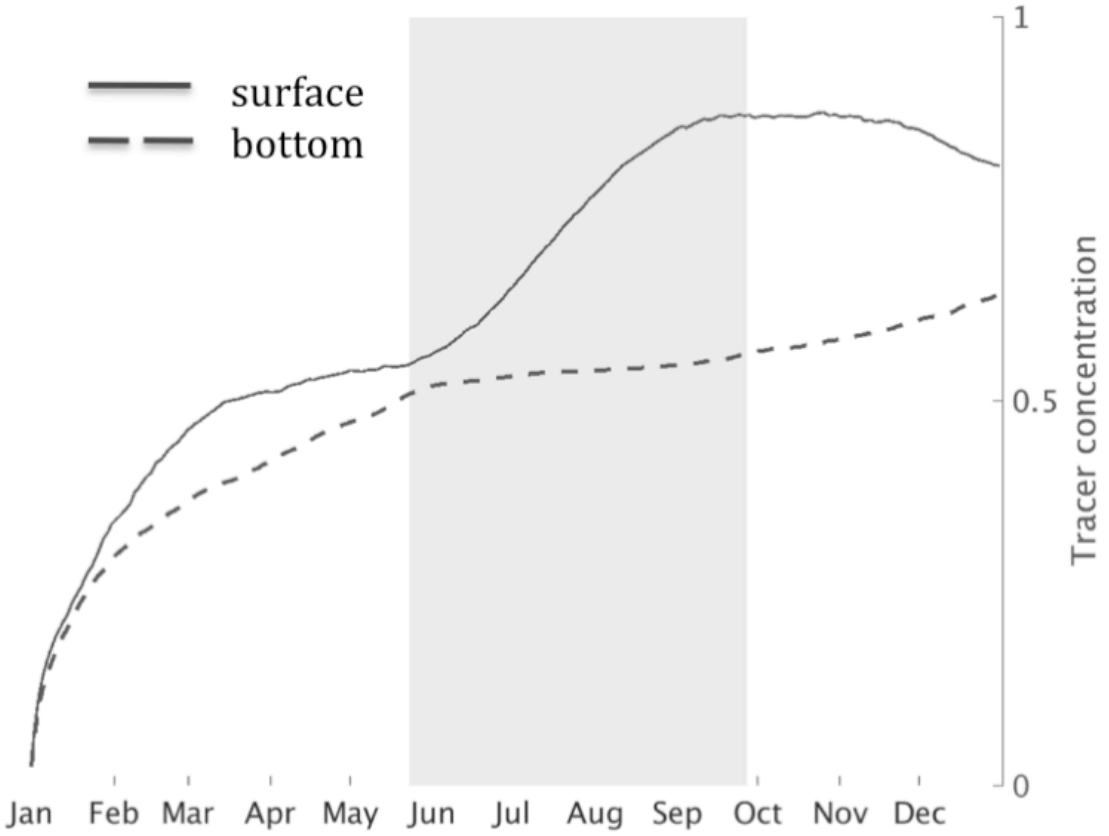

Figure 4. Climatology, nearshore tracer concentration in the offshore. The mean was calculated over the entire nearshore zone. Shading indicates period of maximum nearshore-offshore exchange in the surface.

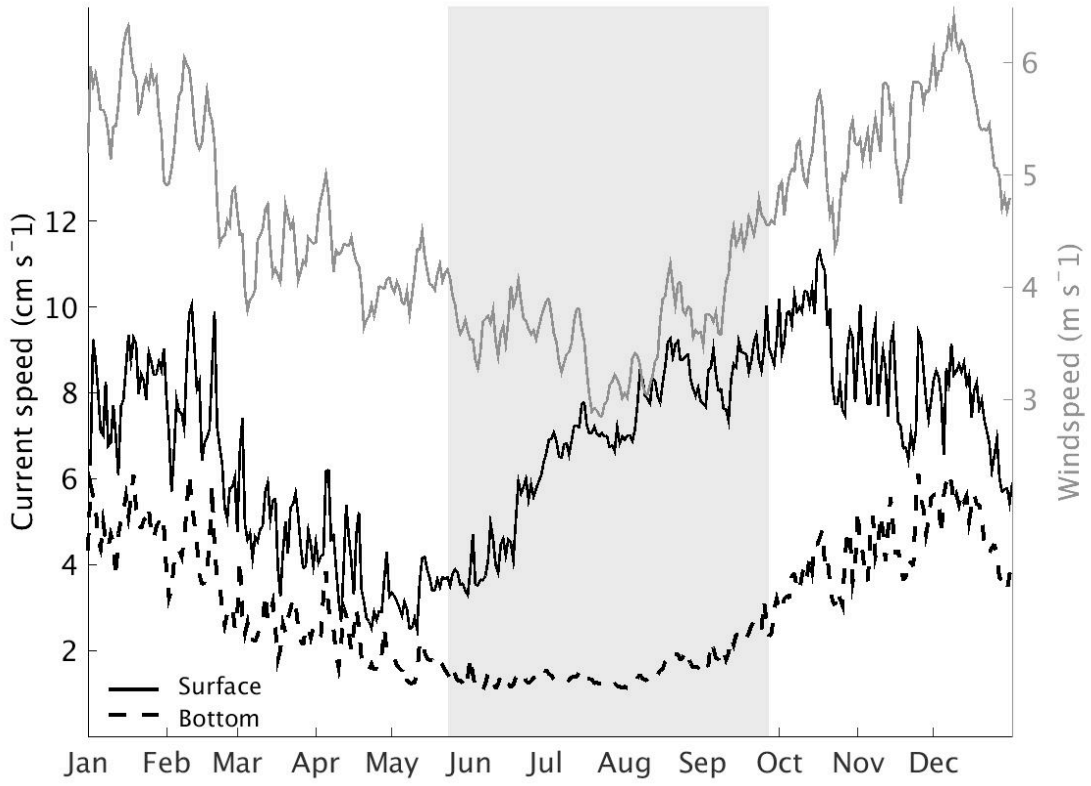

Figure 5. Mean nearshore current speed and windspeed, climatology. The mean was calculated over the entire nearshore zone. Shading indicates period of maximum nearshore-offshore exchange in the surface.

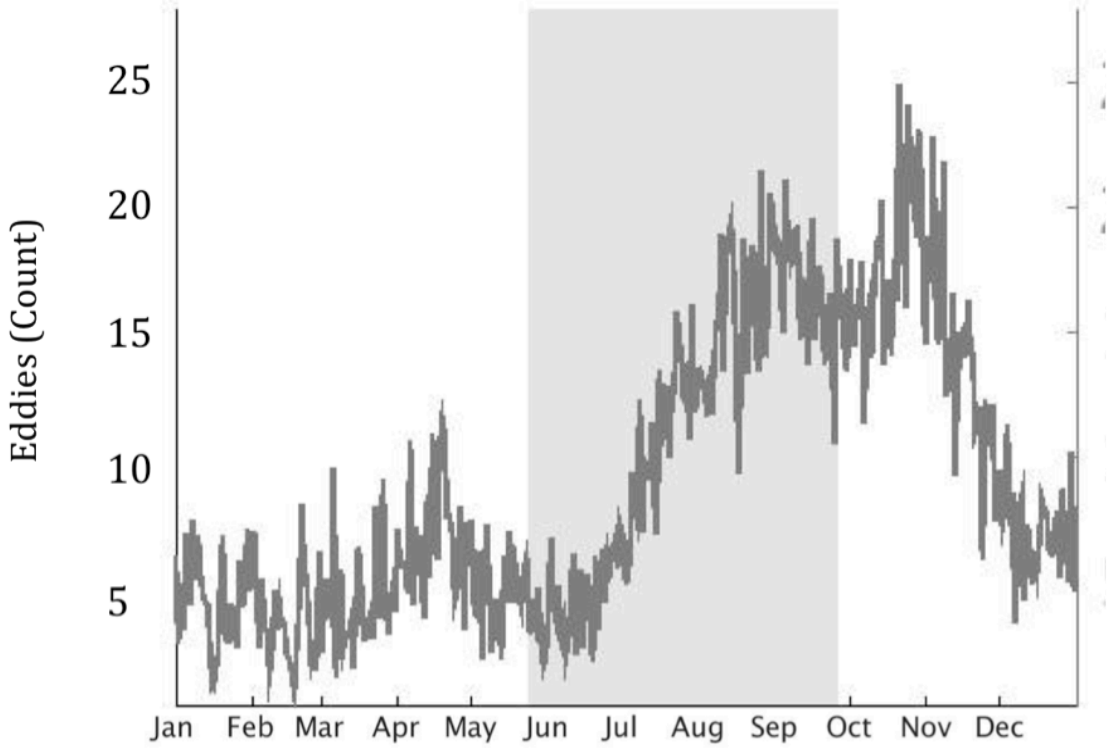

Figure 6. Number of eddies detected at the surface lakewide, climatology. The algorithm detects eddies based on the geometry of the current vectors. The lakewide total was smoothed using a 15 day average. Shading indicates period of maximum nearshore-offshore exchange in the surface.

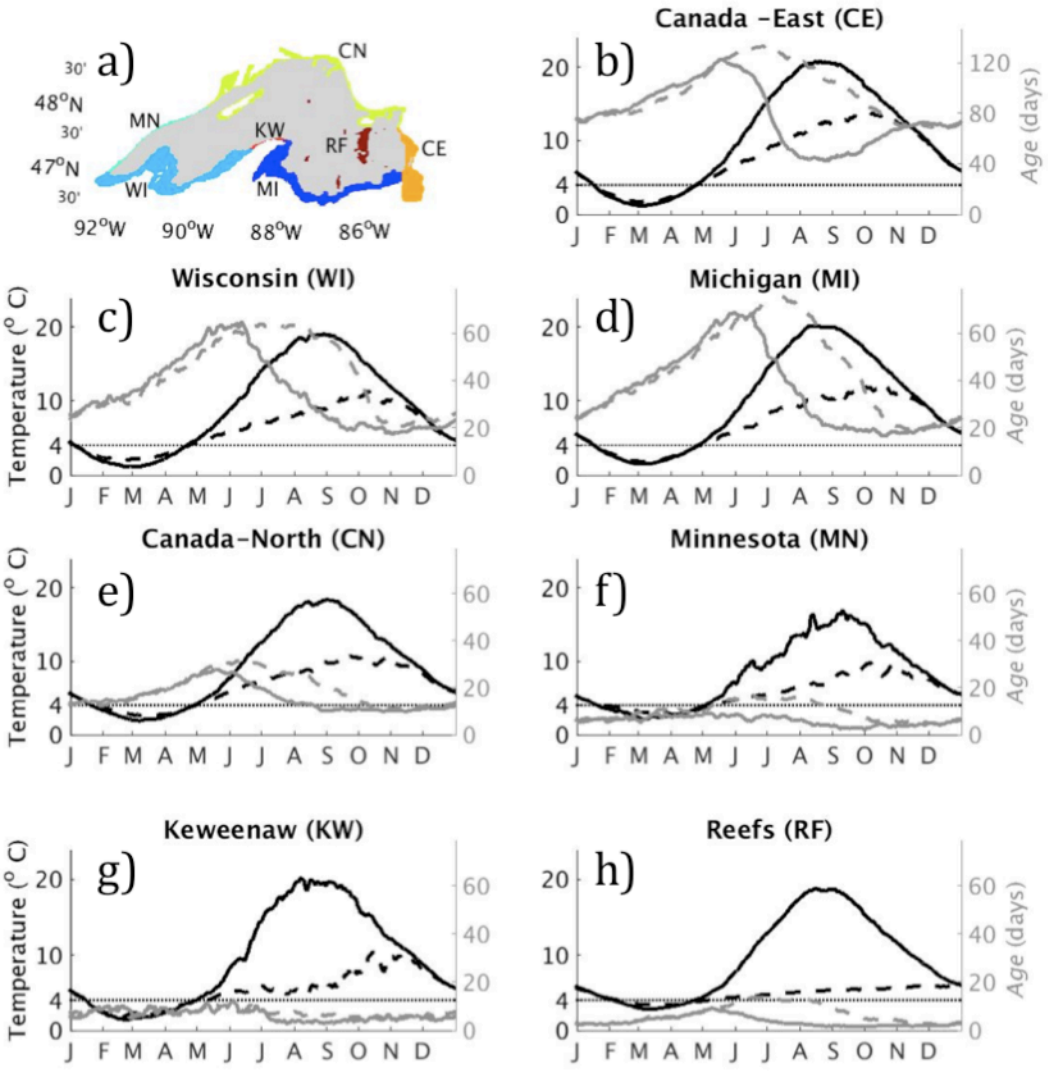

Figure 7. Temperature and *Age* climatology for each nearshore sector. Temperature values on left axis. Surface values are plotted with solid line, bottom layer values are plotted with dashed line. Note the scale of the right hand axis of the upper right panel (b) is twice that of the other panels. The mean was calculated over each individual nearshore sector.

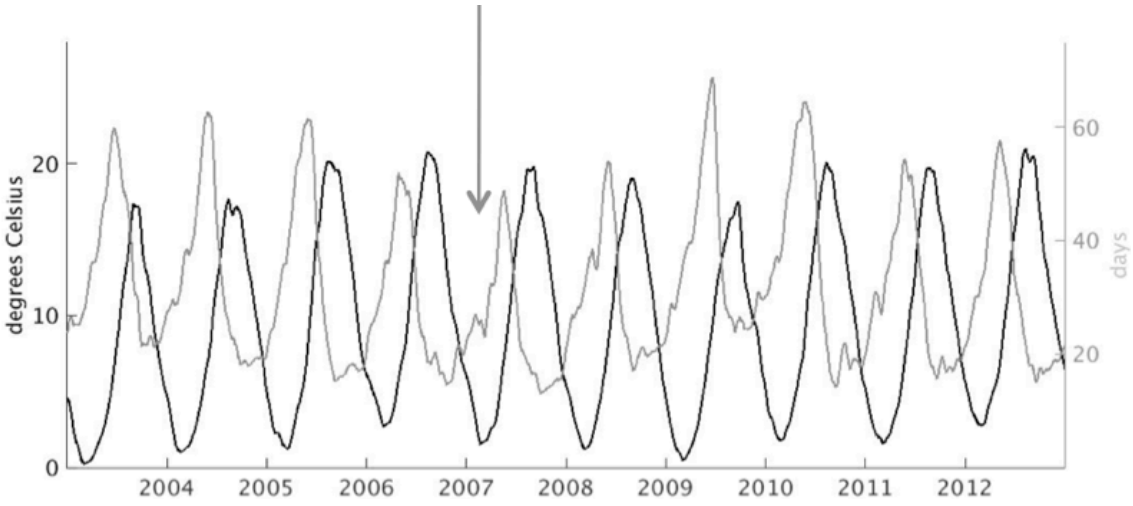

Figure 8. **Mean surface temperature and *Age* in the nearshore zone, 2003 2012.** Temperature (dark line) values are shown on left axis, maximum values of *Age* (lighter line) are shown on right axis. The mean was calculated over the entire nearshore zone. Arrow indicates period of sharp decline in *Age* in spring of 2007 discussed in text.

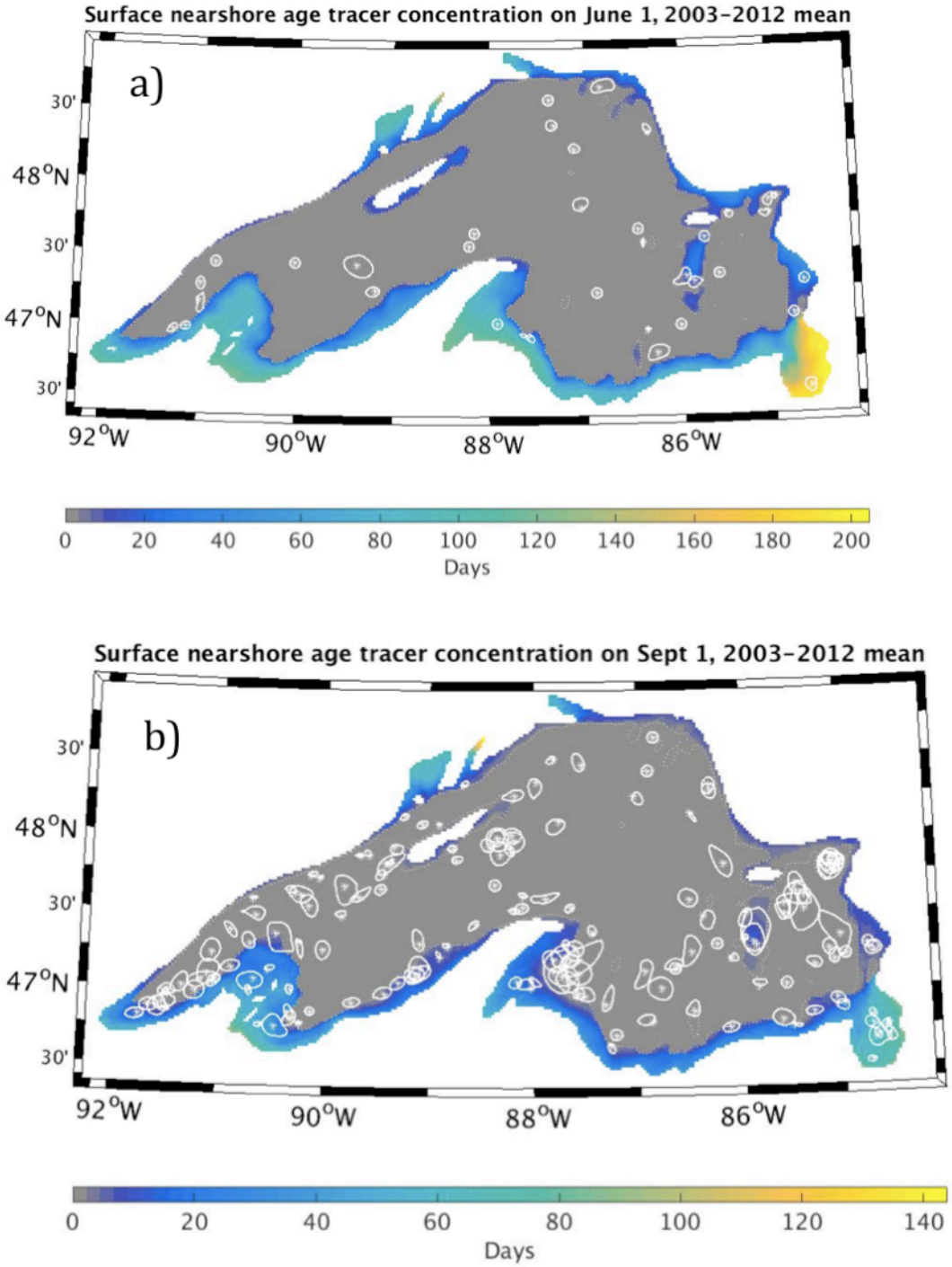

Figure 9. Eddies and average of surface *Age* on June 1 and Sept 1, climatology. The dates correspond to the annual maximum and minimum of the age tracer (Figure 9). All eddies detected by the eddy detection algorithm on April 1 and September 1 in each of the 10 years of the simulation are shown (circles). Note difference in color scale between the two figures.

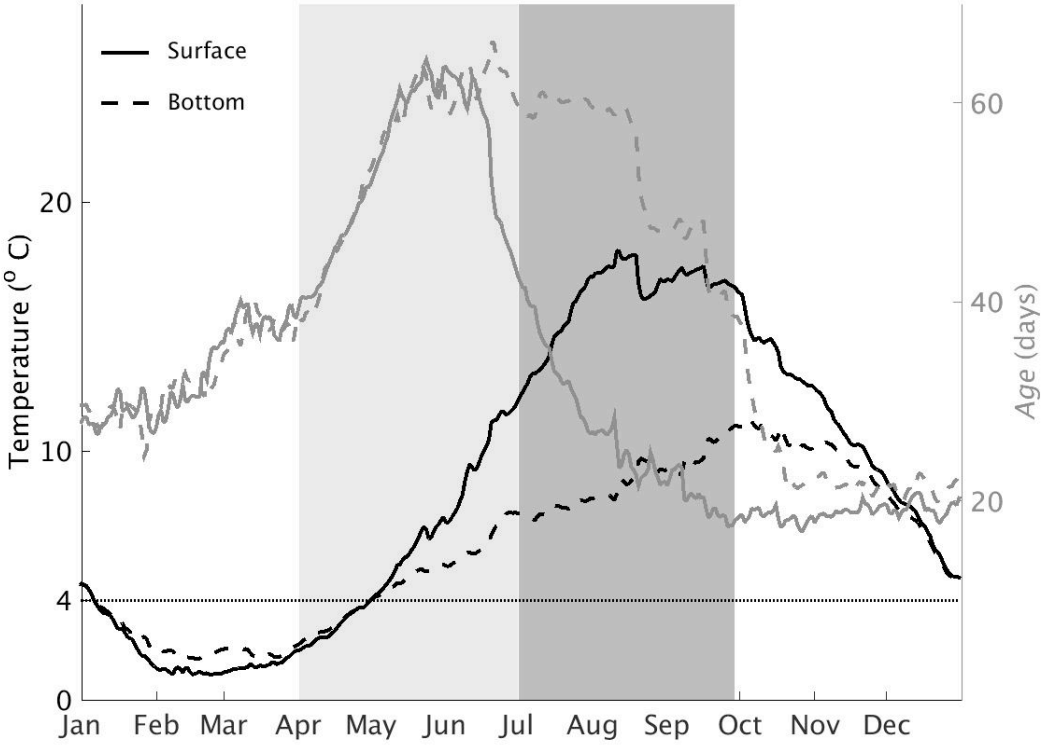

Figure 10. Mean nearshore *Age* tracer and temperature, 2004. The mean was calculated over the entire nearshore zone. The second series of simulations discussed in the text covers the two 90 day periods indicated by shading.

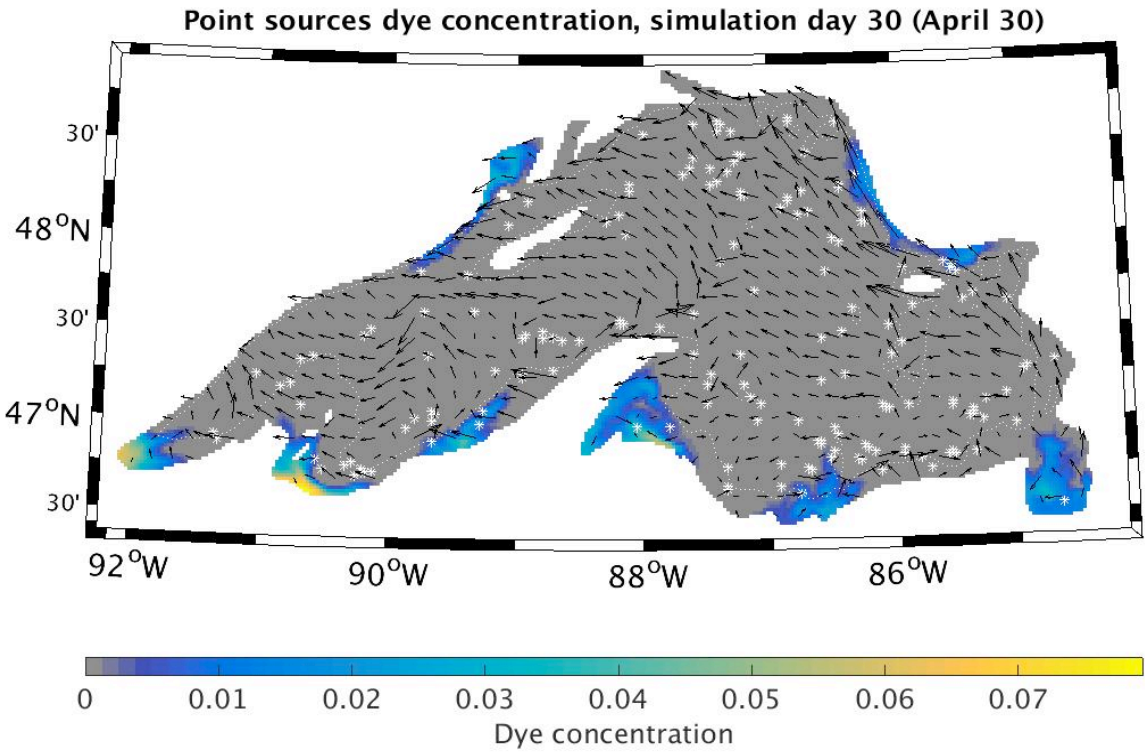

Figure 11a. Point sources surface distribution, early summer, day 30. Current vectors are the mean current over the preceding 30 days. All eddies detected in the previous 30 days are shown.

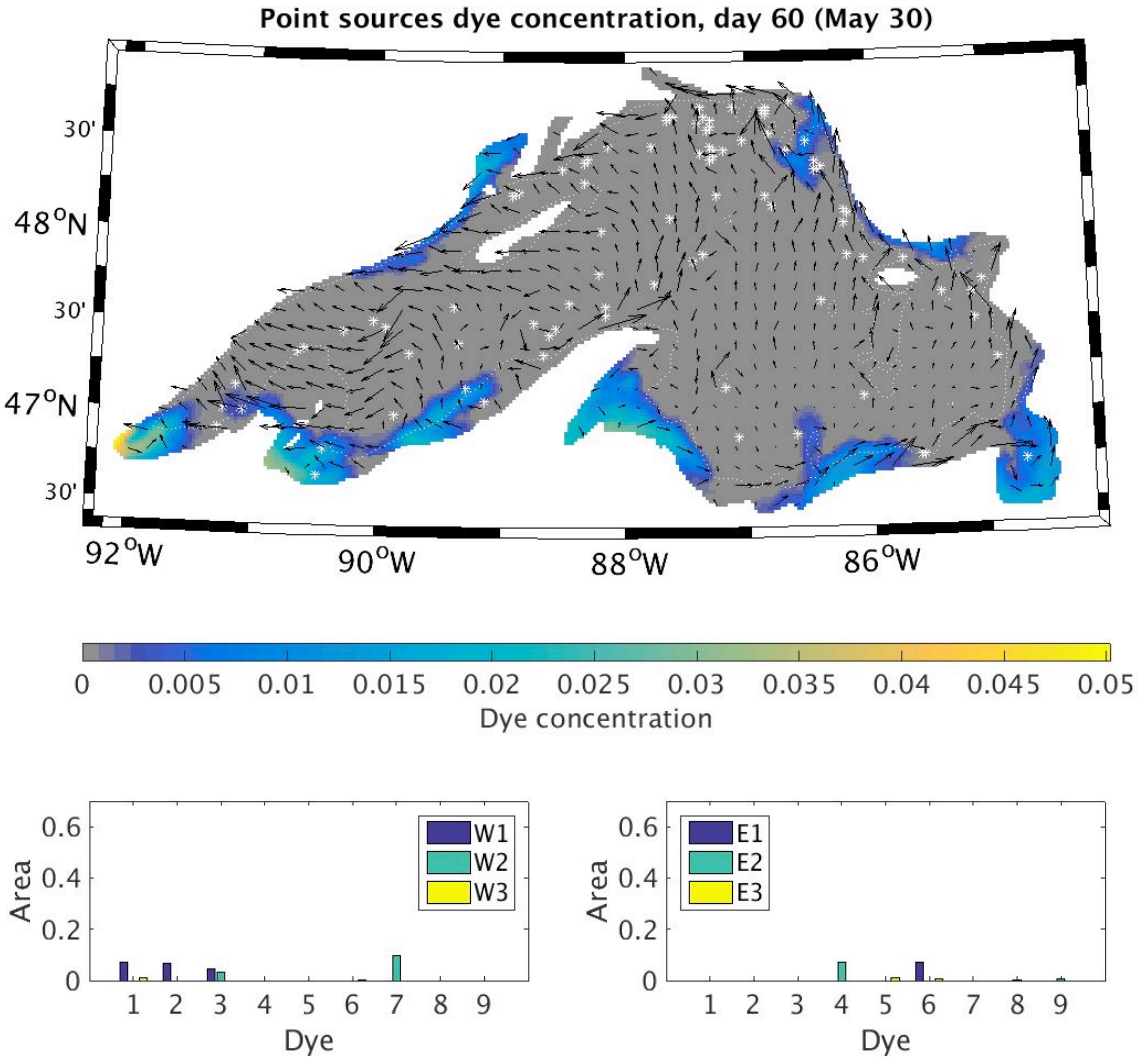

Figure 11b. Point sources surface distribution, early summer, day 60. Current vectors are the mean current over the preceding 30 days. All eddies detected in the previous 30 days are shown.

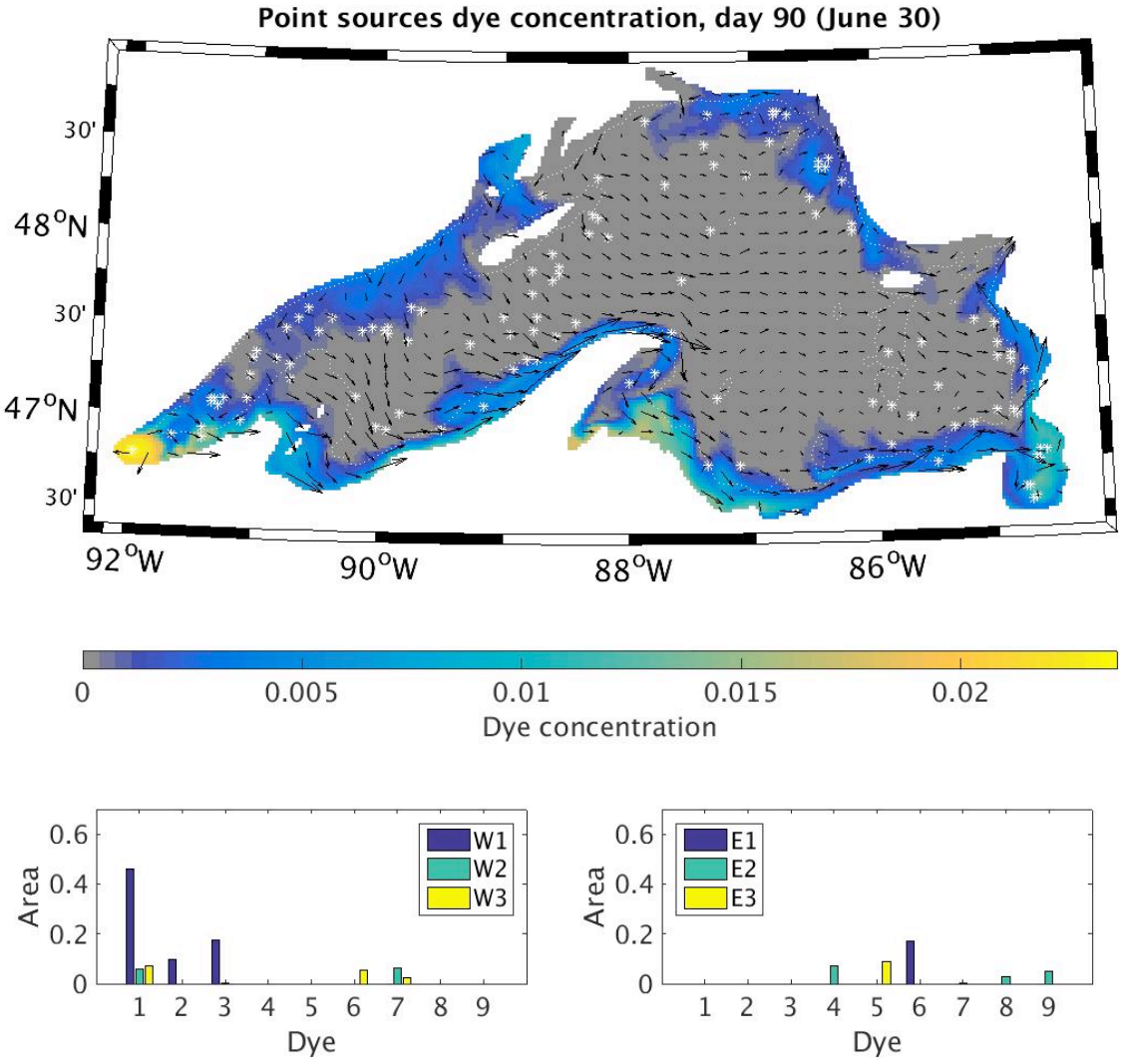

Figure 11c. Point sources surface distribution, early summer, day 90. Current vectors are the mean current over the preceding 30 days. All eddies detected in the previous 30 days are shown.

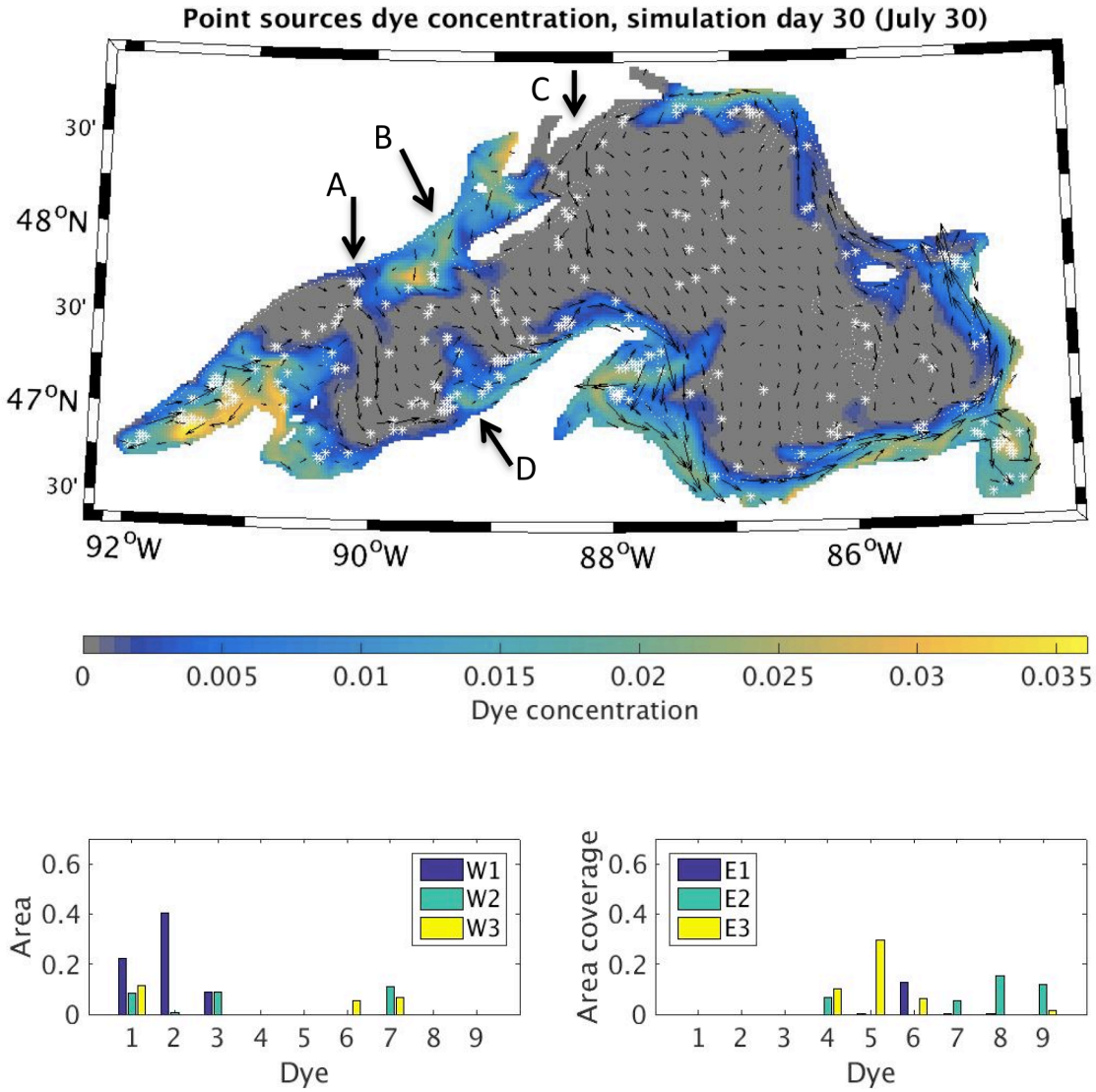

Figure 11d. Point sources surface distribution, late summer, day 30. Current vectors are the mean current over the preceding 30 days. All eddies detected in the previous 30 days are shown. Arrows A-D indicate location of currents discussed in the text.

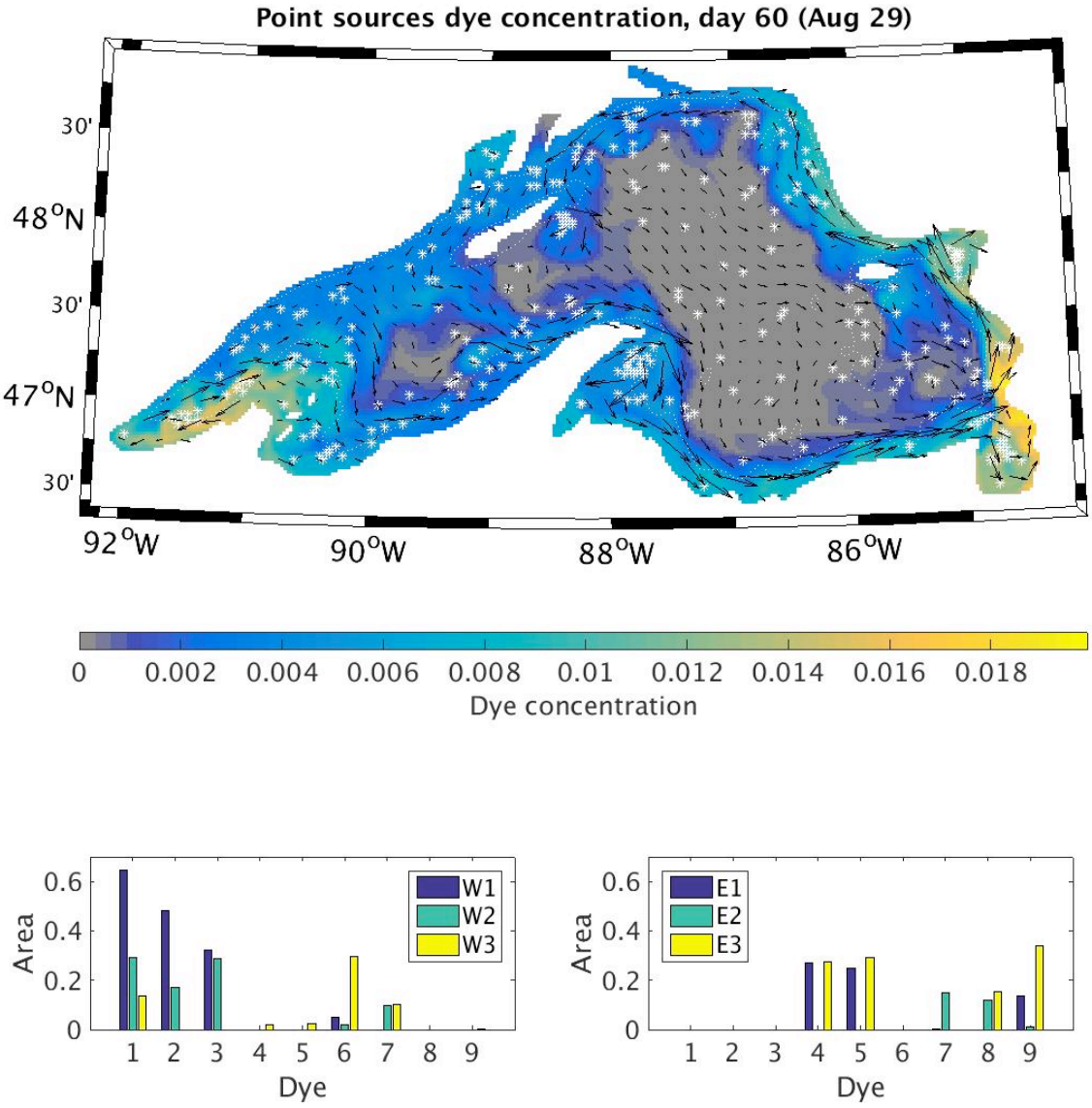

Figure 11e. Point sources surface distribution, late summer, day 60. Current vectors are the mean current over the preceding 30 days. All eddies detected in the previous 30 days are shown.

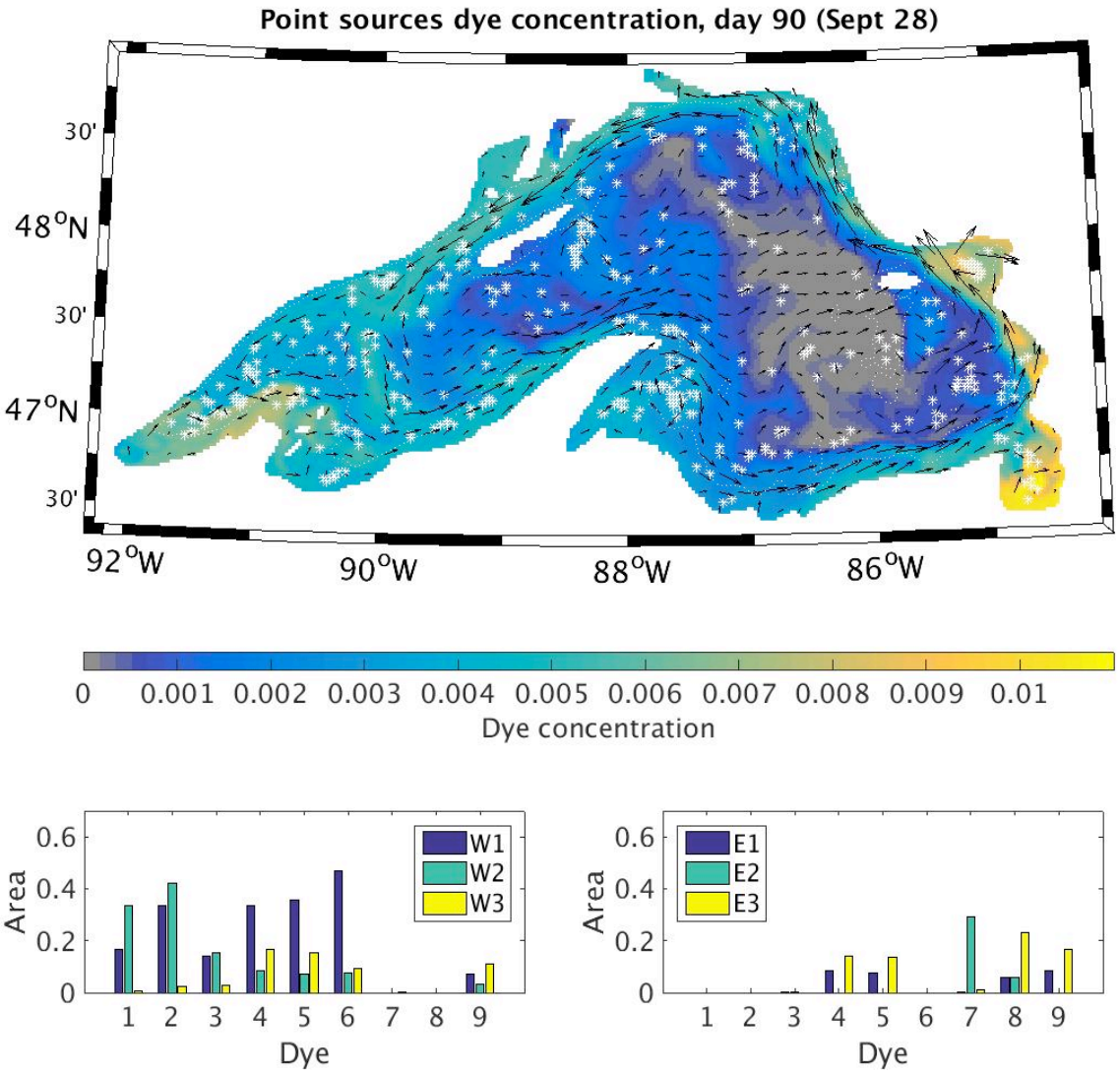

Figure 11f. Point sources surface distribution, late summer, day 90. Current vectors are the mean current over the preceding 30 days. All eddies detected in the previous 30 days are shown.

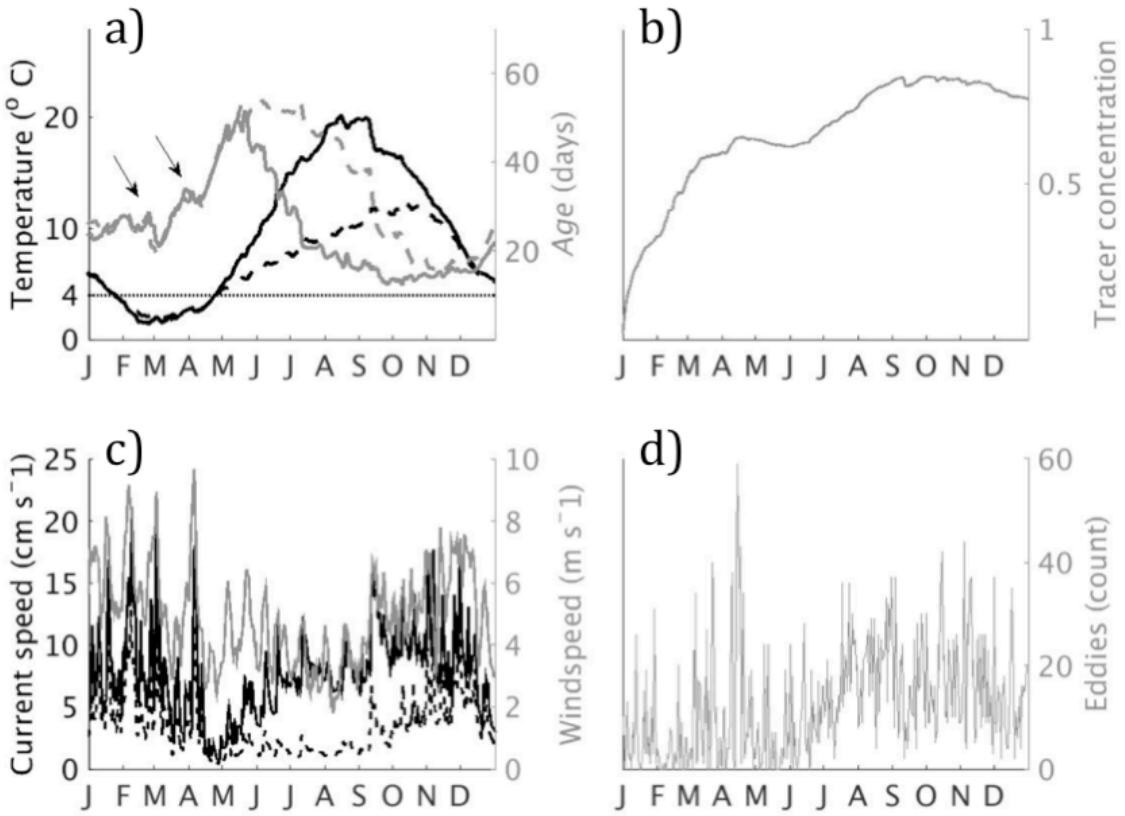

Figure 12. 2007 nearshore *Age* tracer, temperature, current and windspeed. A sharp drop in nearshore age (a) in mid spring is correlated with increases in nearshore dye in the offshore (b), current speed and windspeed (c) and the number of eddies (d).

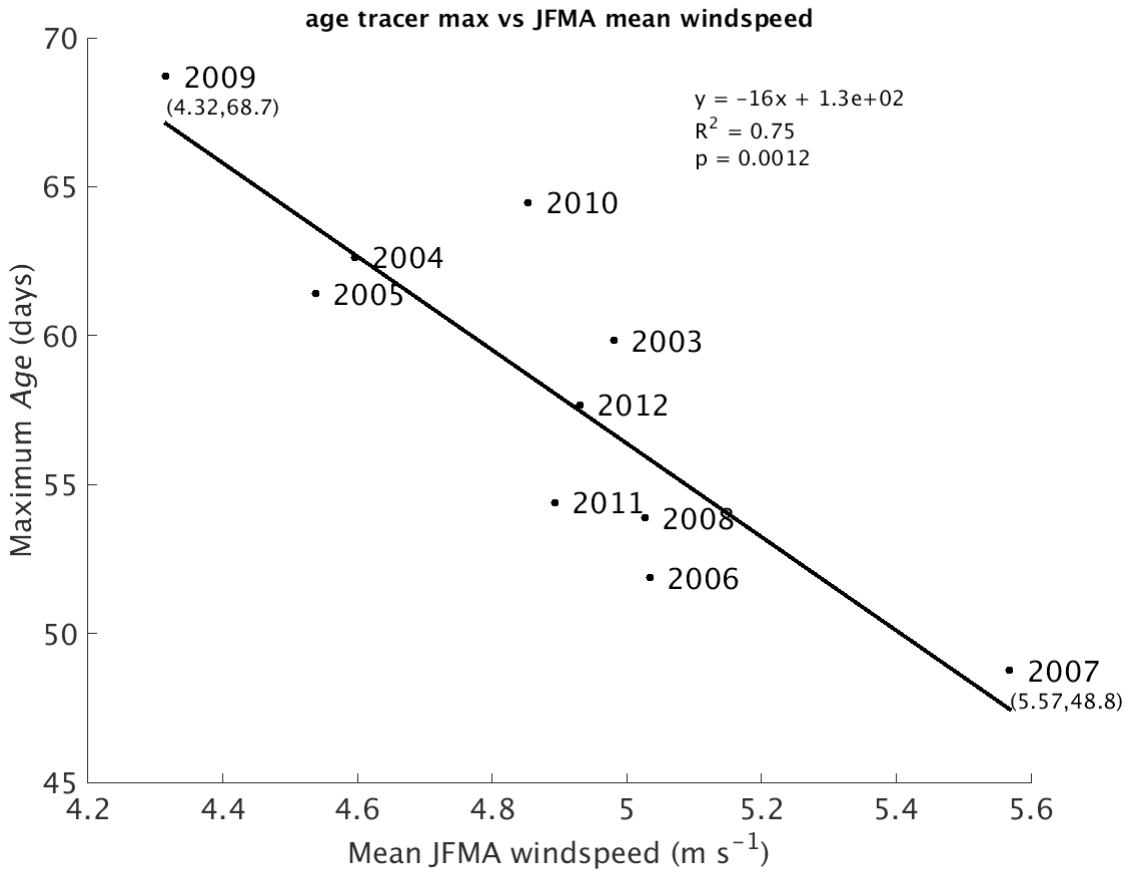

Figure 13. Correlation between springtime mean windspeed maximum of *Age*. The year with the highest *Age* was 2009, when the average windspeed was 4.3 m s^{-1}. The year with the lowest *Age* was 2007, when the average windspeed was 5.6 m s^{-1}.

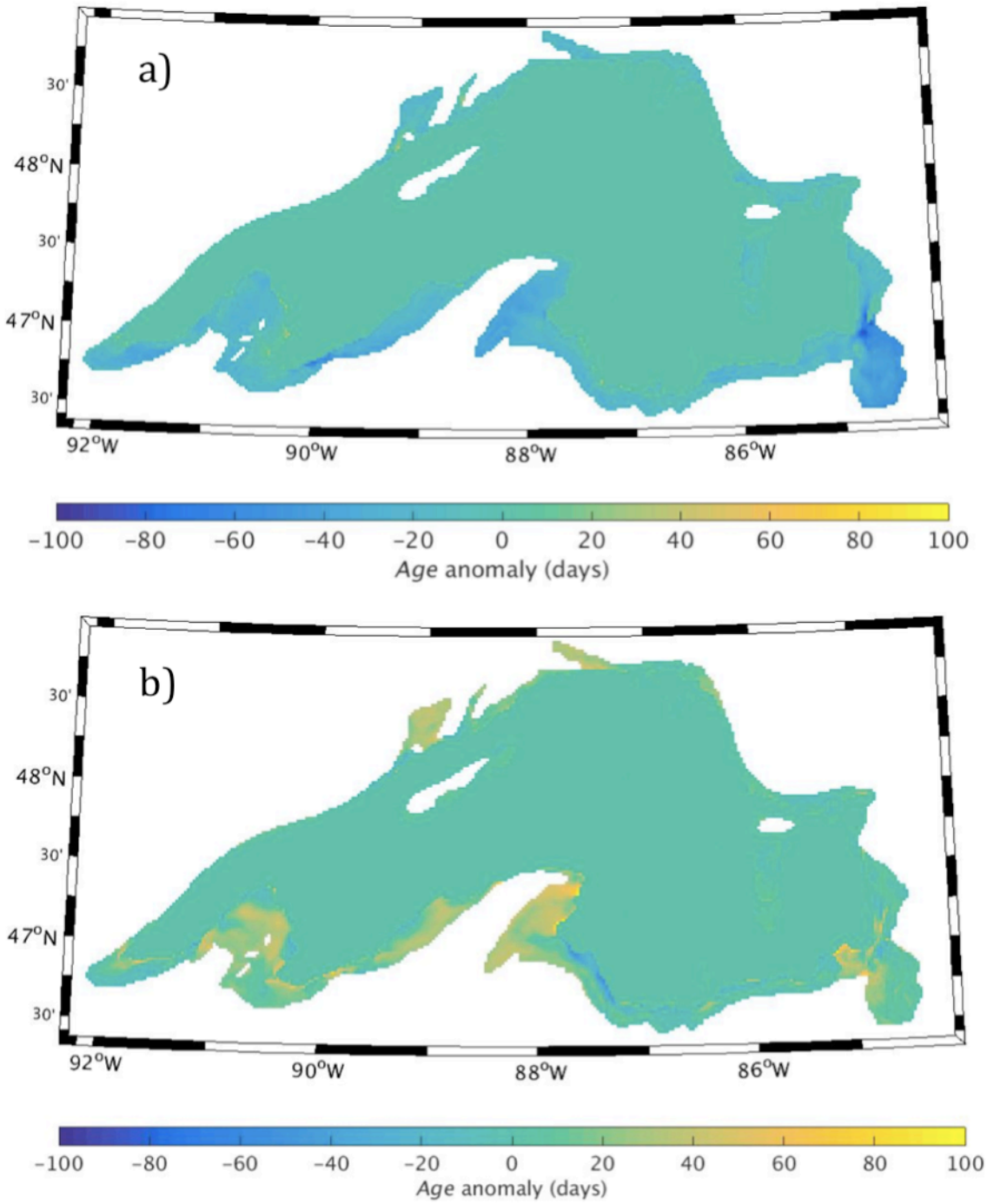

Figure 14. Anomaly of maximum *Age* tracer in 2007 and 2009. 2007 (a), a year with low cisco recruitment, and 2009 (b), a year with high recruitment. Higher *Age* in 2009, the result of low exchange between nearshore and offshore areas, would promote recruitment by retaining larvae within the nearshore zone where growth rates are higher.

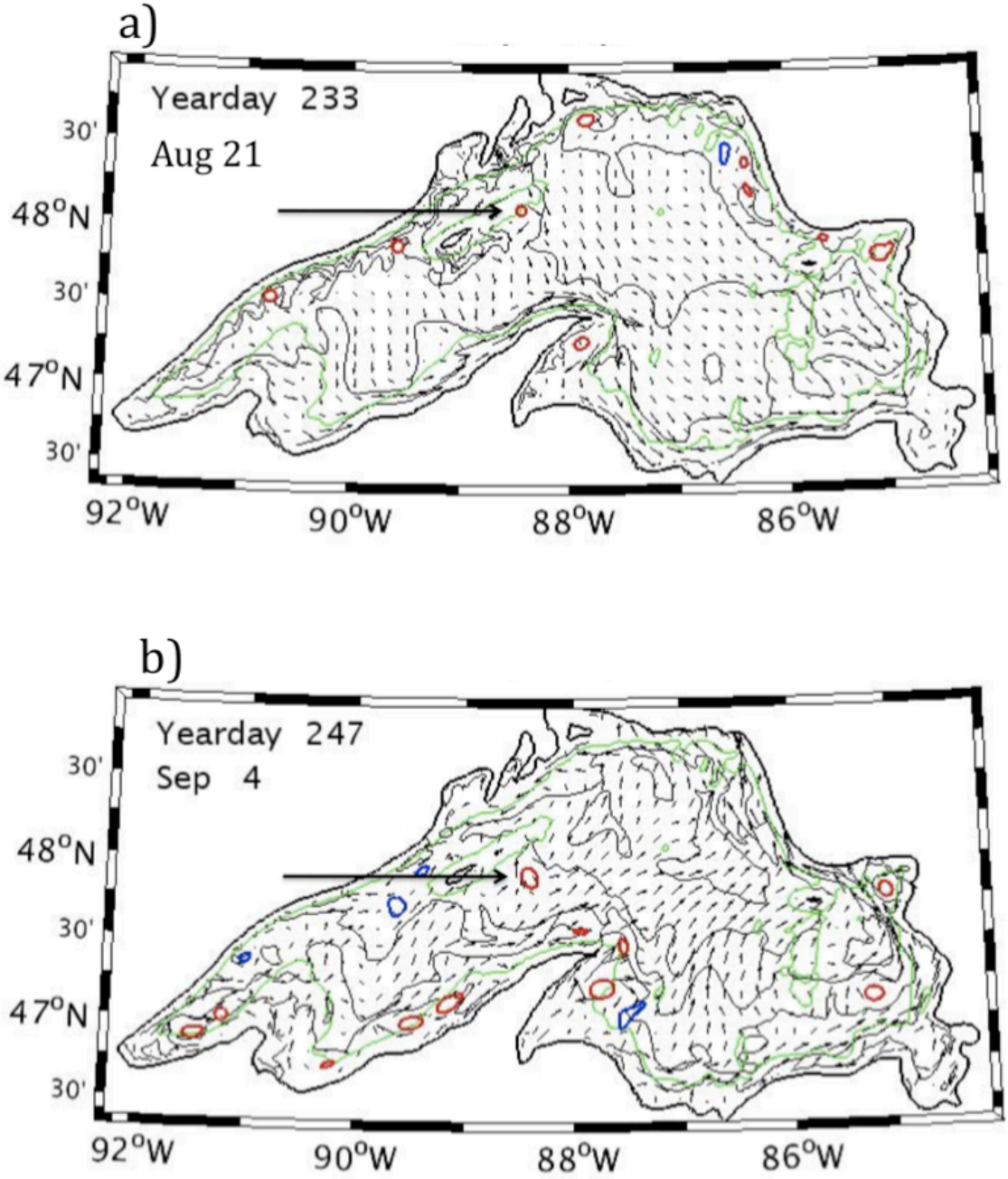

Figure 15. Eddy movement over 15 days. Two frames from a movie of model results showing the starting position (a) and final position (b) of an anticyclonic eddy that persists for 15 days and travels southeast from the northern tip of Isle Royale. Vectors indicate current direction, contours are surface temperature.

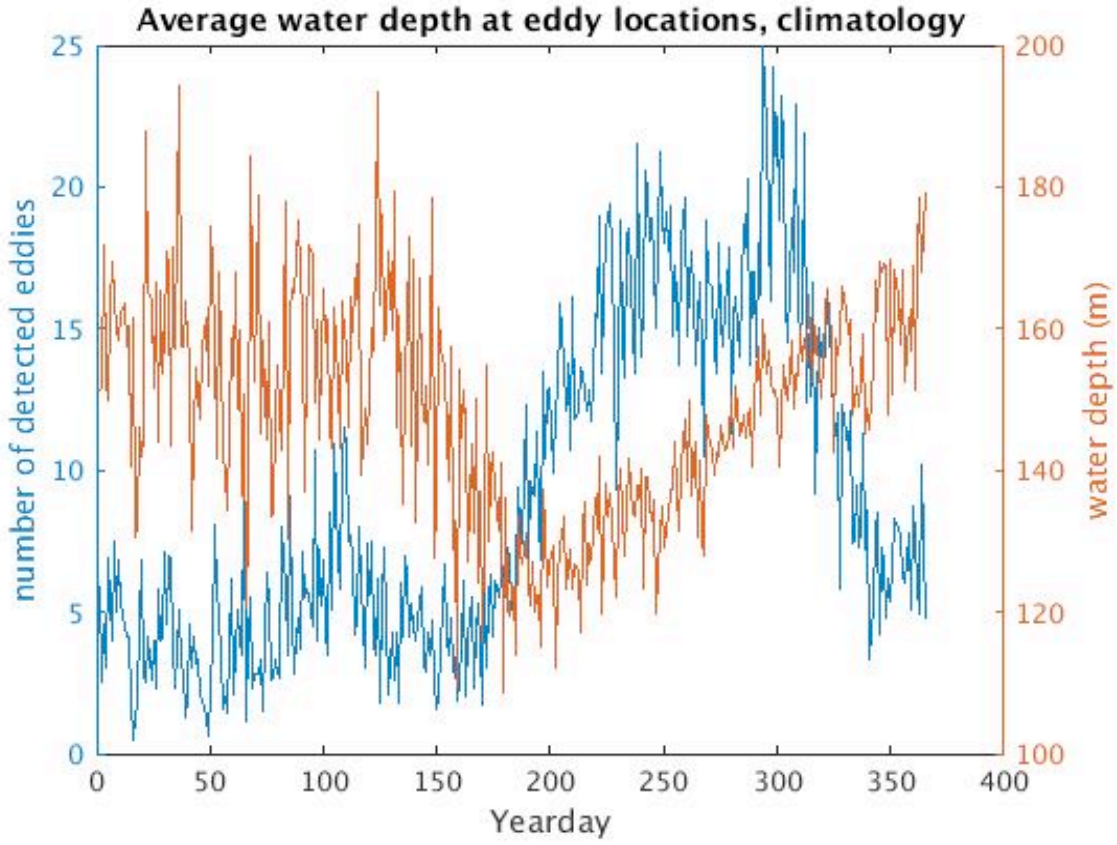

Figure 16. Climatology of eddy numbers by yearday and water depth. Number of eddies (left vertical axis) and water depth at the eddy center (right side vertical axis). The mean depth where eddies form exhibits a seasonal signal corresponding to the spread of stratification from shallow nearshore areas to deeper parts of the lake.

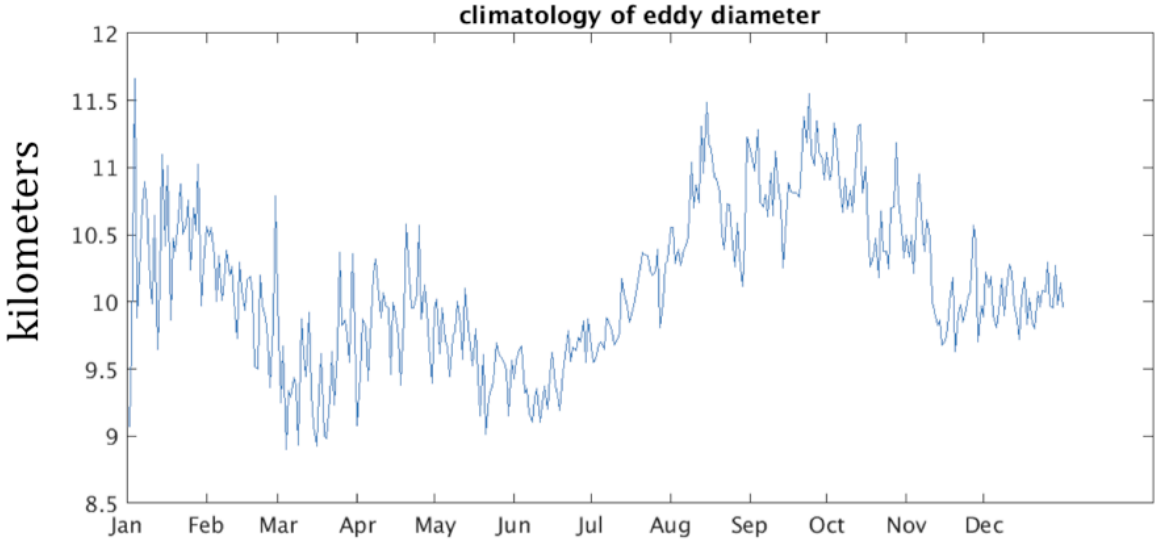

Figure 17. Mean eddy diameter, climatology. The daily mean values were smoothed using a 15 day moving average.

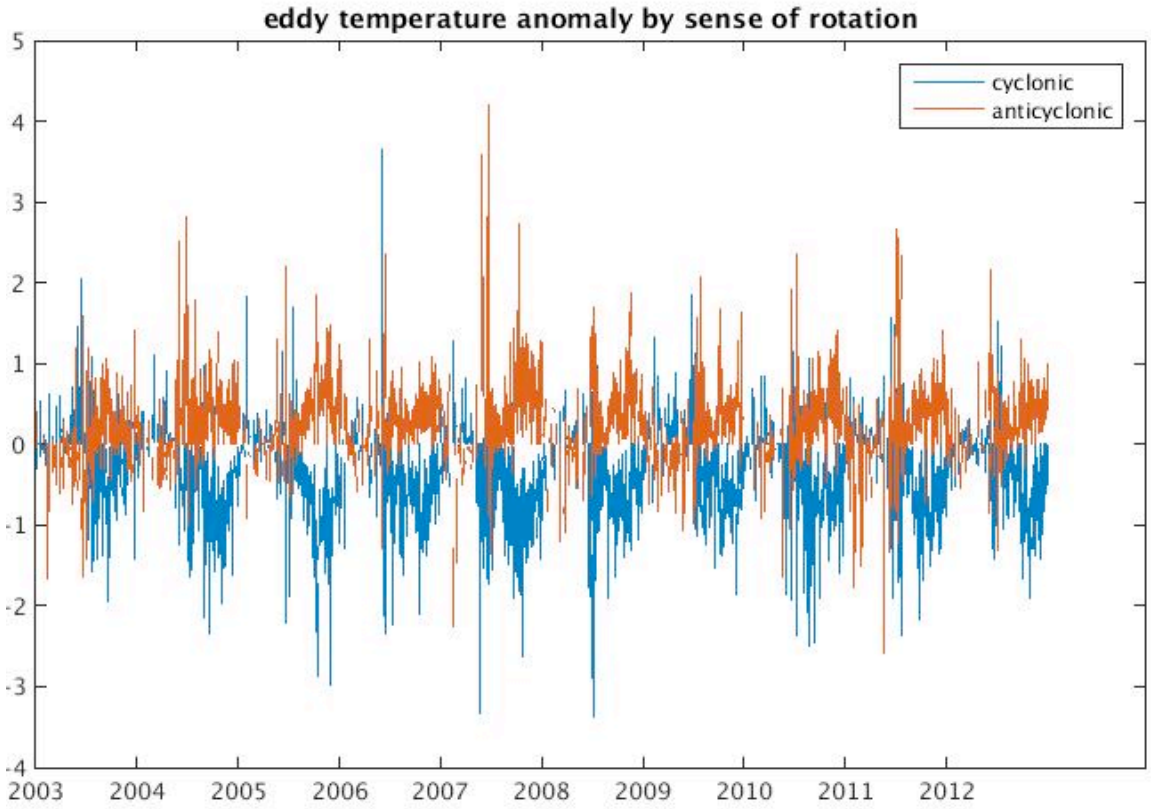

Figure 18. Temperature anomaly of eddies by sense of rotation. Anticyclonic eddies are warmer at their center than the daily mean eddy temperature in summer and colder in winter. Cyclonic eddies are opposite.

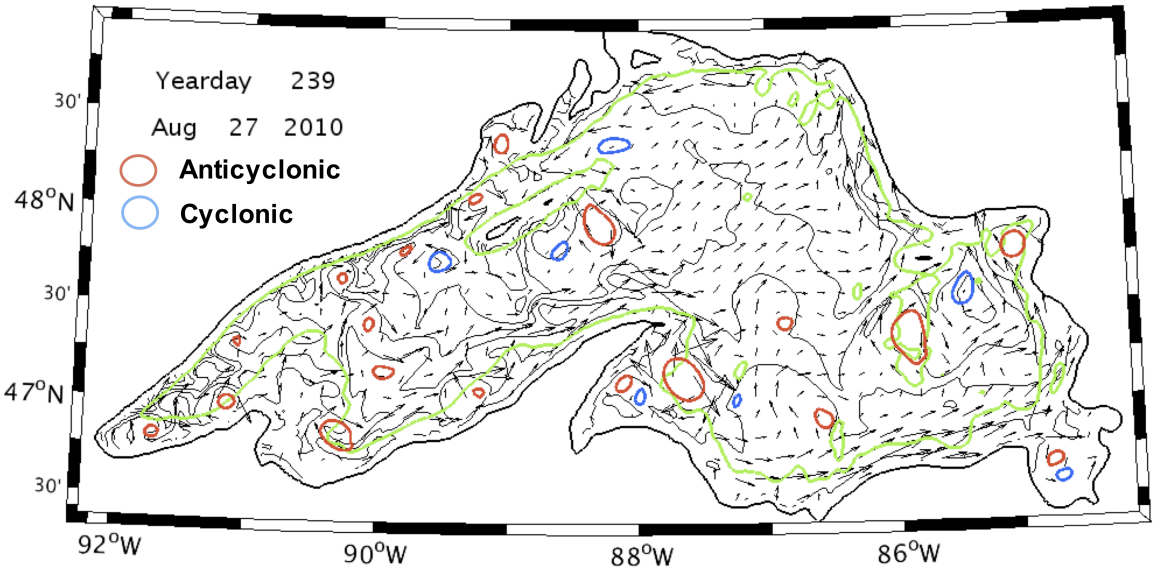

Figure 19. Model eddy distribution August 27, 2010. The distribution of the eddies is typical of the pattern in late summer in the 10 year simulation. The 100 meter depth contour indicated. Vectors indicate current direction. Contours are temperature.

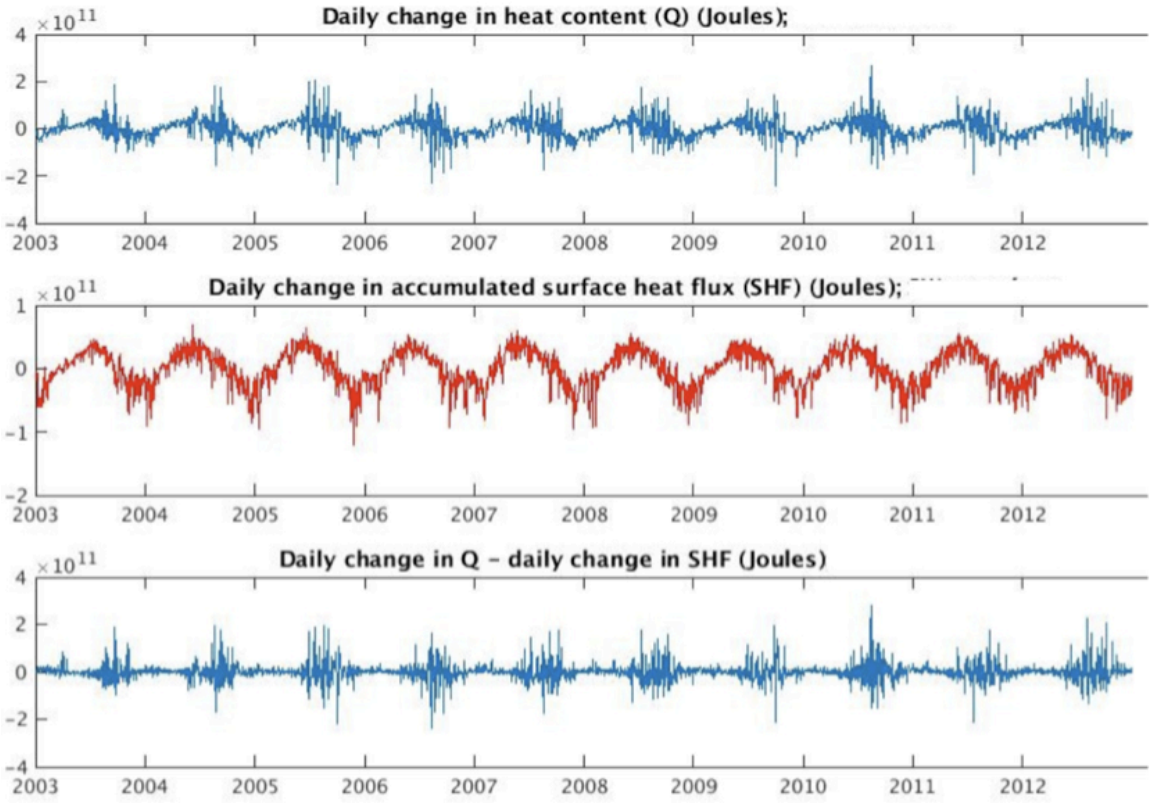

Figure 20. Daily change in heat content and surface heat flux, nearshore sector WI. Changes in daily heat content not attributable to surface heat flux occur during the late summer when eddy numbers peak.

Chapter 5: Conclusion

The world's large lakes are valuable freshwater resources that contain most of the world's available freshwater. They are unique among freshwater systems due to the presence of physical processes, including upwelling and eddies, that are more commonly found in marine settings. In the ocean, these physical processes help maintain biological communities, particularly in the nearshore, where they control important water quality parameters including concentrations of dissolved nutrients and heat. In lakes, these processes are potentially even more important because lakes are dominated by their coasts; the amount of nearshore area relative to offshore is greater than in the ocean. The objective of this dissertation was to study processes contributing to exchange between the nearshore and offshore in Lake Superior using a combination of satellite remote sensing and numerical modeling.

The major findings of this research include observations of eddies in the surface waters of Lake Superior, and modeling that helps define their occurrence and interaction with the seasonal coastal circulation. Eddies were detected using Synthetic Aperture Radar (SAR), the first application of this technique in the Great Lakes. The fine resolution SAR detected smaller eddies than had previously been reported using thermal satellite imagery, and contributed information about their scale, occurrence relative to wind forcing, and position relative to the nearshore thermal gradient that characterizes nearshore waters of Lake Superior during the summer months.

The modeling work was divided into an idealized component and a realistic component. The idealized modeling showed that in the basin with steep nearshore bathymetry, the rate of thermal bar migration during the fast stage was enhanced by the strength of the thermal gradient just behind the front and meanders that formed along the frontal boundary. Consistent with the greater instability, more eddies were detected in the circulation of the deep basin.

Areas where nearshore bottom slope is moderate frequently include estuaries and embayments. The simulation with the embayment grid showed that the presence of an embayment increased the rate of thermal bar migration during the fast stage by providing an additional source of heat to the nearshore zone behind the thermal front.

While the idealized model simulations considered only the thermal bar front, the nearshore areas of the Lake Superior are characterized by shore parallel thermal fronts throughout the summer months. The realistically configured model showed these fronts are sites of eddy generation throughout the summer. For example, a region of high nearshore bottom slope analogous to the deep basin is located along the northwest shore. In the realistically configured model, eddies repeatedly formed along that shore in summer and were associated with a recurring upwelling front parallel to shore.

In addition, the realistic model simulations in chapter four showed exchange between nearshore and offshore areas follows a seasonal cycle, and varies from place to place around the perimeter of the lake. My initial interest was in exploring how this variability might relate to recruitment of cisco, a keystone species in the lake. Results of the first series of simulations showed early spring wind events reduce the *Age* of water in

shelf areas, with higher *Age* significantly correlated with lower mean springtime windspeed. Comparison with published larval density reports revealed the year with the highest *Age* in the simulations corresponded to a year with high cisco recruitment, and conversely, the year with lowest *Age* corresponded to a year with low recruitment. This suggests the *Age* tracer captures an important property of nearshore water quality that could inform efforts to understand the sporadic recruitment pattern of cisco *Coregonus artedi*.

The eddy detection algorithm also revealed eddies were more common in the offshore areas of the western basin than in the east, and a period of high eddy activity in late summer corresponded to a the time when local changes in water column heat content in an offshore area were not attributable to surface heat flux.

In addition, eddies repeatedly formed where the coastal current encountered geographical features such as headlands and islands. An example showed the formation of a coherent eddy behind Isle Royale in the northwest and its drift to the southeast over the ensuing 15 days. These additional details about the occurrence and characteristics of eddies in the lake, and their possible role in offshore transport, could not be addressed in the observations reported in chapter 2. A higher resolution model, particularly one with higher resolution in the nearshore areas (Appendix 2) or new observational techniques would further increase that understanding.

As observational and modeling techniques have advanced, so has the understanding of how eddies participate in multiple processes (McWilliams, 2008). For example, some of the earliest observations were of coherent vortices with horizontal

scales of hundreds of km that persisted for years, during which time they transported water masses at depth, far from their origin (Schultz Tokos and Rossby, 1991). Eddies can at once isolate water masses, and homogenize water properties across frontal boundaries (Bower et al., 1985). Recent observations reveal the entire ocean surface is a dynamic field of eddies on multiple scales (Chelton et al., 2011). Could a similar picture emerge in the Great Lakes ?

Future understanding of eddies and other marine-scale processes within large lakes will likely include new modeling and observational techniques. For example, ROMS is based on the hydrostatic equations of motion and does not resolve some processes that could be important, particularly related to stratification. For example, the thermal bar depends on small changes in density that occur near T_{md}. The hydrostatic ROMS uses a convective adjustment approach in which the unstable vertical density profile at thermal bar is instantly mixed away. Some advanced models now use the non-hydrostatic equations and could potentially reveal new insights into physical processes in large lakes.

Observing the surface signature of dynamic processes involved in mixing and mass exchange, including eddies, in freshwater environments will likely be a valuable component of water management as the world's water cycle responds to climate change. The Surface Water and Ocean Topography (SWOT) mission currently being planned by NASA for launch in 2020 is designed to fill this need. Among other benefits, SWOT may be capable of resolving eddies in freshwater lakes using altimetry, similar to how they have been detected in the ocean over the past two decades.

References

Austin, J.A., Allen, J., 2011. Sensitivity of summer Lake Superior thermal structure to meteorological forcing. Limnol. Oceanogr. 56, 1141–1154.

Austin, J.A., Lentz, S.J., 2002. The Inner Shelf Response to Wind-Driven Upwelling and Downwelling. J. Phys. Oceanogr. 32, 2171–2193.

Auer, M. T., Gatzke, T. L., 2004. The Spring Runoff Event, Thermal Bar Formation, and Cross Margin Transport in Lake Superior. J. Great Lakes Res. 30, 64-81.

Auer, M. T., Auer, N.A., Urban, N.R., Bub, L., 2010. Primary production, carbon flux and the distribution of the amphipod *Diporeia* in Lake Superior. Verh. Internat. Verein. Limnol. 30, 1499-1504.

Auer, M. T., Auer, N.A., Urban, N.R., Auer, T., 2013. Distribution of the amphipod *Diporeia* in Lake Superior: The ring of fire. J. Great Lakes Res. 39, 33–46.

Beletsky, D., Saylor, J.H., Schwab, D.J., 1999. Mean Circulation in the Great Lakes. J. Gr. Lakes Res. 25, 78–93.

Bennett, E.B., 1978. Characteristics of the Thermal Regime of Lake Superior. J. Great Lakes Res. 4, 310–319.

Bennington, V., McKinley, G.A., Kimura, N., Wu, C.H., 2010. General circulation of Lake Superior: Mean, variability, and trends from 1979 to 2006. J. Geophys. Res. 115, C12015.

Bower, A. S., Rossby, H. T., Lillibridge. J.L., 1985. The Gulf Stream-barrier or blender? J. Phys. Oceanogr. 15, 24-32.

Budd, J.W., 2004. Large-scale Transport Phenomena in the Keweenaw Region of Lake Superior: the Ontonagon Plume and the Keweenaw Eddy. J. Great Lakes Res. 30, 467–480.

Chelton, D. B., Schlax, M. G., Samelson, R. M., 2011. Global observations of nonlinear mesoscale eddies. Progr. Oceanogr. 91, 167-216.

Chen, C., Zhu, J., Ralph, E., Green, S.A., Budd, J.W., Zhang, F.Y., 2001. Prognostic Modeling Studies of the Keweenaw Current in Lake Superior. Part I: Formation and Evolution. J. Phys. Oceanogr. 31, 379–395.

Chen, C., Xu, Q., Ralph, E., Budd, J.W., Lin, H., 2004. Response of Lake Superior to mesoscale wind forcing: A comparison between currents driven by QuikSCAT and buoy winds. J. Geophys. Res. 109, C10S02.

Chen, C.A., and Millero, F.J., 1986. Precise thermodynamic properties for natural waters covering only the limnological range. Limnol. Oceanogr. 31, 657-662. doi:10.4319/ lo.1986.31.3.0657

Consi, T.R., Anderson, G., Barske, G., Bootsma, H., Hansen, T., Janssen, J., Klump, V., Paddock, R., Szmania, D., Waples, J.T., 2009. Measurement of spring thermal stratification in Lake Michigan with the GLUCOS observing system, in: OCEANS 2009, MTS/IEEE Biloxi - Marine Technology for Our Future: Global and Local Challenges. Presented at the OCEANS 2009, MTS/IEEE Biloxi - Marine Technology for Our Future: Global and Local Challenges, 1–5.

Cotner, J. B., Biddanda, B. A., Makino, W., Stets, E., 2004. Organic carbon biogeochemistry of Lake Superior. Aquat. Ecosyst. Health Manag. 7, 451-464.

Csanady, G.T., 1975. Hydrodynamics of Large Lakes. Annu. Rev. Fluid. Mech. 7, 357–386.

DiGiacomo, P.M., Holt, B., 2001. Satellite observations of small coastal ocean eddies in the Southern California Bight. J. Geophys. Res. 106, 22,521–22,543.

Edsall, T.A., Charlton, M.N., 1997. Near-shore waters of the Great Lakes. In State of the Great Lakes Ecosystem Conference, 1996. US Environmental Protection Agency and Environment Canada, Windsor, Ont.

Elliot, G.T., 1971. A mathematical study of the thermal bar. Proc. 14th Conf. Great Lakes Res., Intern. Assoc. Great Lakes Res., 545-554.

Fahnenstiel, G., Pothoven, S., Vanderploeg, H., Klarer, D., Nalepa, T., Scavia, D., 2010. Recent changes in primary production and phytoplankton in the offshore region of southeastern Lake Michigan. J. Great Lakes Res. 36, Supplement 3, 20–29.

Fairall, C.W., Bradley, E.F., Rogers, D.P., Edson, J.B., Young, G.S., 1996. Bulk parameterization of air-sea fluxes for TOGA COARE. J. Geophys. Res. 101, 3747-3764.

Farrow, D. E., 1995. A numerical model of the hydrodynamics of the thermal bar. Journal of Fluid Mechanics, 303, 279-295.

Field, M.P., Sherrell, R.M., 2003. Direct determination of ultra-trace levels of metals in fresh water using desolvating micronebulization and HR-ICP-MS: application to Lake Superior waters. J. Anal. At. Spectrom. 18, 254–259.

Forel, F.A., 1880. La congélation des lacs Suisses et savoyards pendant l'hiver 1879-1880, Lac Léman. L'Écho des Alpes 3, 149–161.

Fu, L.-L., Holt, B., 1982. Seasat views oceans and sea ice with synthetic aperture radar, Publ. 81-120. Jet Propul. Lab., Pasadena, Calif.

Gbah, M. B., and Murthy, R. C., 1998. Characteristics of Turbulent Cross and Alongshore Momentum Exchanges During a Thermal Bar Episode in Lake Ontario. Nordic Hydrol. 29, 57–72.

Gorman, O.T., Evrard, L.M., Cholwek, G.A., Yule, D.L., Vinson, M.R., 2011. Status and Trends of Prey Fish Populations in Lake Superior, 2010. U.S. Geological Survey, Great Lakes Science Center, Lake Superior Biological Station, 2800 Lake Shore Dr. E., Ashland, WI 54806. Available online: http://www.glsc.usgs.gov/_files/reports/2010LakeSuperiorPreyfish.pdf

Harrington, M.W., 1895. Surface currents of the Great Lakes. U.S. Weather Bureau. Bulletin B.

Holland, P. R., and Kay, A., 2003. A review of the physics and ecological implications of the thermal bar circulation. Limnologica - Ecology and Management of Inland Waters 33, 153-162.

Holt, B., 2004. SAR Imaging of the Ocean Surface, in: Synthetic Aperture Radar Marine User's Manual. NOAA, Silver Spring, Md., 25–80.

Hubbard, D. W., and Spain, J. D., 1973. The structure of the early spring thermal bar in Lake Superior. In Proc. 16th Conf. Great Lakes Res., Intern. Assoc. Great Lakes Res., 735–742.

Ivanov, A., Zaitsev, V., Naumenko, M., Karetnikov, S., 1995. Study of the thermal bar and other hydrological phenomena in Lake Ladoga using ALMAZ-1 and ERS-1 SAR imagery. Proc. IGARSS'95, v.3, 1985-1987.

Johannessen, J.A., Shuchman, R.A., Digranes, G., Lyzenga, D.R., Wackerman, C., Johannessen, O.M., Vachon, P.W., 1996. Coastal ocean fronts and eddies imaged with ERS 1 synthetic aperture radar. J. Geophys. Res. 101, 6651–6667.

Kantha, L.H., and Clayson, C.A., 2000. Small Scale Processes in Geophysical Flows, Academic Press, San Diego.

Lam, D. C. L., 1978. Simulation of water circulations and chloride transports in Lake Superior for summer 1973. J. Great Lakes Res. 4, 343-349.

Li, X., Pichel, W., Clemente-Colon, P., Krasnopolsky, V., Sapper, J., 2001. Validation of coastal sea and lake surface temperature measurements derived from NOAA/AVHRR data, Int. J. Rem. Sens. 22, 1285-1303.

Likhoshway, Y.V., Kuzmina, A.Y., Potyemkina, T.G., Potyemkin, V.L., Shimaraev, M.N., 1996. The Distribution of Diatoms Near a Thermal Bar in Lake Baikal. J. Great Lakes Res. 22, 5–14.

Liu, W. T., Katsaros, K. B., Businger, J. A., 1979. Bulk parameterization of air-sea exchanges of heat and water vapor including the molecular constraints at the interface. J. Atmos. Sci. 36, 1722-1735.

Liu, A.K., Peng, C.Y., Schumacher, J.D., 1994. Wave-current interaction study in the Gulf of Alaska for detection of eddies by synthetic aperture radar. J. Geophys. Res. 99, 10,075–10,085.

Malm, J., Grahn, L., Mironov, D., Terzhevik, A., 1993. Field Investigation of the Thermal Bar in Lake Ladoga, Spring 1991. Nordic Hydrol. 24, 339-358.

Malm, J., Mironov, D., Terzhevik, A., Jonsson, L., 1994. Investigation of the Spring Thermal Regime in Lake Ladoga Using Field and Satellite Data. Limnol. Oceanogr. 39, 1333-1348.

Markovic, M., Jones, C.G., Winger, K., Paquin, D., 2009. The surface radiation budget over North America: gridded data assessment and evaluation of regional climate models. Inter. J. Climatol. 29, 2226-2240.

Marmorino, G.O., Holt, B., Molemaker, M.J., DiGiacomo, P.M., Sletten, M.A., 2010. Airborne synthetic aperture radar observations of “spiral eddy” slick patterns in the Southern California Bight. J. Geophys. Res. 115, C05010.

Matsumoto, K., Tokos, K. S., Gregory, C., 2015. Ventilation and dissolved oxygen cycle in Lake Superior: Insights from a numerical model. Geochem. Geophys. Geosyst. 16, doi:10.1002/2015GC005916.

McKinney, P., Holt, B., Matsumoto, K., 2012. Small eddies observed in Lake Superior using SAR and sea surface temperature imagery. J. Great Lakes Res. 38, 786-797.

McWilliams, J. C., 2008. The Nature and Consequences of Oceanic Eddies, in Ocean Modeling in an Eddying Regime (eds M. W. Hecht and H. Hasumi), American Geophysical Union, Washington, D. C.. doi: 10.1029/177GM03.

McWilliams, J.C., Colas, F., Molemaker, M.J., 2009. Cold filamentary intensification and oceanic surface convergence lines. Geophys. Res. Lett. 36, L18602.

Mesinger, F., et al., 2006. North American regional reanalysis, Bull. Am. Meteorol. Soc. 87, 343–360. doi:10.1175/BAMS-87-3-343.

Moll, R. A., Bratkovich, A., Chang, W. Y., Pu, P., 1993. Physical, chemical, and biological conditions associated with the early stages of the Lake Michigan vernal thermal front. Estuaries 16, 92-103.

Mortimer, C. H., 1988. Discoveries and testable hypotheses arising from Coastal Zone Color Scanner imagery of southern Lake Michigan. Limnol. Oceanogr. 33, 203-226.

Munk, W., Armi, L., Fischer, K., Zachariasen, F., 2000. Spirals on the Sea. Proceedings: Mathematical, Physical and Engineering Sciences 456, 1217–1280.

Myers, J. T., Yule, D. L., Jones, M. L., Ahrenstorff, T. D., Hrabik, T. R., Claramunt, R. M., Ebener, M.P., Berglund, E. K., 2015. Spatial synchrony in cisco recruitment. Fish. Res. 165, 11-21.

Niebauer, H.J., Green, T., Ragotzkie, R.A., 1977. Coastal Upwelling/Downwelling Cycles in Southern Lake Superior. J. Phys. Oceanogr. 7, 918–927.

Nencioli, F., Dong, C., Dickey, T., Washburn, L., McWilliams, J.C., 2010. A Vector Geometry–Based Eddy Detection Algorithm and Its Application to a High-Resolution Numerical Model Product and High-Frequency Radar Surface Velocities in the Southern California Bight. J. Atmos. Oceanic Technol. 27, 564–579. doi:10.1175/2009JTECH0725.1.

Paulson, C. A., Simpson, J. J., 1977. Irradiance measurements in the upper ocean. J. Phys. Oceanogr. 7, 952–956.

Quinn, F. H., 1992. Hydraulic residence times for the Laurentian Great Lakes. J. Great Lakes Res. 18, 22-28.

Ralph, E.A., 2002. Scales and structures of large lake eddies. Geophys. Res. Lett. 29, 2177. doi:10.1029/2001GL014654.

Rao, Y. R., Skafel, M. G., Charlton, M. N., 2004. Circulation and Turbulent Exchange Characteristics during the Thermal Bar in Lake Ontario. Limnol. Oceanogr. 49, 2190-2200.

Rao, Y.R., and Schwab, D.J., 2007. Transport and mixing between the coastal and offshore waters in the Great Lakes: a review. J. Great Lakes Res. 33, 202–218.

Rodgers, G. K., 1966. The thermal bar in Lake Ontario, spring 1965 and winter 1965-66. In Proc. 9th Conf. Gr. Lakes Res. Univ. Mich. Gr. Lakes Res. Div. 15, 369-374.

Rook, B.J., Hansen, M.J., Gorman, O.T., 2013. Biotic and abiotic factors influencing cisco recruitment dynamics in Lake Superior during 1978–2007. N. Am. J. Fish. Manag. 33, 1243–1257.

Schertzer, W.M., Rao, Y.R., 2009. An overview of the characteristics of Lake Superior Meteorology, Hydrology and Physical Limnology in Munawar, M., Munawar, I.F., (Eds.) State of Lake Superior, Ecovision World Monograph Series.

Schultz Tokos, K., Rossby, T., 1991. Kinematics and dynamics of a Mediterranean salt lens. J. Phys. Oceanogr. 21, 879-892.

Shchepetkin, A.F., McWilliams, J.C., 2005. The regional oceanic modeling system (ROMS): a split-explicit, free-surface, topography-following-coordinate oceanic model. Ocean Modelling 9, 347–404.

Sierszen, M. E., Hrabik, T. R., Stockwell, J. D., Cotter, A. M., Hoffman, J. C., Yule, D. L., 2014. Depth gradients in food‐web processes linking habitats in large lakes: Lake Superior as an exemplar ecosystem. Freshwater Biology 59, 2122-2136.

Sloss, P.W., Saylor, J.H., 1976. Large-Scale current measurements in Lake Superior. NOAA Tech. Rep. ERL 363 GLERL 8.

Steissberg, T.E., Hook, S.J., Schladow, S.G., 2005. Measuring surface currents in lakes with high spatial resolution thermal infrared imagery. Geophys. Res. Lett. 32, L11402, doi:10.1029/2005GL022912.

Sterner, R.W., 2010. In situ-Measured Primary Production in Lake Superior. J. Great Lakes Res. 36, 139–149.

Schultz Tokos, K., Rossby, T., 1991. Kinematics and dynamics of a Mediterranean salt lens. J. Phys. Oceanogr. 21, 879-892.

Tikhomirov, A. I., 1963. The thermal bar in Lake Ladoga. Soviet Hydroloy Selected Papers, AGU Trans. 95, 134-142.

Troy, C.D., Ahmed, S., Hawley, N., Goodwell, A., 2012. Cross-shelf thermal variability in southern Lake Michigan during the stratified periods. J. Geophys. Res. 117, C02028.

Ullman, D., Brown, J., Cornillon, P., Mavor, T., 1998. Surface temperature fronts in the Great Lakes. J. Great Lakes Res. 24, 753-775.

Van Luven, D.M., Huntoon, J.E., Maclean, A.L., 1999. Determination of the Influence of Wind on the Keweenaw Current in the Lake Superior Basin as Identified by Advanced Very High Resolution Radiometer (AVHRR) Imagery. J. Great Lakes Res. 25, 625–641.

Watson, N.H., Wilson, J.B., 1978. Crustacean zooplankton of Lake Superior. J. Great Lakes Res. 4, 481-496.

White, B., Austin, J., Matsumoto, K., 2012. A three-dimensional model of Lake Superior with ice and biogeochemistry. J. Great Lakes Res. 38, 61–71.

White, B., Matsumoto, K., 2012. Causal mechanisms of the deep chlorophyll maximum in Lake Superior: A numerical modeling investigation. J. Great Lakes Res. 38, 504-513.

Wilson, M.C., Shore, J.A., Rao, Y.R., 2013. Sensitivity of the simulated Kingston Basin – Lake Ontario summer temperature profile using FVCOM. Atmosphere-Ocean 51, 319-331.

Winstead, N.S., Sikora, T.D., Thompson, D.R., Mourad, P.D., 2002. Direct Influence of Gravity Waves on Surface-Layer Stress during a Cold Air Outbreak, as shown by Synthetic Aperture Radar. Mon. Wea. Rev. 130, 2764.

Wurl, O., Wurl, E., Miller, L., Johnson, K., Vagle, S., 2011. Formation and global distribution of sea-surface microlayers. Biogeosciences 8, 121–135.

Yurista, P., Kelly, J.R., Miller, S.E., 2011. Lake Superior: nearshore variability and a landscape driver concept. Aquat. Ecosyst. Health Mgmt. 14, 345-355.

Zhu, J., Chen, C., Ralph, E., Green, S.A., Budd, J.W., Zhang, F.Y., 2001. Prognostic Modeling Studies of the Keweenaw Current in Lake Superior. Part II: Simulation. J. Phys. Oceanogr. 31, 396–410.

Appendix 1 : Field observations of the springtime thermal bar in Lake Superior.

In the spring of 2012, I conducted a field trip to observe the thermal bar in Lake Superior. The field work was conducted in the vicinity of Bark Point, located on the south shore of Lake Superior between Herbster and Cornucopia, Wisconsin. I used small boats including canoe, kayak and small fishing boat that could be launched easily, and portable hand-held CTD and GPS instruments. Water temperature measurements at the surface were recorded along with GPS coordinates for comparison with satellite images of lake surface temperature. Subsurface temperatures were also recorded in order to determine the three dimensional temperature structure of the thermal bar.

I selected the date and location for the field work by monitoring lake surface temperatures using satellite products available online through the NOAA Coastwatch program and Michigan State University[5]. In general, I was looking for the transition zone between nearshore areas that had stratified with surface temperatures above 4 °C and offshore areas where surface temperatures were at or below that temperature.

In areas where bottom slope is consistent in the alongshore direction, the thermal bar (4 °C isotherm) is parallel to shore. Most of the south shore has a moderate bottom slope where the thermal bar moves relatively quickly offshore to a distance 10 or more km offshore where it is clearly resolved in the satellite images, which have a pixel size of approximately 2 km. This was further offshore than I wanted to venture using the small boats.

---

[5] http://www.coastwatch.msu.edu/twosuperiors.html

Near Bark Point, the bottom slope increases (Figure 1), and as a result of the deeper water, the width of the stratified area shoreward of the thermal bar is narrower in that area (Figure 2). I used the relatively coarse resolution satellite images to monitor water temperatures along the south shore. After the thermal bar was clearly visible in the satellite images, I visited the Bark Point area and located the 4 °C temperature front manually by measuring surface temperatures perpendicular to shore. After locating where temperatures were colder than 4 °C, I turned back towards shore and began recording water temperatures at 400 meter intervals.

Figure 3 shows the temperatures measured at the surface and at depth during the transect from 4.5 km from shore, where surface temperatures were below 4 °C, to a station 0.5 km from the tip of Bark Point. The cross section (a) shows that while in general, the isotherms form a wedge of warm water near shore, there is asymmetry from approximately 3.25 to 4.5 km from shore where the 4 °C isotherm extends further from shore than the extension of the subsurface wedge. This feature, described in the literature as a tongue of warm water, is characteristic of the later stage in thermal bar development, in which the advection velocity behind the 4 °C isotherm (thermal bar) is faster than its propagation speed predicted by one dimensional models.

Debris was observed at the surface 2.5 km behind where the 4 °C isotherm was observed at the surface; temperatures near the bottom at that station were warmer than inshore (Figure 3, arrows) suggesting a zone of convergence and downwelling occurred roughly half-way from shore to the 4 °C isotherm. The debris included insects that apparently had recently hatched, and pollen (Figure 4).

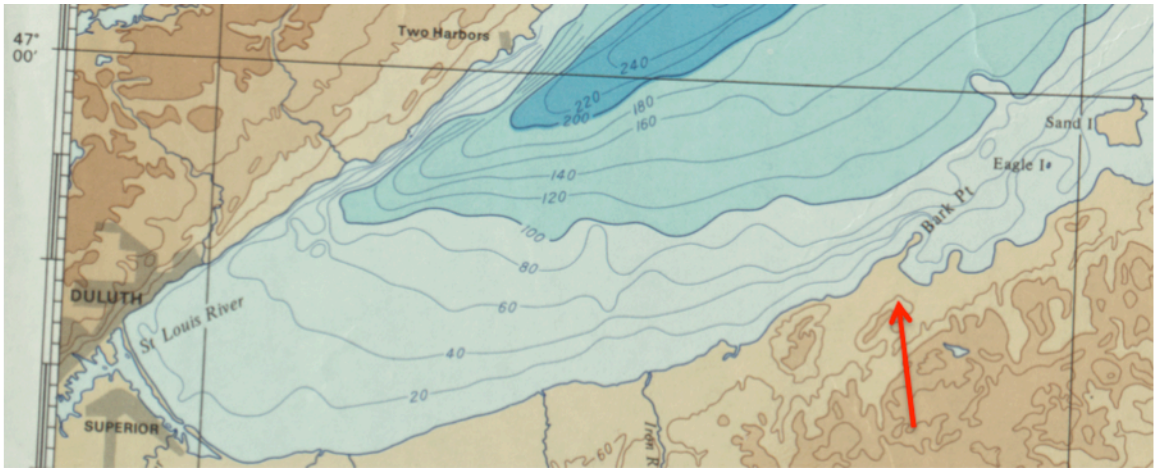

Figure 1. **Location and bathymetry of field area.** Excerpted from Lake Superior bathymetric chart published by the Canadian Hydrographic service (Publication 885, first edition, 1973). The narrowing of the shelf width in the vicinity of Bark Point Wisconsin is shown (arrow).

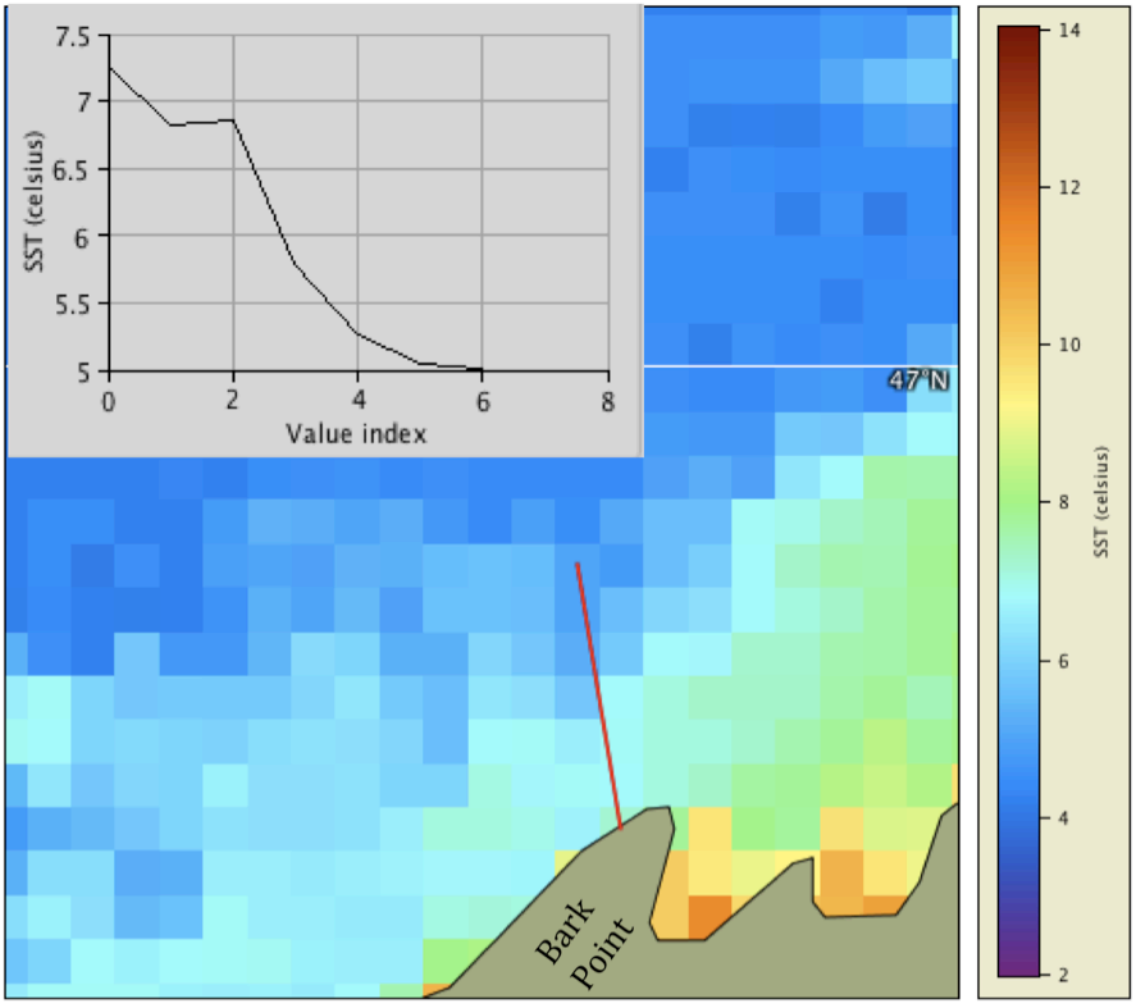

Figure 2. Satellite-based surface temperature in field area. Temperatures derived from AVHRR data obtained May 11 2012, 02:28 UTC (May 10, 2012, 9:28 pm CDT). Temperature plot corresponds to red line, which corresponds to the transect where surface temperatures were measured . The satellite derived temperatures are 1 °C warmer than observed earlier in the day. Image obtained from the NOAA CLASS website at http://www.class.ncdc.noaa.gov. Figure produced using the Coastwatch data analysis tool available at http://coastwatch.noaa.gov/cwn/cw_software.html.

(a)

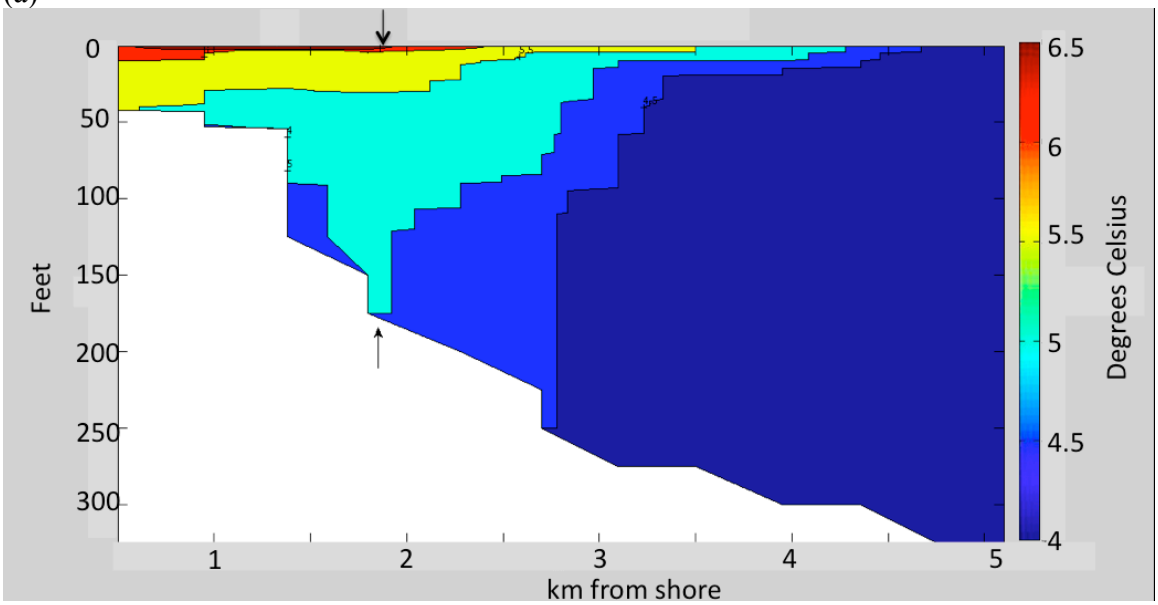

(b)

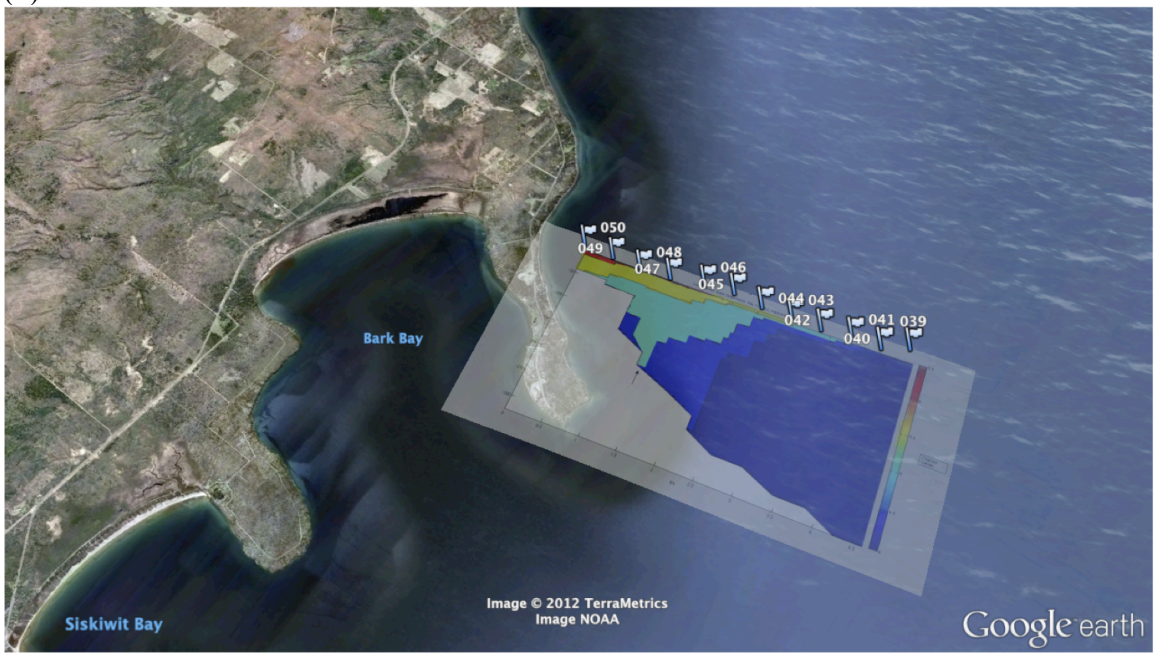

Figure 3. Lake Superior thermal bar. Temperatures shown were obtained during a transect from offshore station 39 to nearshore station 50 between 10:50 am and 1:10 pm, May 10, 2012. Arrows (a) indicate location of station 47, where debris was observed at the surface. Bottom contours over 100 feet deep in (a) are from 2 km resolution bathymetric map, and were not obtained in the field.

Figure 4. Photos of debris which was widespread at station 47. Debris consisted of dead insects which appeared to be midges as well as cases suggesting there had recently been a hatch. Other debris included feathers, pine needles and yellow dust sized particles later identified as spruce pollen under microscope.

Appendix 2: Nested grid model of Lake Superior's western arm.

In this appendix, I provide an overview and example of a nested grid simulation using the Lake Superior model.

A key question faced when configuring ROMS for a particular application is what scale to use for the orthogonal grid. The decision is based on the scale of the circulation desired, computational cost, and uncertainty in boundary conditions. Compared to a coarse grid, a smaller grid size resolves finer details of the circulation, but also increases the time required for a solution. A general rule is that the computation time increases as the cube of the increase in horizontal resolution. For example, increasing the horizontal resolution by a factor of 10 increases the computation time by a factor of 1000; the increase is due to the 100 fold increase in the number of grid cells, and a 10 fold decrease in the time step required to solve the equations over the smaller grid size. Thus the user must ask whether the results of the finer grid are likely to improve the simulation, and whether they are worth the extra time it takes to obtain a solution. In the case where flow is less turbulent, the solution provided by the larger grid size may be essentially the same as the coarse grid. Uncertainty in the boundary conditions (forcing) may also factor into the decision, since resolving fine details of circulation is unlikely to improve the simulation without also providing high resolution forcing.

A nested grid configuration resolves fine scale processes in selected areas, and avoids the computational cost associated with modeling the entire domain at fine

resolution. In nested configuration, a coarse resolution grid (the donor grid) is used to create boundary conditions for a fine resolution grid (the recipient grid) covering an area of interest. Multiple nested layers are possible.

Nesting can be online or offline. In an online configuration, results from the fine scale grid are fed back to the coarse grid. In contrast, an offline nesting configuration is one-way with no feedback to the donor grid from the recipient grid solution. The ROMS developers have not yet incorporated the ice module used in the Lake Superior model into the online nesting capabilities, and so for now, nested configurations of the model are limited to offline nesting.

My objective for the nested configuration in the Lake Superior model was to increase the resolution of circulation near shore in order to resolve small eddies, and the springtime thermal bar. This required an estimate of the typical length scale of eddies in the lake. The temperature and rotation of the eddies detected in the SAR study suggested the eddies were geostrophic, with an average diameter of 8 km. However, limitations of the SAR technique meant some eddies may not have been detected, for example if there were no surfactants, or if wind speeds were too low or too high.

The energy source for geostrophic eddies can be barotropic, in which the eddy energy is derived from the kinetic energy of the mean flow, or baroclinic, in which the eddy energy is supplied from the potential energy of sloping isopycnals. The fundamental length scale of baroclinic eddies is the first baroclinic deformation radius R_1, the length scale where buoyancy effects are equal to rotational effects. The non-dimensional

parameter $e = R_1/\Delta x$ is used to classify model resolution as eddy resolving ($e > 4$), eddy permitting ($e \sim 1\text{-}4$) or eddy excluding ($e < 1$).

Within the Great Lakes, the deformation radius varies between 2 and 5 km due to seasonal differences in the buoyancy effects including changes in the thickness of the surface mixed layer and the density gradient across the thermocline. Thus, the 2 km horizontal resolution Lake Superior grid is eddy permitting when $R_1 = 2 - 8$ km, and eddy resolving when $R_1 > 8$ km. To resolve eddies under conditions when $R_1 = 2$ km, horizontal resolution of 500 m is required.

The tools for making the grid, boundary conditions and forcing for the nested configuration are all found in the latest (2013) version of the ROMS matlab tools, which are distributed with the ROMS. I used the tools as described below to make a recipient grid with horizontal resolution of 400 m and corresponding forcing and boundary condition files. The primary script for constructing the fine scale grid is coarse2fine.m. The fine scale forcing was constructed using coarse2fine.m. The boundary condition files were constructed from the donor grid output.

A. Prepare the recipient grid

In the ROMS package, cd to roms/roms_matlab/grid.

A description of the grid making utilities is in the file Contents.m.

The script coarse2fine.m makes the fine scale recipient grid.

Parameters to be defined :

- Ginp, the name of the donor grid.

- Gout, the name to be given the recipient grid.
- Scale factor: Using "5" for scale factor results in a 400 meter recipient grid from a 2 km donor grid. Note that the scale factor cannot just be any number. Recommended scale factors are described in the comments in the header of the coarse2fine.m script.
- X and Y coordinates of the area in the donor grid.
    - it is recommended that the recipient (nested) area is a rectangle, to avoid i,j confusion.

Example:

start matlab ;

cd to roms/roms_matlab/grid ;

enter the following at the matlab prompt:

Ginp = '~/Grid/LS_grid_5km.nc' ;

Gout = 'LSWA_1k.nc';

coarse2fine(Ginp,Gout,5,1,22,8,33)

Refine the recipient grid by adding coastline and landmask

The recipient grid will retain the coastline of the donor grid. To resolve coastline features at the finer scale, use the tools in the directory /roms_matlab/landmask/. The process is described in roms_matlab/landmask/Contents. Figure 1 shows an example before and after the coast is smoothed. In the case of the Lake Superior, the coastline file

was provided with the bathymetry data as a separate file from GLERL. GLERL coastline data is in the roms_matlab/grid directory.

If no coastline file is available, or if additional editing of the landmask is required, use the interactive script matlab/roms_matlab/editmask.

Figure 2 shows screenshots of the 'editmask' gui:

1. the gui prompts the user for name of grid file to edit.
2. use mouse to convert 'land' to 'sea' or vice versa
3. upon exit, the new coastline file is saved.

B. Prepare forcing files for the recipient grid.

Although ROMS *should* be able to interpolate forcing files from the donor grid to the finer scale recipient grid, I found in practice that the size of the grid in the forcing file must match the size of the grid in the grid file. Therefore for the offline nesting, I create a separate forcing file, interpolated from the forcing file used in the original (donor) model run. The new forcing file grid size corresponds to the spatial resolution of the recipient grid. I use this script ~/Forcing/interpcoarse2fine.m. Instructions are in the header section of the script.

C. Prepare initial conditions for recipient grid:

One of the objectives of the offline nesting is to run the fine scale model over a specific time period. The initial conditions for the fine scale run are prepared from the output of the coarse scale run, and then interpolated to the fine scale grid. Use the matlab

tools in the directory ~/matlab/roms_matlab/initial. Two scripts to become familiar with are c_initial.m ('c' for 'create') and d_initial.m ('d' for 'driver'). The first script creates the NetCDF file. As the name suggests, the second script runs the process, and as provided, it is a template. Modify as necessary. For additional description of the process and the other scripts involved, see the files Contents.m and README in the directory ~/matlab/roms_matlab/initial/.

D. Prepare boundary conditions for recipient grid

An offline nesting configuration is basically a model run that utilizes the results of another model run as boundary conditions. An issue arises in that the coarse resolution output needs to be resized to correspond to the scale of the recipient grid. The ROMS matlab toolbox includes matlab scripts to do this. The driver script is named d_initial (as in the other matlab tools, 'd' stands for driver). For a full description of how the driver script interacts with the other associated scripts, see the file Contents.m in the directory ~/matlab/roms_matlab/boundary/

Note that in contrast to the size of the forcing files, in which the size of the parameters are all the same (i,j) as the size of the recipient grid domain, the (i,j) (column,row) size of ROMS variables required as boundary conditions varies depending on the variable. For example, bulk properties including temperature and salinity are calculated on the 'rho' grid, corresponding at the center of the grid cell, and so the size of the matrix describing them is the number of (i,j). Therefore, for these variables, their size in the boundary condition file will correspond to the size of the recipient grid. It is

recommended that the recipient grid be a rectangular area to avoid confusion about which boundary is which.

For example, for a northern boundary, the size of variables defined on the rho grid will be equal to the number of columns in the recipient grid, assuming north is at the top of an orthogonal area. On the other hand, the component of velocity in the u direction is calculated at the right hand edge of each grid cell, and are numbered beginning with the left most cell, and ending with the penultimate right hand cell, since the outer edge of the last cell in each row is the boundary of the domain. Thus, the size of variables defined on the U grid is (i-1, j), and for a northern boundary, the variables will be the number of columns - 1 of the recipient grid. Similarly, variables calculated on the 'v-grid', including the V velocity component are (i, j-1). Thus the size of variables defined on the v-grid in the boundary conditions file will be 1 less than the number of rows of the recipient grid.

E. Running the recipient grid model

I found the boundary conditions files were the most troublesome to make, and part of the trouble was that at first the model would not run with the boundary condition files I created. Partly this was because I did not have the correct open boundary condition settings in the .in file when running the model. After searching the ROMS user forum for advice, I found the following "open boundary conditions recipe", in a post by Kate Hedstrom (Figure 3). The recipient grid model ran successfully after these conditions were specified in the .in file.

Examples of the recipient grid output are provided in Figure 4. In general the finer scale recipient grid resolves the three dimensional thermal structure close to shore including the thermal bar in the vicinity of Bark Point.

(a)

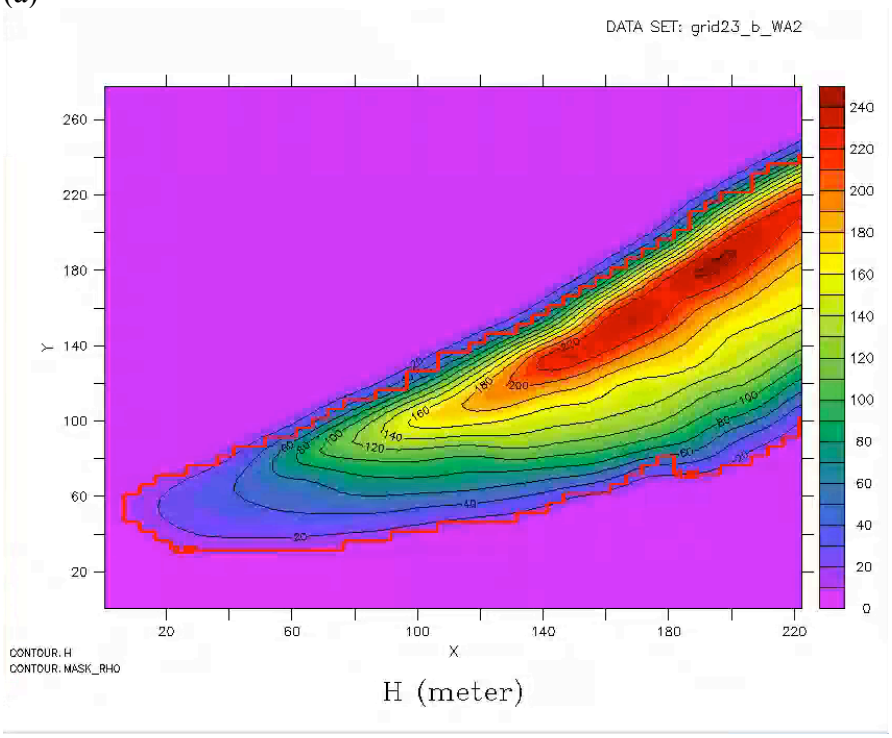

(b)

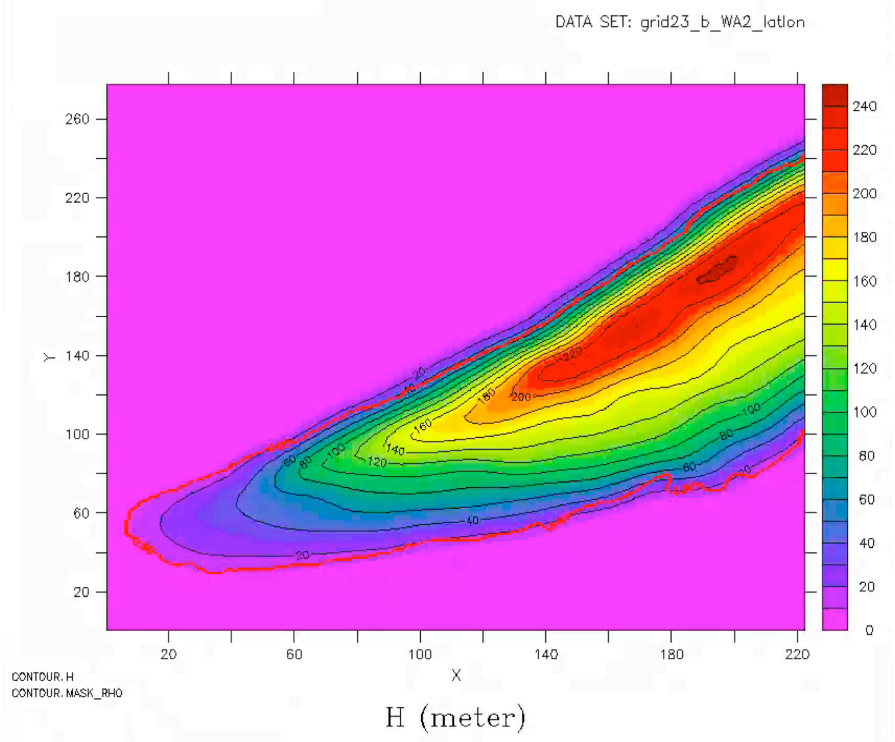

Figure 1. Comparison of coastline from donor grid (a) and smoothed coastline (b).

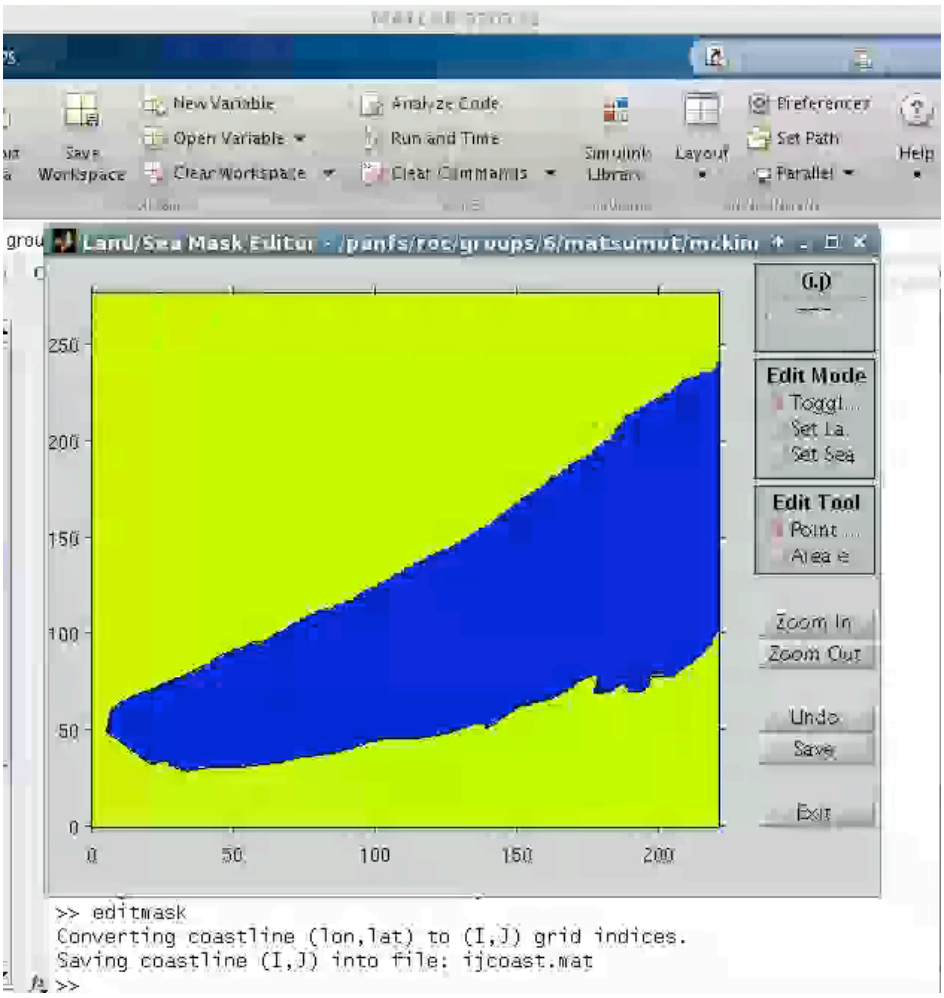

Figure 2. Screenshot from landmask GUI. The landmask can be edited manually where necessary.

```
! see Kate Hestrom OBC 'recipe'

  LBC(isFsur) ==   Clo     Clo     Cha     Clo         !  Cha free-surface
  LBC(isUbar) ==   Clo     Clo     Fla     Clo          ! Fla 2D U-momentum
  LBC(isVbar) ==   Clo     Clo     Fla     Clo          ! Fla 2D V-momentum
  LBC(isUvel) ==   Clo     Clo     RadNud  Clo          ! Rad 3D U-momentum
  LBC(isVvel) ==   Clo     Clo     RadNud  Clo          ! Rad 3D V-momentum
  LBC(isMtke) ==   Clo     Clo     RadNud  Clo          ! Clo mixing TKE
  LBC(isTvar) ==   Clo     Clo     RadNud  Clo \         ! Rad temperature
                   Clo     Clo     Rad     Clo \        ! Clo salinity
                   Clo     Clo     RadNud  Clo \         !  dye_01
                   Clo     Clo     RadNud  Clo \         !  dye_02
                   Clo     Clo     RadNud  Clo \         !  dye_03
                   Clo     Clo     RadNud  Clo \         !  dye_04
                   Clo     Clo     RadNud  Clo          !  dye_05
```

Figure 3. Open boundary condition settings. I located these in a post by Kate Hedstrom in the ROMS online forum. These are set in the .in file prior to running the model.

(a)

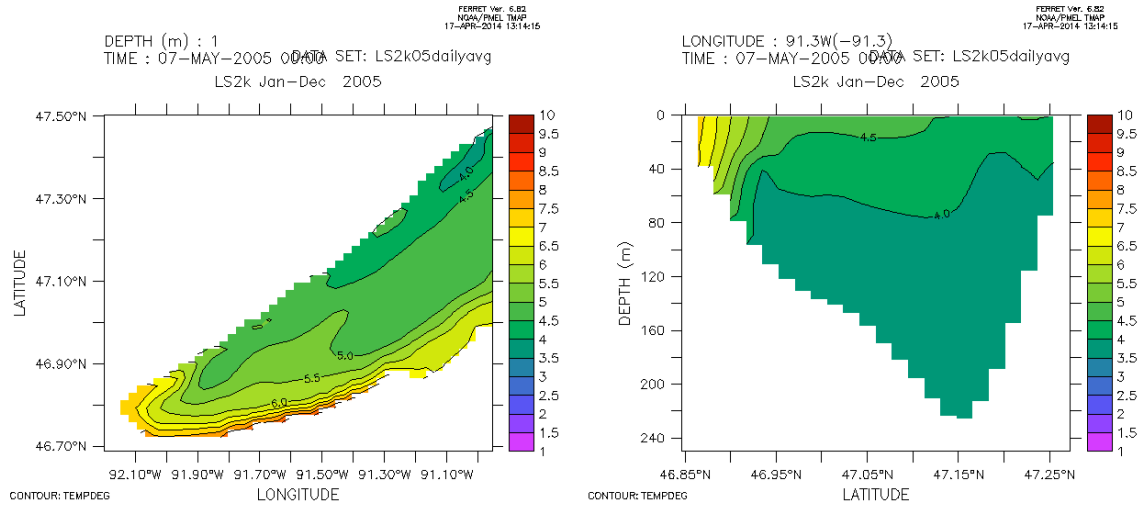

(b)

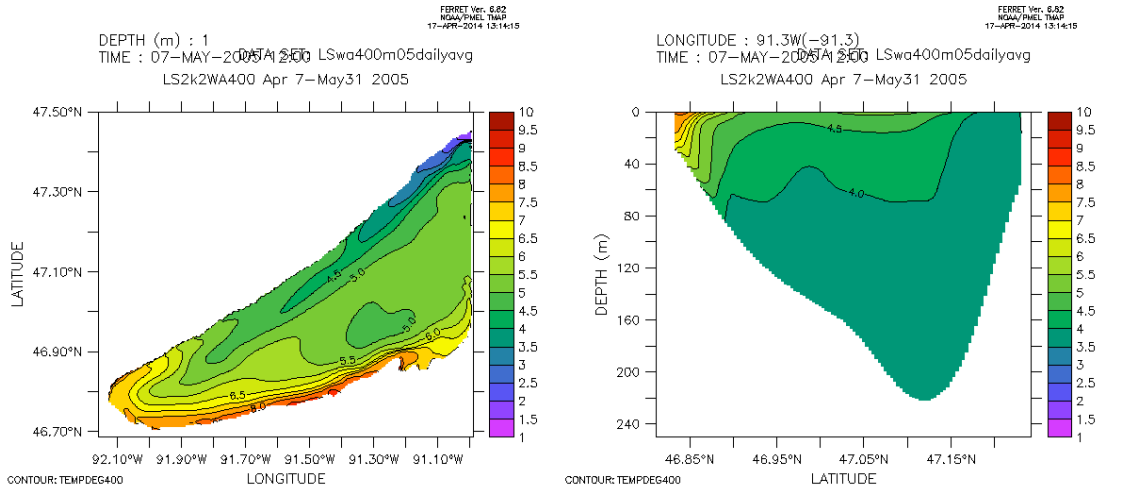

Figure 4. Comparison of output from 2 km (a) and 400 m (b) resolution models. Temperatures from 12:00 pm May 7, 2005 from the 2 km resolution model (a) and the 400 m (b) resolution grids. The cross section views (right) from longitude 91.3 west.